SYNTHETIC OBSERVATIONS USING A ROBUST END-TO-END RADIATIVE TRANSFER MODELING PIPELINE

A Dissertation
Presented to
The Academic Faculty

By

Kirk Stuart Simeon Barrow

In Partial Fulfillment
of the Requirements for the Degree
Doctor of Philosophy in the
School of Physics

Georgia Institute of Technology

May 2018

SYNTHETIC OBSERVATIONS USING A ROBUST END-TO-END RADIATIVE TRANSFER MODELING PIPELINE

Approved by:

Dr. John Wise, Advisor
School of Physics
Georgia Institute of Technology

Dr. David Ballantyne
School of Physics
Georgia Institute of Technology

Dr. Pablo Laguna, Chair
School of Physics
Georgia Institute of Technology

Dr. Tamara Bogdonovic
School of Physics
Georgia Institute of Technology

Dr. Marcus Holzinger
School of Aerospace Engineering
Georgia Institute of Technology

Date Approved: March 27, 2018

Acknowledgments

I would first like to thank my thesis advisor Dr. John Wise for his mentorship, his patience, and his insight these long six years from undergrad through to my defense. It has been a harrowing journey and I certainly could not have done it without him. I would also like to thank the Georgia Tech School of Physics and the Center for Relativistic Astrophysics for facilitating an excellent academic program and a continuous stream of invited speakers. I would of course also like to thank the school for taking a chance on me and supporting me financially as a research assistant and a teaching assistant.

I would also like to thank Dr. Marcus Holzinger for encouraging me to pursue research in orbital mechanics and Dr. Nathan Strange and the Jet Propulsion Laboratory for hosting me for a life-changing summer internship.

Finally, I would like to thank my friends and family and especially my partner for always being there to support me and believe in me when the challenges of an academic career felt insurmountable.

Contents

List of Tables

List of Figures

SUMMARY

The Epoch or Reionization (EoR; $15 \geq z \geq 6$) is currently the farthest into the Universe the current generation of infrared space telescopes can observe[e.g., 3–5]. Though cosmological simulations are often run to low redshift by making trade offs on feedback routines or scale, the EoR is currently the furthest forward large-box, radiative-transfer cosmological simulations can calculate[e.g. 2, 6, 7]. This generates a thin envelope within which simulated objects and observational targets may be contemporaneously studied with the benefit of a full physics prescription. The convergence of the two fields on the EoR is especially compelling as it is host to a large number of theoretically and numerically predicted phenomena that have yet to be empirically constrained. These include metal-free Population III stars, possible progenitors of supermassive black holes such as direct collapse black holes (DCBH), the early Universe luminosity functions, galaxy morphologies, the nature of the early intergalactic medium (IGM), interstellar medium (ISM) enrichment, and the radiative engines of reionization. With the forthcoming *James Webb Space Telescope*(JWST)[8] becoming operational soon, work by Barrow et al. [9] on robustly producing representative synthetic observations and predictions is timely. By emphasizing applicability to generalized scenarios in the construction of the radiative transfer technique, a bevy of astrophysical phenomena are modeled, studied, and compared with observation, producing several novel predictions.

CHAPTER 1
OBSERVATIONS OF THE HIGH-REDSHIFT UNIVERSE

In 1965, a nearly completely isotropic and seasonally-invariant background radiation was observed in the sky by Penzias and Wilson [10]. The shape of its spectrum corresponded to a temperature of $\sim$ 2.725 K (originally reported as 3.5 $\pm$ 1.0 K), peaking at a wavelength of 1.063 mm. Follow up work by Dicke et al. [11] revealed that this cosmic microwave background (CMB) was our view of the first light that escaped when baryons recombined less than 400,000 years after the Big Bang[12]. Since radiation was coupled directly with matter at this time, the polarization and power spectrum of the CMB hold the promise of several insights about the initial structure and constituents of the universe and its discovery prompted the deployment of several dedicated observational missions including, most recently, the Planck Observatory[13].

The final release of data from Planck observations of the CMB[14] in 2015 suggest strong agreement with a cosmological constant-cold dark matter (ΛCDM) model of an expanding universe. Riess et al. [15] independently concurred using near-field observations of standard candles using the Hubble Space Telescope (HST), albeit with some tension[16] between their reported Hubble constants[1]. The source of this discrepancy is a field of active study and may reveal new insights into the manner in which the universe expands. For now, however, the best model for the evolution of the scale factor, a, is given by

$$H(z) = \frac{\dot{a}}{a} = H_0 \sqrt{\Omega_{\mathrm{r},0}(1+z)^4 + \Omega_{\mathrm{M},0}(1+z)^3 + \Omega_{\mathrm{k},0}(1+z)^2 + \Omega_{\Lambda,0}}, \tag{1.1}$$

[1] see Appendix A for a derivation of the Hubble constant

with standard definitions as described in Appendix A. According to Planck, the values for the cosmological constants for their cross year "all in" model are $H_0 = 67.74 \pm 0.46$ km s^{-1} Mpc^{-1}, $\Omega_{M,0} = 0.3089 \pm 0.0062$, $\Omega_{\Lambda,0} = 0.6911 \pm 0.0062$, $\Omega_{k,0} = 0.0008^{+0.0040}_{-0.0039}$, and $\Omega_{r,0} \approx 9.153 \times 10^{-5}$. Using these values, the age of the Universe is

$$t_H = \int_0^\infty \frac{dz}{(1+z)H(z)} \approx 13.813 \pm 0.021 \text{ Gyr.} \tag{1.2}$$

While the CMB offers a glimpse of baryogenesis in the earliest moments of the Universe, subsequent phenomena do not as easily lend themselves to observation. Except for the CMB, the oldest object observed is galactic source Gn-z11 at $z = 11.09^{+0.08}_{-0.12}$ or about 13.39 Gyr ago[17], which was detected using *HST*. This, of course, is a remarkable achievement and a testament to the legacy of *HST*, but we are still unsatisfyingly left without any direct observational data of any kind for the foundational first ~ 420 Myr of the Universe.

This problem is not entirely dissimilar to Ferdinand Magellan's quest for East India across the unexplored Pacific. That is, we know the initial and final state of a complex physical system, but are provocatively left to convincingly connect the two. As cosmologists and astronomers, we are driven by the same inescapable instinct for exploration and similarly informed about the size of our frontier and what we might find.

1.1 Observational Techniques and Constraints

Our knowledge of the contents of Universe is entirely derived from telescope observations so a cursory review of our observational tools and techniques is warranted. By wavelength from short to long, the current field-leading cadre of ground and space telescopes are as follows.

Cosmic ray: High Altitude Water Cherenkov Experiment. Ice Cube Neutrino

Observatory **Gamma-ray**: Fermi Gamma-ray Space Telescope. Swift Gamma Ray Burst Explorer. Very Energetic Radiation Imaging Telescope Array System. **X-ray**: Chandra X-ray Observatory. Swift Gamma Ray Burst Explorer. **UV**: Hubble Space Telescope. Swift Gamma Ray Burst Explorer. **Visible**: Hubble Space Telescope. **Infrared**: Hubble Space Telescope. Spitzer Space Telescope. Herschel Space Observatory. **Sub-millimeter**: Herschel Space Observatory. Atacama Large Millimeter Array. Sub-millimeter Array. James Clerk Maxwell Telescope. **Microwave**: None. **Gravity**: Laser Interferometer Gravitational-Wave Observatory.

HST has served as the flagship space observatory for UV and IR observation since 1990 and was upgraded and repaired by astronauts over the course of five Space Shuttle missions through 2009. The forthcoming *James Webb Space Telescope*(JWST)[8] is due to assume *HST*'s role with more powerful instrumentation pending a successful launch in 2020.

IR space observatories like *HST* and *JWST* are well-suited for deep field observation because they observe at frequencies that correspond to a source's brightest wavelengths before red-shifting. However, light from high-redshift objects are subject to several effects as a consequence of the Universe's cosmological expansion and the physics of photon detection.

1.1.1 Cosmological Distances and Flux

Gn-z11 was captured by Hubble Space Telescope's Wide Field Camera 3 (*WFC*3), which has a 123x137 arcsecond field of view and a pixel size of 0.13 arcseconds in the near infrared channel used for this observation. *WFC*3, like most telescope camera systems, features a set of filters that select light by wavelength as well as grating prisms, or grisms, that spatially separate light of different wavelengths for a point source along a row of pixels.

Objects at high redshift like Gn-z11 are difficult to view because their great dis-

tance attenuates their flux at the telescope. The distance-flux relationship is governed by three effects. First, the bolometric flux, F, of light at an observer viewing a point source at high redshift in units of erg s^{-1} cm^{-2} is

$$F = \frac{L}{4\pi d_{\mathrm{L}}^2(z)}, \tag{1.3}$$

where L is the bolometric luminosity in units of erg s^{-1} and the luminosity distance, $d_{\mathrm{L}}(z)$, is

$$d_{\mathrm{L}} = c(1+z)\int_0^z \frac{dz'}{H(z')}, \tag{1.4}$$

which is derived by integrating the Friedmann–Robertson–Walker (FRW) metric[18] for a source at redshift z. This is very different than the distance a photon actually travels, which is given by the co-moving distance

$$d_{\mathrm{c}} = c\int_0^z \frac{dz'}{(1+z')H(z')}. \tag{1.5}$$

The factor of $(1+z)$ in Equation 1.4 means that the flux of an object decreases asymptotically as one looks closer to the Big Bang and illustrates why viewing the furthest 420 Myr is so much more difficult than the preceding 13,390 Myr.

Second, the angular dimension of an object in an observer's sky, θ_0, is related to its proper width, W, and the luminosity distance by the Etherington [19] relation

$$\theta_0 = \frac{(1+z)^2 W}{d_{\mathrm{L}}(z)}. \tag{1.6}$$

Here, the factor of $(1+z)$ in the numerator stretches objects across the sky at high redshift. We can invert Equation 1.6 by fixing θ_0 for a given pixel resolution to solve for the corresponding width of its field of view. We find, for example, that one pixel in the IR channel of *WFC3* is about 514 pc at $z = 11.1$, which shrinks to 412 pc at $z = 15$.

This may seem useful to observers interested in the fine details of an astronomical object, however Equation 1.4 and Equation 1.6 conspire together to attenuate the observed surface brightness, Σ, of an extended object with proper area, A, according to the relationship

$$\Sigma = \frac{F}{\theta_0^2} = \frac{L}{4\pi A(1+z)^4}. \tag{1.7}$$

The third effect is to the benefit of observers using filters. The monochromatic flux, $f_{\omega,0}$ of an object in units of erg s^{-1} cm^{-2} Hz^{-1} is given by

$$\omega_0 f_{\omega,0} = \frac{\omega_e L_{\omega,e}}{4\pi d_L^2(z)}, \tag{1.8}$$

where ω_0 and ω_e are the observed and emitted frequency of the light respectively and $L_{\omega,e}$ is the emitted monochromatic spectral luminosity with units of erg s^{-1} Hz^{-1}[20]. Since the observed frequency is $\omega_e = (1+z)\omega_0$ by the definition of a redshift, Equation 1.8 obtains a factor of $(1+z)$ in the numerator. If we integrate Equation 1.8 over the observed frequency and apply a redshifted filter response, $R_{\omega,e}$, the total flux through a filter is

$$F = \frac{(1+z)}{4\pi d_L^2(z)} \int_0^\infty L_{\omega,e} R_{\omega,e} d\omega. \tag{1.9}$$

1.1.2 Noise and Optical Effects

Circular lenses and mirrors like those employed by *HST* naturally diffract effective point sources into an Airy [21] disk. This has the effect of spreading the natural intensity of an observed object over several pixels and blurring observations. Anderson [22] reports that the *WFC3* IR filter point-spread functions (PSF) show a peak intensity between 2/5 and 1/2 of the intensity derived from Equation 1.9, with the rest of the energy spread across nearby pixels.

Optical instruments are also subject to several sources of noise. Source radiation, S_0, in photons s^{-1} have a random temporal spacing between the emission of individ-

ual photons. Also, due to photon scattering in a diffuse interstellar or intergalactic medium (see Section 2.1.2), light from secondary sources also hit the detector, accumulating in a random sky background, S_s, in photons s^{-1} pixel^{-1}. The temperature of the detector also leads to collisional excitations and spontaneous, random emission (see Section 2.1.3) that cannot be distinguished from source photons in what is termed the dark current, S_d, also in photons s^{-1} pixel^{-1}. Thus, the number of photons that hit the receiver from the source thus takes the form of a Poisson [23] cumulative random distribution. The standard deviation for the number of events, n, in a cumulative random process is $\sigma = \sqrt{n}$ and the total standard deviation for multiple independent random processes is

$$\sigma_\mathrm{T} = \sqrt{\sum_i \sigma_i^2}. \tag{1.10}$$

The actual measurement of an incident photon usually requires a voltage change in the detector and is subject to a systematic read out noise with stand deviation R. Taken together, if we define the noise of the incident flux to be the standard deviation of the observed photon flux, the total noise, N, is

$$N = \sigma_\mathrm{T} = \sqrt{S_0 Qt + n_\mathrm{p}(S_\mathrm{s} Qt + S_\mathrm{d} t) + R^2}, \tag{1.11}$$

where Q is the fraction of photons that excite the detector, n_p is the number of pixels the source extends over, and t is the exposure time. The ratio of the photon flux from the source, $S_0 Qt$, to the noise known as the signal-to-noise ratio, S/N, is therefore

$$S/N = \frac{S_0 \sqrt{Qt}}{\sqrt{S_0 + n_\mathrm{p}(S_\mathrm{s} + S_\mathrm{d}/Q) + R^2/(tQ)}}. \tag{1.12}$$

In the limit where the readout noise is small compared to the source flux or exposure times are large, we get the simple relation $S/N \propto \sqrt{t}$. Below certain values of S/N,

a source cannot be statistically distinguished from the noise. It can be said, then, that the limiting factors for observing the early Universe are the availability of long exposure times and the sensitivity of the available instruments. However, given that there are so few IR observing space telescopes available to astronomers and a large number of scientifically interesting targets to investigate, we are likely resigned to barely discerning high-redshift objects for the foreseeable future, even with *JWST*.

1.2 Modeling an Unseen Universe

Since our ability to observe the early Universe is constrained by hardware, it is incumbent on the field to devise new methods of discerning novel mechanisms from observationally degenerate phenomena. In the near-field, one can sometimes rely on empirical data and a well-established astrophysical model to confirm such an observation. In the frontier beyond Gn-z11, however, empiricism is completely supplanted by theory. It is therefore prudent to briefly examine the working narrative of the physical evolution of the early Universe, how we arrived at it, and its caveats.

1.2.1 The Grand Narrative

The composition of the Universe at the time of the CMB is deduced from observation as evolved within the framework of the FRW metric. The matter component, $\mathbf{\Omega_M}$, is comprised of a baryonic and non-baryonic matter of which the non-baryonic component is $\sim 85\%$ according to Planck Collaboration et al. [14]. Non-baryonic (dark) matter has never been directly observed and the nature of its constituents are an active field of research. It is generally assumed to primarily interact gravitationally based on the non-peaked shape of the potential wells in large galaxies[24–26], whereas we know diffuse baryonic matter reacts detectably to hydrodynamic and thermal effects in addition to gravitational attraction.

According to the CMB, the primordial density fluctuations in the Universe are on

the order of 10^{-4} so the contributions of the intraparticle gravitational field mostly canceled each other out. Equation 1.1 implies that the rate of expansion of the Universe was also much larger relative to its size at high redshift. Matter therefore initially moved approximately linearly with the expansion rate until $z \sim 100$, when the density perturbations grew enough to induce strong non-linear interactions at the smallest scales[27]. After which, matter evolves according to the equations of fluid dynamics. The continuity equation in comoving coordinates and velocities is

$$\frac{\partial \rho}{\partial t} + 3H\rho + \frac{1}{a}\nabla(\rho\vec{v}) = 0, \tag{1.13}$$

where ρ is the density. The Euler equation is

$$\frac{\partial \vec{v}}{\partial t} + \frac{1}{a}H(\vec{v}\ \nabla)\vec{v} = -\frac{1}{a}\frac{\nabla P}{\rho} - \frac{1}{a}\nabla\phi, \tag{1.14}$$

where P is the pressure, $\vec{v}$ is the peculiar velocity, and ϕ is the peculiar local gravitational potential. Finally, the Poisson equation is

$$\nabla^2\phi = 4\pi G a^2(\rho - \bar{\rho}), \tag{1.15}$$

where $\bar{\rho}$ is the mean density of the Universe, and G is the gravitational constant. If we take perturbations in dark matter density to be small and assume $P = 0$, we can combine these equations to evolve dark matter overdensity, $\delta = \rho - \bar{\rho}$, with

$$\ddot{\delta} + 2H\dot{\delta} = 4\pi G\bar{\rho}\delta. \tag{1.16}$$

This is the governing equation of a dark matter-only or "N-body" simulation, which reproduces the observed filamentary structure of the Universe to first order when evolved from the initial perturbations seen in the CMB. In these simulations, we

see the spherical accumulations of dark matter "haloes" at the nexus of filaments where one would expect the presence of galaxies. These haloes merge over time into progressively larger haloes and clusters.

Baryonic matter (gas) overdensities grow quickly in haloes, precluding the effective use of perturbation theory to describe its dynamics. For gas, it is sometimes more convenient to recast Equation 1.14 in terms of energy density, E, rather than a momentum conservation, and we thus obtain the form

$$\frac{\partial E}{\partial t} + \frac{1}{a}\nabla \cdot (E + P) = -2HE - \frac{\rho}{a}\vec{v}\,\nabla \cdot \phi + \dot{E}, \tag{1.17}$$

where $\dot{E}$ is the net of heating and cooling terms due to physical processes within the gas. Eqs. 1.13, 1.15, and 1.17 form the basis of a hydrodynamic cosmological simulation. These are dramatically more computationally expensive to perform than N-body simulations, but allow us to track the collapse of gas into denser structures and deduce a more accurate picture of the matter distribution of the Universe. These simulations show us that the first ~ 180 Myr ($z > 20$) of the Universe were relatively cold, neutral, dark, and uneventful as local density peaks were still too low to form stars or galaxies[28].

After this point there is compelling evidence that stars formed[29, 30], so careful consideration and handling of resolution, star formation, black holes, and $\dot{E}$ are required to produce an accurate model. We know, for example, that the intergalactic medium (IGM) of the Universe was completely reionized by radiation by $z = 5.7$[31], but the timing and contributing elements are still an area of active research[e.g. 32]. The formation of the first stars, the first galaxies, and the first black holes are also under study as well as the manner in which the Universe went from primordial abundances of hydrogen and helium to the present-day abundances of heavier elements. In order to constrain any of these processes with observations, we need to devise a

method of converting our theoretical and simulated physical predictions into their observational counterparts. The first step in this process is a model for the evolution of radiation through the Universe.

1.3 Overview of Thesis

In the work described in subsequent chapters, we use data produced with the collaborative cosmological simulation code Enzo[33], which employs several techniques to handle each of the progressively more complex phenomena that occur as the Universe evolves. In the next chapter, we focus specifically on the background and theory behind a numerical solution to radiative transfer including a brief overview of the technique employed in Enzo. The third chapter begins a discussion of our technique for converting simulation data into observables using a novel post-processing radiative transfer pipeline (Caius) and makes predictions for *HST* and *JWST*. The fourth chapter describes advancements to Caius and focuses on predictions for high energy sources like massive stars and binary stellar remnant black holes. The fifth chapter makes predictions for massive black holes. Finally, the sixth chapter summarizes our conclusions and charts a plan for future studies.

CHAPTER 2
RADIATIVE TRANSFER IN COSMOLOGICAL SIMULATIONS

2.1 The Radiative Transfer Equation

In radiative transfer theory, incident radiation traveling through a medium may be absorbed, scattered, or gain energy through emission. A review of these three mechanisms in the context of astrophysical plasma is detailed in this section to support and motivate the research described in subsequent chapters.

2.1.1 Extinction

2.1.1 Bound States

Extinction is defined as the attenuation of monochromatic light along a path in a medium by an energy exchange or absorption. For atoms with bound electrons or subject to inter-molecular bonds, electrons may absorb photons corresponding to the difference between their current and unoccupied energy levels. However, there are several restrictions to the allowable states. First, since photons are vector particles (bosons), they carry a spin angular momentum, s, of 1 and their total angular momentum $j = s + l$, where l is orbital angular momentum, must be conserved in an interaction. Second, the parity, given by $(-1)^l$, of the final energy state must have the opposite sign of the initial energy state for an allowed electronic dipole transition, which results in the rule that $l_f = l_i \pm 1$. In a single-electron hydrogen atom, for example, electrons can transition between the 1s state ($j = 1/2, l = 0, s = 1/2$) and the 2p state ($j = 3/2, l = 1, s = 1/2$), but cannot easily transition to the 2s state ($j = 1/2, l = 0, s = 1/2$), a so-called "forbidden transition." These and other transition selection rules are described by the Wigner-Eckart theorem[34] and the corresponding

Clebsch–Gordan coefficients.

Despite the foreboding name, forbidden transitions are nevertheless usually possible with a diminished probability. In the case of the 1s to 2s transition, it can be achieved by the simultaneous absorption of two photons that cancel out their spin angular momentum contribution. More generally, transition probabilities are best described with the Einstein B coefficient defined as

$$\left(\frac{dn_1}{dt}\right)_{\text{photons},1\to2} = -B_{12}n_1\rho(\omega), \tag{2.1}$$

where n_1 is the number density of electrons in state 1, B_{12} is the Einstein coefficient[35] for the rate of transitions from state 1 to state 2 in $\text{erg}^{-1}\ \text{cm}^3\ \text{s}^{-1}$, and $\rho(\omega)$ is the isotropic spectral energy density in $\text{erg}\ \text{Hz}^{-1}\ \text{cm}^{-3}\ \text{s}^{-1}$ of photons of frequency ω. These coefficients are derived from the convolution of quantum mechanical wave functions of the final and initial states and are thus intrinsic to the atomic or molecular specie. For simple atoms like hydrogen, coefficients can be determined analytically. For more complex atoms and molecules, they must be determined empirically due to the prohibitive complexity of the wave forms.

It is often useful to refer to transition probabilities in the spatial, rather than time domain and determine the rate of energy lost rather than the number of photons absorbed. Since light moves at a constant speed, c, between interactions in a medium, Equation 2.1 can be easily converted to

$$\left(\frac{dn_1}{dz}\right)_{\text{photons},1\to2} = -\frac{B_{12}}{c}n_1(z)\rho(\omega,z). \tag{2.2}$$

We then multiply both sides by the factor $\hbar\omega c$, where $\hbar$ is the reduced Planck constant, and recast $c\rho(\omega,z)$ as the spectral intensity $I(\omega,z)$ to achieve the form

$$c\hbar\omega\left(\frac{dn_1}{dz}\right)_{\text{photons},1\to2} = -\hbar\omega\frac{B_{12}}{c}n_1(z)I(\omega,z). \tag{2.3}$$

Since $\hbar\omega dn_1/dz$ is the spectral energy density lost per unit length, the factor on the left becomes $dI(\omega, z)/dz$ to yield the first order differential equation in intensity

$$\left(\frac{dI(\omega)}{dz}\right)_{1\to 2} = -\hbar\omega\frac{B_{12}}{c}n_1 I(\omega, z). \tag{2.4}$$

We conveniently define the interaction-dependent extinction cross-section as

$$\sigma(\omega)_{1\to 2} = \hbar\omega\frac{B_{12}}{c}, \tag{2.5}$$

in units of cm^2, and solve the differential equation to attain the form

$$I(\omega, z_f) = I(\omega, z_i)e^{-\sigma(\omega)_{1\to 2}\int_{z_i}^{z_f} n_1(z)dz}, \tag{2.6}$$

which is an arbitrary function for the absorption of the spectral intensity as radiation moves through the medium due solely to transitions from state 1 to state 2 and based on the number density of electrons in state 1.

Since Equation 2.4 is an explicit function of the number of electrons in the initial state, other factors that affect the states of electrons such as collisions become important when determining how much radiation is absorbed. For example, molecules also absorb energy through collisions with other particles, according to

$$\left(\frac{dn_1}{dt}\right)_{\text{collision},1\to 2} = -q_{12}n_1 n_o, +q_{21}n_2 n_o \tag{2.7}$$

where q_{12} and q_{21} are the transition rates to and from state 2 due to collision respectively, E_i is the energy of state i, and n_o is the number density of the other party to the collision, which may be another atomic or molecular specie or a free electron. When particles interact frequently enough, the occupancy of each energy state can be statistically related to the temperature of the medium. This condition is referred

to as local thermodynamic equilibrium (LTE) and is governed by the Boltzmann [36] distribution

$$\frac{n_1}{n_2} = \frac{g_1}{g_2} e^{(E_2 - E_1)/kT}. \tag{2.8}$$

Here, g_2 and g_1 are the degeneracy of each energy state, $k \sim 1.3806 \times 10^{-16}$ erg K^{-1} is the Boltzmann constant, and T is the temperature. The value of q_{12} in Equation 2.7 similarly becomes an implicit function of temperature to account for the number of particles of type n_o that have enough kinetic energy to trigger an electronic transition to state 2 from state 1. However, Equation 2.8 is only useful when the incident field is weak or non-existent since it does not include an accounting of photo-excitation. Usually, the collisional and photo-excitation rates need to be combined to accurately determine state occupancy densities (see Equation 2.29). Equation 2.8 is sometimes used with a departure coefficient, b_i, to capture the predicted or measured discrepancies that arise from a collision-only approach where

$$n_{i,\text{corrected}} = b_i n_{i,\text{col.}}. \tag{2.9}$$

In LTE, the kinetic energy of the absorbing molecule along the path of the incident photon affects the frequency dependence of the absorption cross-section by changing the energy required to trigger a transition. In the frame of the absorbing molecule, the frequency of an absorbed photon, ω, is Doppler shifted to the rest frequency ω_{12} according to

$$\omega = \omega_{12}\,(1 + v/c)\,, \tag{2.10}$$

and the normalized Maxwell-Boltzmann distribution[37, 38] for frequency is

$$f(\omega) = \frac{c}{v_{12}} \sqrt{\frac{m}{2\pi kT}} \exp \frac{mc^2(\omega - \omega_{12})}{2kT\omega_0^2}, \tag{2.11}$$

where m is the mass of the absorbing particle. In addition to Doppler broadening,

energy levels are naturally broadened by the Heisenberg [39] uncertainty principle and by pressure broadening. We can combine these effects with Equation 2.5 to get the LTE-specific form of the absorption cross section

$$\sigma(\omega)_{1\to 2,\mathrm{LTE}} = \hbar\omega \frac{B_{12}}{c} \frac{\Gamma(T)}{4\omega_{12}\pi^2} \sqrt{\frac{m}{2\pi kT}} \int_0^\infty \frac{e^{-\frac{mc^2(\omega'-\omega_{12})}{2kT\omega_{12}^2}}}{(\omega-\omega'-c(\omega'-\omega_{12})/\omega_{12})^2 + (\Gamma(T)/4\pi)^2} d\omega', \tag{2.12}$$

where $\Gamma(T)$ depends on the frequency of collisions and electronic transitions between the states.

When collision energies between particles are high enough, electrons can become unbound. In this case, the number of species, n_i, in the ith ionization state is approximately described by the Saha equation[40, 41] in the case of LTE as

$$\frac{n_{i+1}n_e}{n_i} = 2\left(\frac{\sqrt{2\pi m_e kT}}{h}\right)^3 \frac{g_{i+1}}{g_i} \exp -\frac{(E_{i+1}-E_i)}{kT}, \tag{2.13}$$

where h is the Planck constant, m_e is the mass of an electron, and n_e is the free electron number density. In the example of hydrogen, about half of the ground state electrons in LTE are unbound at 2060 K for densities of one hydrogen nucleus per cm^3.

Of course, photons of sufficient energy can ionize atoms and molecules as well, which further affects the availability of electrons and the absorption rate. Since unbound electrons have a continuum of energy levels and states, bound electrons are susceptible to being freed by a range of photon energies in an incident radiation field. However, photon energies higher than the ionization potential are progressively less likely to interact. The extinction cross section for a bound-free transition mostly follows an inverse cube relationship with respect to photon frequency of the form

$$\sigma(\omega)_{\mathrm{ion,Z,n}} = \frac{7.91\times 10^{-18}}{(nZ)^2}\left(\frac{\omega_{\mathrm{ion}}}{\omega}\right)^3 g_{bf}\ \mathrm{cm}^2, \tag{2.14}$$

for hydrogenic atoms[42, 43] where Z is the atomic number, n is the energy level of

the electron, and g_{bf} is a factor of order unity. This approximation is valid when ω is greater than the ionization frequency ω_{ion} and mostly accurate for H, He, and He II, which comprise the greatest fraction of primordial astrophysical media.

2.1.1 Free States

When unbound electrons interact with ionized nuclei, a continuum of energy levels is available for the absorption of photons. The Kramers [44] formula for free-free absorption in hydrogenic atoms in LTE is given as

$$\sigma(\omega)_{ff} = n_e \left(\frac{2m_e}{3\pi kT}\right)^{1/2} \frac{4\pi Z^2 e^6}{3m_e^2 ch\omega^3} g_{ff}(\omega)(1 - e^{-h_\omega/kT}), \tag{2.15}$$

where e is the charge of an electron and g_{ff} is again a factor of order unity.

Due to our strict definition of extinction, independent electrons also exhibit an absorption cross section despite their inability to capture photons. When electrons have kinetic energies comparable to or less than the energies of incident photons, collisions can shift the frequency of the photon in accordance with the Klein and Nishina [45] formula. This shift is expressed as

$$f_\omega(\omega_i, \theta) = \frac{\omega_f}{\omega_i} = \frac{1}{1 + (\hbar\omega_i/m_e c^2)(1 - \cos(\theta))}, \tag{2.16}$$

where θ is scattering angle. The differential cross section as a function of the scattering angle and the initial frequency is

$$\frac{d\sigma}{d\Omega} = \frac{1}{137.04}\frac{\hbar}{m_e c} f_\omega(\omega_i, \theta)^2 \left[f_\omega(\omega_i, \theta) + f_\omega(\omega_i, \theta)^{-1} - sin^2(\theta)\right]. \tag{2.17}$$

This phenomena is referred to as the Compton [46] effect and is confined to X-rays for most medium temperatures due to its dependence on the factor of $\hbar\omega_i/m_e c^2$ in Equation 2.16. When medium temperatures are hot enough for electrons to move

relativistically, Equation 2.16 holds for the frame of the electron $(\omega_i', \omega_f', \theta')$, but must be converted to the laboratory frame $(\omega_i, \omega_f, \theta)$ with the relations

$$\cos(\theta') = \left(\frac{v}{c}\right) \frac{\cos(\theta) + v/c}{1 + (v/c)\cos(\theta)}, \tag{2.18}$$

$$\omega_i' = \omega_i \frac{1}{\sqrt{1 - (v/c)^2}} \left(1 - \cos(\theta')\right), \tag{2.19}$$

$$\omega_f = \omega_f' \frac{1}{\sqrt{1 - (v/c)^2}} \left(1 + \cos(\theta')\right), \tag{2.20}$$

where v is the speed of the electron. The net result after substituting back into Equation 2.16 is that the frequency of the incident photon is boosted rather than decreased after colliding with a relativistic electron.

2.1.2 Scattering

2.1.2 Bound States

We define scattering as the redirection of monochromatic light through interactions with a medium. When bound to nuclei, electrons in excited states spontaneously decay to lower energy levels at rates described by the Einstein A coefficients of units of s^{-1} in the relationship

$$\left(\frac{dn_1}{dt}\right)_{A,\text{photons},2\to1} = A_{21} n_2, \tag{2.21}$$

while emitting photons isotropically. The emission rate of photons due to transitions between state 2 and 1 is further boosted in the presence of a radiation field in a process of stimulated emission, which is described similarly to Equation 2.1, but with reversed subscripts. We can write an expression for the ratio of scattered photons to

the total photons absorbed, the albedo α, as

$$\alpha_{12} = \frac{A_{21}n_2 + B_{21}n_2 I(\omega)}{B_{12}n_1 I(\omega)}, \tag{2.22}$$

where $B_{21} = (g_1/g_2)B_{12}$. In LTE, the frequency-dependent scattering cross section for transitions between states one and two is therefore simply

$$\sigma(\omega)_{\text{scattering},1\to2,\text{LTE}} = \alpha_{12}\sigma(\omega)_{1\to2,\text{LTE}}. \tag{2.23}$$

where $\sigma(\omega)_{1\to2,\text{LTE}}$ is taken from Equation 2.12.

For bound-free interactions, we note that Equation 2.13 assumes a detailed balance between the ionization rate and the recombination rate at a given temperature and electron density in LTE. When electrons recombine with an atom or molecule, their excess energy is released as a photon. However, because we assume that the particles move thermally and electrons can be captured by any energy level in an atom, there is a discrepancy between the form of the absorption cross section in Equation 2.14 and the shape of the recombination spectrum. This results in a frequency-dependent albedo. Cillié [47] found that the recombination rate to level n is

$$\left(\frac{dn_e}{dt}\right)_{\text{recomb,n}} = n_{i+1}n_e\frac{g_{i+1}}{g_i}\frac{2^9\pi^5}{(6\pi)^{3/2}}\frac{Z^4e^{10}}{nm_ec^3h^3}\left(\frac{m_e}{kT}\right)^{3/2}\int_0^\infty \frac{e^{-\frac{m_ev^2}{2kT}}}{E_{n,\text{ion}} + 1/2m_ev^2}vdv. \tag{2.24}$$

Since we are only interested in monochromatic scattering in the incident intensity, we multiply both sides by a factor of $\hbar\omega$ and apply the Kronecker delta function, $\delta(E_{n,\text{ion}} + 1/2mv^2 - \hbar\omega)$, to the integral to retrieve

$$\left(\frac{dI(\omega)}{dz}\right)_{\text{recomb,n}} = n_{i+1}n_e\frac{g_{i+1}}{g_i}\frac{2^9\pi^5}{(6\pi)^{3/2}}\frac{Z^4e^{10}}{nm_ec^3h^3}\left(\frac{m_e}{kT}\right)^{3/2}e^{-\frac{\hbar\omega-E_{n,\text{ion}}}{kT}}\sqrt{2\frac{\hbar\omega - E_{n,\text{ion}}}{m_e}}. \tag{2.25}$$

We can then combine with Equation 2.13 and Equation 2.14 to get the ionizing albedo

for hydrogenic atoms for transition to level n in LTE,

$$\alpha(\omega)_{Z,n,\text{ion}} = \frac{2^9\pi^5 n}{7.91\times10^{-18}}\left(\frac{\omega}{\omega_{\text{ion}}}\right)^3\left(\frac{g_{i+1}}{g_i}\right)^2\frac{m_e Z^2 e^{10}}{g_{bf}c^3h^6}e^{-\frac{\hbar\omega}{kT}}\sqrt{\frac{\hbar\omega - E_{n,\text{ion}}}{m_e}}. \tag{2.26}$$

It should also be noted that Equation 2.26 does not explicitly include terms for energy level broadening and should be convolved in a manner similar to Equation 2.12.

2.1.2 Free States

In the low energy limit ($\hbar\omega \ll m_e c^2$) of photon interaction with free electrons, Equation 2.16 approaches unity and the interaction becomes one of pure scattering ($\alpha = 1$). Herein, Equation 2.17 simplifies to

$$\frac{d\sigma}{d\Omega} = \frac{1}{2}r_e^2[1+\cos^2(\theta)], \tag{2.27}$$

if the forward constants are written in terms of the electron radius, r_e. We can then easily integrate over solid angle to get

$$\sigma_T = \frac{8\pi}{3}r_e^2, \tag{2.28}$$

which is the classical Thomson [48] scattering cross section. However, though it is possible to write this as a single value, the anisotropic nature of the resulting radiation field should be noted for applications where the path of the resulting rays is important.

2.1.3 Emission

2.1.3 Bound States

Emission is defined here as the portion of the radiation field emanating from a medium that is not scattered from an incident field and is generally presented as a spectral energy density, $j(\omega)$, with units of erg s^{-1} Hz^{-1} cm^{-3} sr^{-1}. This measure is derived

from the photon density, $\rho(\omega)$, by dividing it by a factor of 4π and is used to describe a large number of phenomena. Likewise, the spectral radiance $i(\omega)$ in units of erg s^{-1} Hz^{-1} cm^{-2} sr^{-1} is the intensity $I(\omega)$ divided by solid angle. Before delving into these, we need to clarify the difference between scattering and emission with respect to Equation 2.22 and Equation 2.26. In both cases, photons are not technically redirected, but are re-emitted through a separate mechanism with no constraints on the value of the resulting albedo. In the case of bound-bound transitions, the occupancy of the second state can be comparable to the occupancy of the first state at the high temperature limit due to a combination of collisional excitations and the nature of the incident radiation field, which would allow for an albedo greater than one. For bound-free transitions, the inverse cube frequency relationship in the absorption cross section almost guarantees albedos greater than one at higher frequencies, which contradicts the definition of an albedo as a fraction. One solution would be to do away with the concept of scattering and cast every interaction as either an absorption or an emission. In lieu of this, we take the portion of emission representing an albedo greater than one and treat it as an unrelated source of diffuse emission. This treatment allows us to account for scattering phenomena in dense environments analytically without having to track an untenably high number of individual absorption and emission events.

Beyond the treatment of albedo, one key emission mechanism is a line transfer. For a many-state system, the transition rate to a state is given as

$$\left(\frac{dn_j}{dt}\right) = \sum_{i}^{i\neq j}(A_{ij} + n_o q_{ij} + B_{ij}\rho(\omega_{ji}))n_i - (A_{ji} + n_o q_{ji} + B_{ji}\rho(\omega_{ji}))n_j, \tag{2.29}$$

where only the terms with A and B coefficients emit or absorb photons. As such, an electron that transitions to an excited state through photon absorption may undergo several intermediate transitions before it returns to a ground state, emitting photons with various energies along the way. We treat each of these photons as an emission

source distinct from scattering mechanisms. To account for broadening, we once again convolve their emission rate with a frequency profile in a manner similar to Equation 2.12.

The line transfer phenomenon is especially prevalent during electron recombinations, which produce prominent lines in the spectra of astrophysical plasma[e.g. 49]. To account for changes in occupancy due to photoionization and recombination events, Equation 2.13 and Equation 2.24 need to be added to Equation 2.29. Given the unwieldy form of the resulting state transition rate equation, photochemical balances are most conveniently solved numerically, but can in fact be estimated analytically with a judicious application of the departure constant introduced in Equation 2.9.

2.1.3 Free States

Accelerating unbound electrons emit radiation. Free electrons interacting with ions will radiate energy according to the Larmor [50] formula

$$\frac{dJ}{d\Omega} = \frac{Z^2 e^2 a^2 \sin^2(\theta)}{4\pi c^3}, \tag{2.30}$$

where a is the acceleration of the charge and J is the total radiative power integrated over all frequencies in units of $\mathrm{erg\ s^{-1}}$. To describe the frequency dependence of free-free emission, we first clarify the difference between black body (thermodynamic equilibrium; TE) radiation and thermal (LTE) radiation. The spectral radiance for a medium interacting thermally is given by the Planck [51] Law

$$B(\omega) = \frac{2h\omega^3}{c^2} \frac{1}{e^{\hbar\omega/kT} - 1}. \tag{2.31}$$

In thermodynamic equilibrium, interactions are so frequent that final spectrum is independent of the source spectrum. In more diffuse media, temperatures only exist locally (LTE) and Planck radiation is related to the spectra energy density through

the Kirchhoff [52] Law as

$$j(\omega) = B(\omega)\sigma(\omega)n_i, \tag{2.32}$$

where n_i is the number density of the emitting specie. Here Planck radiation is a source rather than the resulting total radiation field. Thus we can recover the form of the free-free emission spectrum from Equation 2.15 to find

$$\frac{d\rho(\omega)_{ff}}{d\Omega} = n_i n_e \left(\frac{2m_e}{3\pi kT}\right)^{1/2} \frac{Z^2 e^6 c}{m_e^2} g_{ff}(\omega) \sin^2(\theta) e^{-\hbar\omega/kT}, \tag{2.33}$$

which is commonly referred to as Bremsstrahlung, or "braking," radiation.

For LTE diffuse emission in general, the specific luminosity is calculated by integrating Equation 2.32 over frequency and dividing the result by the mass density of the emitting particle. For a single molecule, this becomes

$$\frac{L_i}{m_i} = \frac{8\pi^5 k^4}{15c^2\hbar^3} \frac{M_i \langle\sigma\rangle_{B(T)} T^4}{N_A}, \tag{2.34}$$

where N_A is Avogadro's Number, M_i is the molar mass for particle i, and $\langle\sigma\rangle_{B(T)}$ is the Planck-averaged absorption cross section, which is an implicit as well as an explicit function of temperature. As shown in Figure 2.1, this relationship is therefore not a power law as one may expect from the T^4 dependence. Deviations from that relationship are due to both the effect of photochemical balance and the frequency dependence of the absorption cross section.

A statistical mechanical framework for a many-body system like a volume of astrophysical phenomena is required to determine the transport of radiation and other energies. Thus, the assumption of LTE in many of the preceding equations is often required to produce analytical descriptions of dynamic phenomena and is difficult to escape entirely. We are being strict in our definition of LTE as the existence of a temperature, however. The combination of diffuse absorption, scattering, and emis-

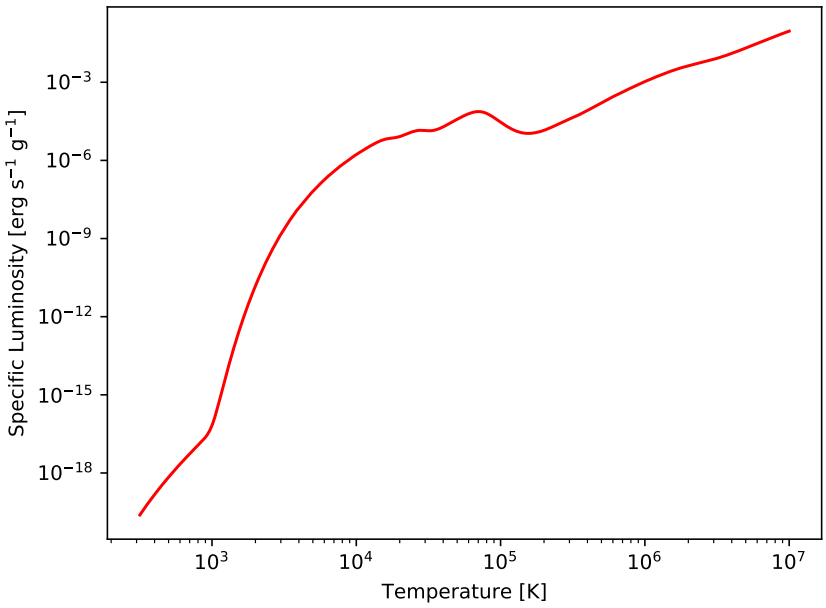

Figure 2.1: Gas specific luminosity versus temperature (Equation 2.34) for primordial abundances of hydrogen and helium in photochemical balance.

sion mechanisms described here would be referred to as "non-LTE" in some literature because the result would diverge quite significantly from the shape of the Planck distribution. We make this point to emphasize that our semantic choices are not automatically equivalent to making a gross simplification.

For example, though we use Kirchoff's Law to determine emission, we carefully apply it on a per-specie basis so that effects like photo and thermal ionization are explicitly included. This is exemplified by the non-Planck shape of the curve in Figure 2.1 as discussed. We are also free to define a different temperature for each ionization state of each particle as required. Some of our assumptions do break down when particles interact so infrequently that temperatures no longer exist, which is not uncommon in astrophysical contexts. However, since specific luminosity (Equation 2.34) and the collision frequency (Equation 2.7) are both proportional to the number density of the particle, the non-existence of a temperature also implies a marginal

impact on the spectra, which mitigates the error induced by an assumption of LTE.

2.1.4 Point Sources

Radiation from stars and compact objects are treated as point sources at astrophysical distances. We can easily convert between a point source and the spectral density with the relationship.

$$j(\omega) = \frac{L_\omega(\omega)}{4\pi}\delta^3(\vec{r}), \tag{2.35}$$

where $\delta^3(\vec{r})$ is a three-dimensional Dirac delta function that has null value everywhere but at the source's position $\vec{r}$ and $L_\omega(\omega)$ is the spectral luminosity in units of erg s^{-1} Hz^{-1} at frequency ω. The total luminosity of the point source, L, is recovered from the spectral luminosity by integrating over all frequencies.

2.1.4 Stars

Stars are well approximated as blackbodies in thermal equilibrium that have intrinsic spectra close to the Planck distribution given by Equation 2.31. This spectra is processed by metals in the star and the stellar photosphere to produce metallicity and temperature-dependent absorption characteristics. The Morgan et al. [53] stellar classification scheme is used by astronomers to group stellar objects by signatures in their spectra. For metal-enriched stars, temperature becomes a proxy for both spectra and classification. When plotting luminosity versus temperatures for the Gliese and Jahreiß [1] sample of of nearby stars to form a Hertzsprung [54] and Russell [55] diagram, stars are observed to be grouped into the main sequence and giant branches as shown in Figure 2.2, where spectral classes are indicated above the plot.

Stars in the main sequence roughly follow the empirical luminosity relationship

$$\frac{L}{L_\odot} \propto \left(\frac{M_\star}{M_\odot}\right)^\alpha, \tag{2.36}$$

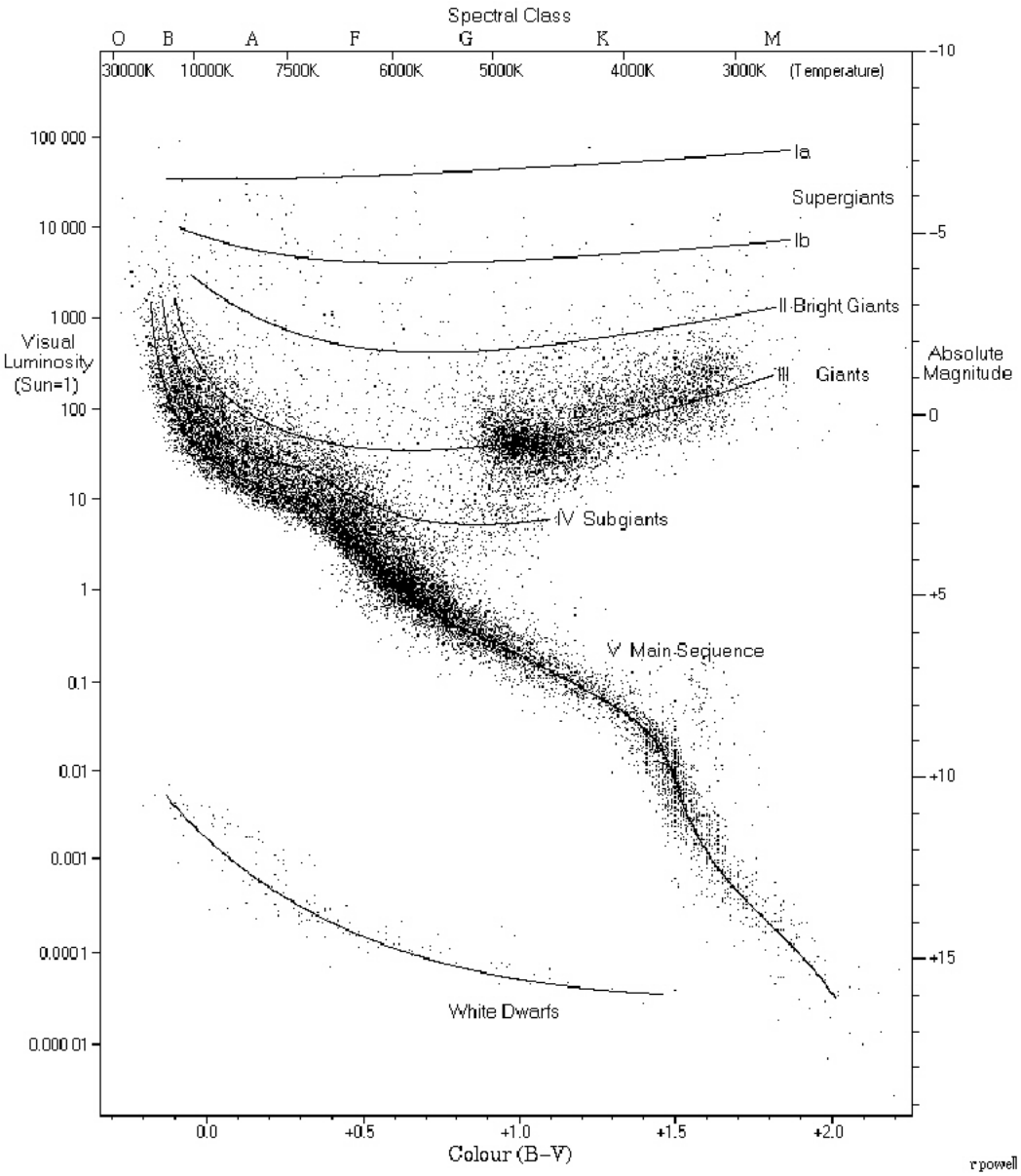

Figure 2.2: Hertzsprung-Russell diagram from the Gliese and Jahreiß [1] catalog of nearby stars produced by Richard Powell.

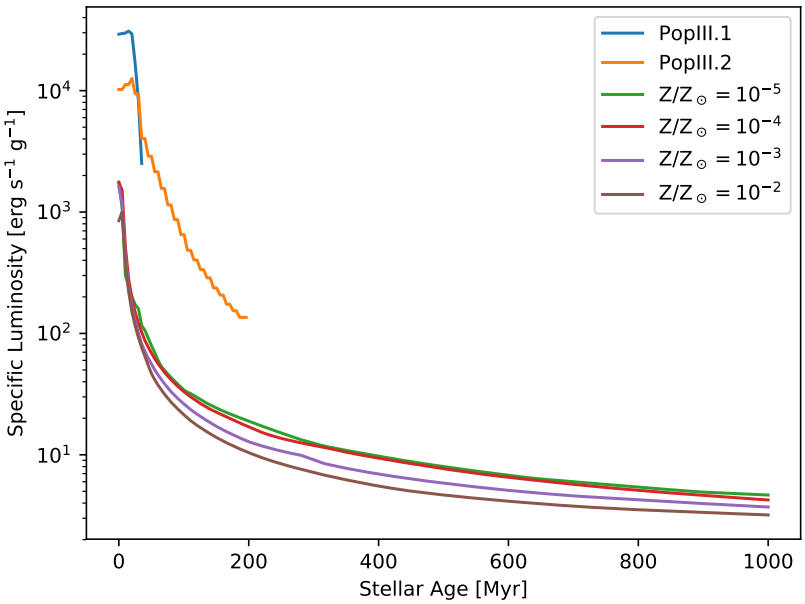

Figure 2.3: Specific luminosity of stars by metallicity. Population III specific luminosities for the PopIII.1 and PopIII.2 IMF prescriptions are presented.

where $2.5 \leq \alpha \leq 6$ depending on stellar classification. Since the mass and temperature of individual stars vary with time, it is useful to describe luminosity as a function of the metal content of their birth cloud and their age. Several population synthesis models accomplish this task[e.g. 56–58]. Figure 2.3 shows a time evolution of the initial mass function (IMF)-averaged specific luminosity for various metallicities as calculated by Conroy and Gunn [59] for Population II stars as well as the top-heavy PopIII.1 and bottom-heavy PopIII.2 IMF models used in Zackrisson et al. [60] for Population III stars. For reference, the specific luminosity of the sun is $1 L_\odot / M_\odot \approx 1.96$ erg s^{-1} g^{-1}.

2.1.4 Accretion onto Black Holes

Material accreting into black holes convert some fraction, ϵ, of their gravitational potential energy into radiation. The resulting radiation pressure on the incoming gas in turn regulates the accretion rate. The Eddington [61] formula for the radiation-

limited accretion rate onto compact objects is

$$\dot{M}_{\rm Edd} = \frac{4\pi G M_{\rm bh} m_p}{\epsilon c \sigma_T}, \tag{2.37}$$

where $M_{\rm bh}$ is the mass of the black hole, σ_T is the Thomson scattering cross section given in Equation 2.28, m_p is the mass of a proton, and ϵ is taken to be around 10%[62]. The corresponding Eddington luminosity is

$$L_{\rm Edd} = \epsilon \dot{M}_{\rm Edd} c^2. \tag{2.38}$$

Bondi and Hoyle [63] showed that the limiting accretion rate onto a compact object based purely on orbital dynamics and conservation of momentum is given by

$$\dot{M} = \frac{\lambda_{\rm BL} \pi G^2 M_{\rm bh}^2 \rho_\infty}{v_\infty^3}, \tag{2.39}$$

where $\lambda_{\rm BL}$ is a constant, G is the gravitational constant, ρ_∞ is the density of the local unbound medium, and v_∞ is the hyperbolic excess velocity of the incoming gas, which is equivalently the velocity of the compact body with respect to the local unbound medium. Bondi [64] later showed that the presence of shocks further limits the accretion rate to be

$$\dot{M}_{\rm B-H} = \frac{\lambda_{\rm B} \pi G^2 M_{\rm bh}^2 \rho_\infty}{c_s^3}, \tag{2.40}$$

where $\lambda_{\rm B}$ is again a constant and c_s is the speed of sound in the medium. In the same work, Bondi suggested that one can interpolate between Equation 2.39 and Equation 2.40 in the manner

$$\dot{M}_{\rm Bondi} = \frac{\lambda \pi G^2 M_{\rm bh}^2 \rho_\infty}{(c_s^2 + v_\infty^2)^{3/2}}, \tag{2.41}$$

where Shima et al. [65] have argued that the constant λ, which depends on the ratio of specific heats, should be close to four for astrophysical media. Each of the three

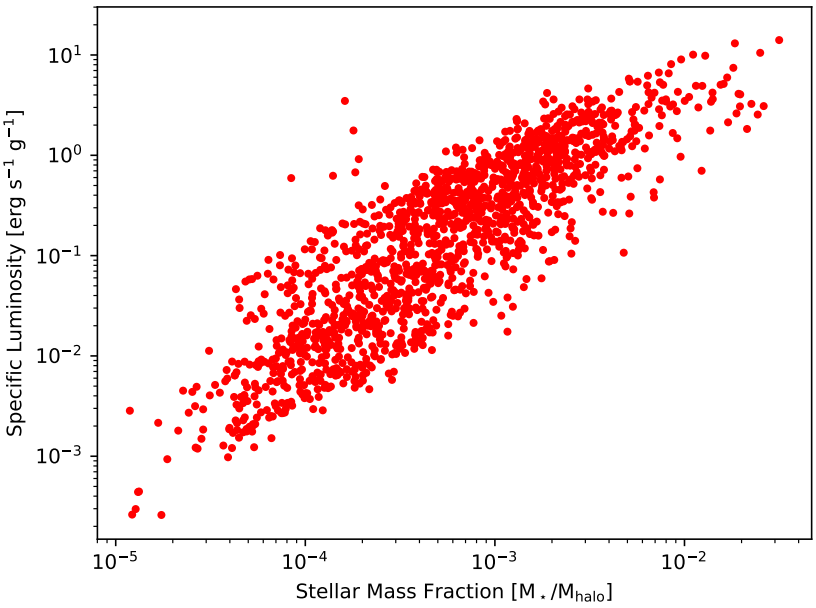

Figure 2.4: Galaxy specific luminosities versus stellar mass fraction for haloes in the "rare peak" of the Renaissance Simulations[2] at $z = 15$.

proceeding equations and Equation 2.37 assume a spherically symmetric flow in equilibrium. However, angular momentum conservation tends to collect accreting media into a disk over time[62, 66], which would necessarily lead to changes in the accretion rate. Also, if the Bondi limit is much larger than Eddington limit ($\dot{M}_{\rm Bondi} \gg \dot{M}_{\rm Edd}$), the flow may undergo periods of super-Eddington accretion.

To determine the frequency dependence of the compact body emission spectrum, we first define the Schwarzschild [67] radius, $r_{\rm s}$, as

$$r_{\rm s} = \frac{2GM_{\rm bh}}{c^2}. \tag{2.42}$$

The effective temperature profile of a black hole with a Shakura and Sunyaev [62]

accretion disk in thermodynamic equilibrium is

$$T_{\text{eff}}(r) = \left[\frac{3GM_{\text{bh}}\dot{M}}{8\pi\sigma r^3} \left(1 - \sqrt{\frac{6r_{\text{s}}}{r}} \right) \frac{6r_{\text{s}}}{r} \right]^{1/4}, \tag{2.43}$$

as described in Ebisawa et al. [68], where the black body temperature is $T_{\text{col}}(r) \approx 1.7T_{\text{eff}}(r)$ due to the Compton effect on the disk. The total disk spectrum is therefore

$$j(\omega) = \delta^3(\vec{r}) \int_{r_{\text{s}}}^{\infty} B(\omega, T_{\text{col}}(r)) 2\pi r dr, \tag{2.44}$$

which is commonly referred to as the multi-color disk (MCD) spectrum. However, observed active galactic nuclei spectra also contain a component of hard X-ray photons due to further Componization of photons by hot electrons in the corona, which can be expressed as a power law with an exponential cut off of the form

$$j(\omega) = \frac{\delta^3(\vec{r})}{4\pi} N_{\text{P}} \left(\frac{x}{T} \right)^{-\alpha} \frac{e^{-x/T}}{x}, \tag{2.45}$$

where $x = \hbar\omega/m_e c^2$, α is the power law slope, and N_{P} is a normalization[69]. The ratio of the power law component to the disk component in the non-relativistic limit is

$$\frac{J_{\text{PL}}}{J_{\text{MCD}}} = \frac{\Gamma(\alpha)}{\Gamma(2\alpha + 3)} \tag{2.46}$$

for both optically thin and optically thick plasmas, where Γ is an Euler gamma function and the slope, α, asymptotically decays from ~ 2.5 to 1.75 for higher accretion rates[70].

2.1.4 Relative Strength of Emission Sources

The specific intensity of galaxies generally increases with stellar mass fraction at high redshift as shown in Figure 2.4. Though these values imply that continuum diffuse emission is relatively unimportant except for hot haloes with extremely low stellar

mass fractions, the luminosity density is usually concentrated into prominent nebular emission lines in the spectra of most galaxies. Diffuse emission is also important because reprocessed incident radiation may drastically reshape the spectra in some cases without causing a change in the bolometric luminosity.

2.1.5 Constructing the Equation

A radiation field expanding isotropically in a flat, non-moving, non-expanding space time is described by the continuity expression

$$\frac{\partial j(\omega)}{\partial t} + c\hat{n} \cdot \nabla j(\omega) = S(\omega), \tag{2.47}$$

where $S(\omega)$ is a source function that includes absorption, scattering, and emission. Assuming the FRW metric, the radiative transfer equation in the cosmologically expanding comoving frame becomes

$$\frac{\partial i(\omega)}{\partial t} + \frac{\partial}{\partial x^i}(\dot{x^i} i(\omega)) - H\left[\omega \frac{\partial i(\omega)}{\partial \omega} - 3i(\omega)\right] = S(\omega), \tag{2.48}$$

as derived in Gnedin and Ostriker [71], where x^i are comoving coordinates. Here, the third term describes the Doppler shift and aberration of the intensity due to cosmological expansion.

We note that Equation 2.48 still retains the assumption that the medium is stationary in the expanding frame, which is valid for low-velocity flows. For relativistic flows, we define $\beta = v/c$, $\gamma = 1/\sqrt{1-\beta^2}$, and $\mu = \cos(\phi)$ where ϕ is the angle between photon's velocity vector and that of the flow. We also restrict the equation to a one-dimensional photon trajectory along a geodesic and assume that the flow is locally homogeneous ($\partial\beta/\partial t = \partial\beta/\partial r = 0$), which is useful for many computational applications where a grid or mesh of physical attributes is used. To $O(\beta)$, the radiative

transfer equation thus expands to,

$$\begin{aligned}
&\gamma(1+\beta\mu_0)\frac{\partial i(\mu_0,\omega_0)}{\partial t} + c\gamma(\mu_0+\beta)\frac{\partial i(\mu_0,\omega_0)}{\partial r} \\
&+ c\frac{\partial}{\partial \mu_0}\left\{\gamma(1-\mu_0^2)\left[\frac{1+\beta\mu_0}{r}\right]\right\} i(\mu_0,\omega_0) + c\frac{\partial}{\partial \omega_0}\left\{\gamma\omega_0\left[\frac{\beta(1-\mu_0^2)}{r}\right]\right\} i(\mu_0,\omega_0) \\
&+ c\gamma\left\{\frac{2\mu_0+\beta(3-\mu_0^2)}{r}\right\} i(\mu_0,\omega_0) = S_0(\omega),
\end{aligned} \tag{2.49}$$

which is simplified from Mihalas and Mihalas [72]. Here, the naught subscript denotes terms in the frame of the medium and the distance variable, r, is the length along the locally homogeneous region. Equation 2.49 is therefore comoving with respect to a volume of media, but does not include terms for cosmological expansion such as the Hubble constant. However, there is no need to find or enforce a consistency between this equation and Equation 2.48 because each is relevant on entirely distinct spatial scales. The third term in Equation 2.48 only becomes important when considering a distances approaching the Hubble length, $c/H(z)$. Over which, the fine details of the relativistic flows described in by the terms in Equation 2.49 become little more than point sources and may be handled equivalently by absorption and emission terms in the source functions on the right hand side of Equation 2.47 or Equation 2.48 at large and very large scales, respectively.

Conversely, at the scale of a galaxy, significant Hubble expansion takes much longer periods of time than it takes photons to traverse the medium and thus expansion terms usually become irrelevant, whereas the velocity-dependent details of radiation hydrodynamics as light is absorbed and emitted throughout the medium are more important. One notable exception to this dichotomy are frequencies with high absorption cross sections and albedos where photons undergo a large number of scatterings before eventually Doppler shifting out of the absorbing frequency and escape a dense region. This scenario usually requires a dedicated modeling approach[e.g. 73, 74].

Returning to the source function, we define the absorption opacity, $\kappa(\omega)$, as

$$\kappa(\omega) = \sum_i \sigma_i(\omega) n_i, \tag{2.50}$$

where $\sigma_i(\omega)$ is the absorption cross section for mechanism i at frequency ω and n_i is the number density of the corresponding absorbing particle. The mean albedo is defined as

$$\bar{\alpha}(\omega) = \frac{\sum_i \alpha_i(\omega)\sigma_i(\omega)n_i}{\kappa(\omega)}, \tag{2.51}$$

and the source functions is constructed from these quantities as

$$\frac{S(\omega)}{c} = j(\omega) + \kappa(\omega)i(\omega)(\bar{\alpha} - 1). \tag{2.52}$$

We can rewrite the second term in Equation 2.48 as $c\hat{n} \cdot \nabla i(\omega)/(1+z)$ since the speed of light is constant. Thus, we finally write the full radiative transfer equation for cosmologically expanding coordinates and derivatives as

$$\frac{1}{c}\frac{\partial i(\omega)}{\partial t} + \frac{\hat{n} \cdot \nabla i(\omega)}{1+z} - \frac{H}{c}\left[\omega\frac{\partial i(\omega)}{\partial \omega} - 3i(\omega)\right] = j(\omega) + \kappa(\omega)i(\omega)(\bar{\alpha} - 1). \tag{2.53}$$

2.2 Numerical Solution Methods

We employ two numerical methods to solve the radiative transfer equation in subsequent chapters. The first is a self-consistent adaptive ray tracing routine run "on the fly" within ENZO, which models monochromatic absorption along rays from point sources and couples directly with the hydrodynamics. The second is a post-processed Monte Carlo simulation that calculates scattering, diffuse emission, and reprocessing for a range of frequencies. We review the methodology of both routines for reference.

2.2.1 Adaptive Ray Tracing (Enzo)

Ray-tracing is generally defined as the tracking of light along a vector. To use this technique within a grid-based cosmological simulation, a ray between each source and each illuminated cell needs to be calculated. Because the scale of cosmological simulations is usually large enough to require time-dependent tracing along a ray, the number of illuminated cells and thus the number of required rays increase with time.

Abel and Wandelt [75] devised an adaptive technique that takes the normals of an Hierarchical Equal Area isoLatitude Pixelation[HEALPix; 76] of a sphere to scatter rays. Rather than trace rays from the source towards each cell, a small number of rays is used to impinge adjacent cells, which split as the ray density decreases. Therefore, only absorption calculations along a path length of cdt are required rather than along the entire distance from the source to the illuminated cell, which saves computational time. This saving is continuously realized for radiation sources that have time-dependent luminosities as well as for cells that have time-dependent compositions.

However, the number of required rays scale linearly with the number of photon energy bins. This necessitates a conservative and considered approach to spectrum modeling. Wise and Abel [77] evolved and advanced adaptive ray tracing in Enzo by introducing prescriptions for several physical phenomena, of which a few are described below. The form of the radiative transfer equation used in Enzo is

$$\frac{1}{c}\frac{\partial P}{\partial t} + \frac{\partial P}{\partial r} = -\kappa P, \tag{2.54}$$

where P is a super-photon particle that represents a unit of energy radiating along a ray. The left side of Equation 2.54 can be reposed as

$$\frac{\partial P}{\partial t}\frac{dt}{dr} + \frac{\partial P}{\partial r}\frac{dr}{dr} = \frac{dP}{dr}. \tag{2.55}$$

Since physical quantities are fixed within an Enzo cell, the photon number lost as the particle crosses a cell is simply

$$\Delta P = P(1 - e^{-\sigma n \Delta r}). \tag{2.56}$$

To properly calculate these quantities with a finite number of rays and photons, each particle needs to impinge gas for some radius about the center of the ray. Thus, the energy contained in one particle affects some covering fraction of each cell along the ray, imparting energy. This energy can be used to drive a number of changes within the simulation. For example, the radiation pressure on the gas is

$$\Delta \mathbf{p} = \frac{\Delta P E_{\rm ph}}{c} \hat{r}, \tag{2.57}$$

where $\Delta \mathbf{p}$ is the change in momentum, $E_{\rm ph}$ is the energy of a photon, and $\hat{r}$ is the direction of the photon's velocity. Similarly, the photo-heating rate, $\Gamma_{\rm ph}$, is approximated by

$$\Gamma_{\rm ph} = \frac{\Delta P (E_{\rm ph} - E_i)}{n_i V_{\rm cell} \Delta t}. \tag{2.58}$$

If managed carefully, discrepancies between a spherically diverging source and a Cartesian grid can be mitigated through geometric arguments for the ray covering fraction. Wise and Abel [77] found that their prescription requires only one ray per cell to adequately capture the radiation-hydrodynamics without artifacts when the media is assumed to be optically thin.

2.2.2 Monte Carlo (Hyperion)

Lucy [78] first proposed a technique of solving both diffuse emission and absorption for a radiative transfer equation functionally equivalent to Equation 2.47 by iteratively converging the emitted and absorbed energy rates. The initial estimate for the

absorption rate of the system is given as

$$\dot{A} = \frac{E_{\text{part}}}{\Delta t V_{\text{cell}}} \sum \kappa(\omega) \Delta l, \tag{2.59}$$

where E_{part} is the energy of a super-photon particle and Δl is the path length of the particle across the cell. The total power emitted by the medium assumed to be at temperature T is approximately

$$\dot{E} = 4\sigma_{SB} \langle \sigma \rangle_{B(T)} T^4, \tag{2.60}$$

where σ_{SB} represents the constants in the forward fraction of Equation 2.34. Unless the incoming radiation is described by Equation 2.31, the value of $\dot{E}$ and the value of $\dot{A}$ will be different for the first iteration. For the second iteration, the subsequent temperature estimate, T_{i+i}, can be derived from the absorption rate as

$$T_{i+1} = \sqrt[4]{\frac{\dot{A}}{4\sigma_{SB} \langle \sigma \rangle_{B(T)}}}, \tag{2.61}$$

which can be used to recalculate the Planck mean absorption coefficient and recalculate $\dot{E}$ until an effective convergence with $\dot{A}$. Lucy [78] shows that this can occur in as few as two or three iterations and preserves the radial distribution of luminosity.

HYPERION[79] uses pre-computed tables of the Planck mean opacity and emssivities as a function of $\dot{A}$ and thus eschews temperature as an intermediary of the calculation. HYPERION quickly solves an LTE balance and can output temperature if requested. However, the resulting emissivity changes the frequency dependence of the radiation field which in turn changes $\dot{A}$ so several iterations are needed to bring the two in balance throughout a non-homogeneous medium. This method is too computationally expensive to couple with a hydrodynamic simulation, but is well-adapted to producing mock photometry and spectrometry.

Having now established a theoretical background to treatments of radiative transfer, the next chapter begins with a literature review of deep field astronomy, cosmological simulations, and synthetic observations before introducing our own methodology and results.

CHAPTER 3
EXPLORING THE SPECTRA OF HIGH-REDSHIFT GALAXIES IN THE RENAISSANCE SIMULATIONS

This chapter describes the methodology and implementation of a synthetic observation modeling pipeline to a large, high resolution cosmological simulation. Hereafter is the work as published in the Monthly Notices of the Royal Astronomical Society in August 2017 with John Wise, Michael Norman, Brian O'Shea, and Hao Xu as coauthors.

We present synthetic observations for the first generations of galaxies in the Universe and make predictions for future deep field observations for redshifts greater than 6. Due to the strong impact of nebular emission lines and the relatively compact scale of H II regions, high resolution cosmological simulations and a robust suite of analysis tools are required to properly simulate spectra. We created a software pipeline consisting of FSPS, Hyperion, Cloudy and our own tools to generate synthetic IR observations from a fully three-dimensional arrangement of gas, dust, and stars. Our prescription allows us to include emission lines for a complete chemical network and tackle the effect of dust extinction and scattering in the various lines of sight. We provide spectra, 2-D binned photon imagery for both HST and JWST IR filters, luminosity relationships, and emission line strengths for a large sample of high redshift galaxies in the Renaissance Simulations[2]. Our resulting synthetic spectra show high variability between galactic haloes with a strong dependence on stellar mass, metallicity, gas mass fraction, and formation history. haloes with the lowest stellar mass have the greatest variability in [O III]/Hβ, [O III] and C III] while haloes with higher masses are seen to show consistency in their spectra and [O III] equivalent

widths (EW) between 1Å and 10Å. Viewing angle accounted for three-fold difference in flux due to the presence of ionized gas channels in a halo. Furthermore, JWST colour plots show a discernible relationship between redshift, colour, and mean stellar age.

3.1 Introduction and Background

The frontier of observations and cosmological simulations has been mostly defined by the limitations of hardware and the fidelity of modelling methods. The epoch of reionization (EoR; $6 \leq z \leq 15$) is both the farthest back space-based observation has seen and the furthest forward large, high-fidelity radiative transfer "first-galaxy" simulations have reached, generating a thin region of overlap where real and synthetic observations may be compared and predicted in greater detail.

3.1.1 EoR Galaxy Observations

The bright UV portion of a young galactic spectrum in the rest frame at $z > 6$ corresponds to the optical and near infrared portion of a spectrum for a present day observer. Thus only telescopes calibrated to observe these and higher wavelengths are appropriate for high-redshift observations. The current cache of operating IR-capable space telescopes include the Wide-field Infrared Survey Explorer (WISE), the Spitzer Space Telescope, and the Hubble Space Telescope (HST). Of the three, the HST's deep field surveys using the UVIS/IR Wide Field Camera (WFC3) provide the most useful data for studies of this epoch.

The Hubble Ultra Deep Field[HUDF; 80] is a culmination of many years of observational campaigns. Several groups have uncovered hundreds of galaxies with redshifts greater than 5 through the Lyman break "drop out" technique[81] that uses photometry with appropriate colour-colour selection rules to high-redshift candidates[80]. In its initial 2005 HUDF campaign, the Hubble Advanced Camera for Surveys (ACS)

used four optical filters to identify galaxies with redshifts up to 7.5, showing that the galaxy number density further declines with redshift[e.g. 82–84].

The HUDF was supplemented with WFC3 observations in 2009, confirming earlier results and extending its reach beyond $z \simeq 7.5$[e.g., 3]. By combining results from optical and near-infrared imaging, this survey used SED fitting to catalogue and confirm 49 candidate objects between redshifts 6 and 9. A subsequent campaign in 2012 with longer exposure times and through more filters, dubbed the Hubble Extreme Deep Field[XDF; 85], produced candidates between redshifts 8.5 and 12[4]. The luminosity functions determined from the XDF galaxies show an exponential decay with increasing redshift until approximately $z = 8$[e.g. 85–87] followed by steeper drop off subject to great uncertainty due to the limited number of observations and difficulty confirming their redshifts. Specifically at both the brightest end ($\mathbf{M}_{1600} \leq -22$) and the faint end ($\mathbf{M}_{1600} \geq -17$), the uncertainties between and within fits grow to a several orders of magnitude differences in the number density of objects[88].

The current state of the art is the ongoing Hubble Frontier Fields survey[5] which combines ACS, WFC3 and catalogues of galaxy clusters[89, 90] to resolve gravitationally lensed objects in their vicinity on the sky as seen from the Earth. The survey is designed to probe six clusters to an observed $\mathbf{AB}_{\mathrm{mag}} \sim 29$ which may be magnified 10–100 times in fortuitous alignments with foreground strongly-lensing galaxy clusters.

3.1.2 EoR Galaxy Simulations

Cosmological simulations apply numerical and empirical subgrid prescriptions to a set of cosmological initial conditions at high redshift to produce a physically plausible representation of the Universe. To that end several codes that include star formation and feedback, radiative transfer, and hydrodynamics routines have been developed. However, as the routines became more physically representative, their demands on

computational infrastructure constrain their resolution and scope. Where small-scale and zoom-in simulations are capable of astounding spatial resolution, accurate accounting for physical phenomena in large-scale cosmological simulations implies the propagation of radiation and the interaction of processes that occur simultaneously on a variety of time and spatial scales from atomic to cosmological.

To achieve appropriate and efficient scale, cosmological simulations generally employ either smooth particle hydrodynamics (SPH) or adaptive mesh refinement (AMR). In addition to the body of work using SPH or AMR, some simulations employ moving mesh codes such as Arepo[91] and meshless codes such as Gizmo[92]. SPH simulation codes such as Gadget[93] and Gasoline[94] initialize mass as a distribution of particles which evolve hydrodynamically into high and low density regions. Fluid dynamics and other calculations are then smoothed over a fixed number of nearby particles, generating a density-dependent spatial resolution for physical calculations. Conversely, AMR codes such as enzo[33] and Ramses[95] initialize a uniform mesh of initial quantities and attributes where calculations of physical processes are calculated within and between each constant-quantity cell of the mesh. Based on one or more user-defined parameters which may include density, cells are further divided into smaller regions as needed to track regions that require higher spatial resolution. Studies indicate that the results of these two methods are similar with discrepancies owning mostly to their sub-grid physics models[96–98].

Examples of high-redshift galaxy simulations with high physical fidelity, radiative transfer, and high resolution are represented by the Renaissance Simulations[2, 99] used in this work, the Aurora Simulation[100], the BlueTides Simulation[6], the First Billion Years Project[7], and a recent radiative transfer-modified Ramses simulation by Katz et al. [101].

3.1.3 Synthetic Observations

Using the HUDF and two different sets of parallel fields, Bouwens et al. [86] and Finkelstein et al. [102] constrained luminosity functions up to redshift 8 and down to $\mathbf{M}_{1600} \simeq -17$ within the EoR. By using gravitational lensing, the luminosity functions from the Frontier Fields extend the steep faint-end slope out to $M_{\mathrm{UV}} \simeq -12.5$ at $z \sim 6$ and -14 at $z \sim 7-8$ with no apparent flattening[103–105]. The luminosity function of objects in the Renaissance Simulations[2] likewise converged on $\mathbf{M}_{1600} \simeq -17$ from the faint end of the luminosity function, closing a long-standing gap between the dimmest observable EoR objects observed and the brightest objects produced in "first galaxy" cosmological simulations. This convergence is timely for the creation of synthetic observations that can be directly compared to images from the HUDF and the Frontier Fields.

Unfortunately, the characterization of observations of individual objects at high redshift is sometimes difficult due to the complex geometry of emission from early galaxies and their distance. For example, objects such as CR7 were initially characterized as a possible Population III galaxy[106] or evidence of a direct collapse black hole[107–110], but further study produced evidence to dispute both claims[111]. Due to stellar feedback and a high merger rate, the morphology of large early galaxies is irregular and exhibit high variability with respect to the observer's viewing angle. These galaxies have bursty star formation and relatively high UV escape fractions[112], making for a non-trivial star formation history. Observations from the Atacama Large Millimetre/Submillimetre Array (ALMA) further suggest that galaxies at high redshift ($6 \lesssim z \lesssim 8$) may exhibit higher metallicities and dust content that previously thought[113, 114], emphasizing the need for a robust dust model.

To generate synthetic observations of objects like CR7, a full 3D model of stellar populations as well as gas and dust extinction is therefore desired. Furthermore, more capable space telescopes like the forthcoming James Webb Space Telescope (JWST)

are required to better study these objects and explore a more statistically significant sample size of early-universe galaxies.

Telescopes observing this epoch are limited by the spectral and pixel resolution of their detectors and can thus produce photometry and low signal to noise spectra data that requires extensive fitting to templates produced by theory. On the other hand, simulations are particularly suited to exactly calculate values that can only be empirically determined from observations such as a star formation history, mass to light ratios, column densities, and high-resolution spectra. This work seeks to provide a suite of such measures for the large sample of galaxies in the Renaissance Simulations to provide context for observations as well as demonstrate the variability that comes with viewing angles and formation history. Similarly we hope to use observations to provide context and constrain uncertainties in the subgrid models used in cosmological simulations.

We provide an overview of the physics modelling and simulation setup of the Renaissance Simulations and our own post-processing radiative transfer routines through a dusty medium in Section 3.2 and discuss our methods for the production of synthetic observations and measures. We then analyse two individual galaxies and then provide aggregate measures such as composite spectra and line ratios for the entire sample in Section 3.3. Finally we discuss our results and compare it to recent work on synthetic observations and emission lines in Section 3.4.

3.2 Research Methods

3.2.1 Simulation Techniques

The Renaissance Simulations use individually run "zoom-in" subvolumes to produce an effective total resolution of 4096^3 in a comoving box of size $(40\ \mathrm{Mpc})^3$ using the hydrodynamic AMR code ENZO. The simulations are run using $\Omega_M = 0.266$, $\Omega_\Lambda = 0.734$, $\Omega_b = 0.0449$, $h = 0.71$, $\sigma_8 = 0.8344$, and $n = 0.9624$ from the 7-year WMAP

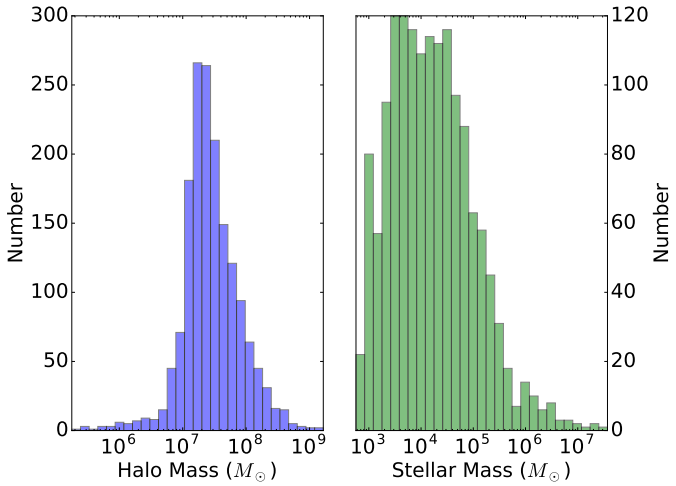

Figure 3.1: Halo number counts in the Renaissance Simulations rare peak region for star-hosting haloes as a function of halo mass (left) and stellar mass (right).

results[115] with standard definitions for each variable. We analyse results from the "rare peak" zoom-in region of the Renaissance simulations with a top grid dimension of 512^3 centred about the Lagrangian volume of two 5×10^{10} $M_\odot$ haloes at $z = 6$. Due to the large size of the simulation, a large sample of 1654 galaxies are available for our analysis with an effective dark matter resolution of 2.9×10^4 $M_\odot$ at $z = 15$ and a spatial resolution of 19 comoving parsecs. In the rare-peak zoom-in region, the most massive halo has a total mass of 1.62×10^9 $M_\odot$ and a stellar mass of 1.55×10^7 $M_\odot$ at $z = 15$. We provide histograms of total and stellar mass of all star-hosting haloes in Figure 3.1. The Renaissance Simulations capture the formation of haloes and their star formation above 3×10^6 $M_\odot$ with more than 100 particles, resulting in an incomplete halo sample below this mass[99, 116]. However, haloes start to form metal-enriched stars above 10^7 $M_\odot$, as shown in the left panel of Figure 3.1, well above this resolution limit. Thus, the drop off in number counts at low mass is caused by physical feedback effects, not lack of resolution.

3.2.1 Star Formation Model

We use the Abel et al. [117] Population III star formation and the Wise and Cen [118] radiative stellar cluster routines to simulate the effect of star formation, radiative and supernovae feedback on the cosmological environment.

We trigger Population III star formation within a converging gas flow when the H_2 fraction exceeds 10^{-4}, the metallicity fraction is below 10^{-4} $Z_\odot$, and the baryon overdensity exceeds $5{\times}10^5$. Population III stars are assigned a random mass according to the distribution

$$f(\log M)dM = M^{-x}\exp\left[-\left(\frac{M_c}{M}\right)^{\beta}\right]dM, \tag{3.1}$$

Furthermore, we set the minimum mass for Population III stars to 5 $M_\odot$ and limit the maximum mass to 300 $M_\odot$.

Whereas the Population III star formation routine produces star particles representing individual stars, it is currently computationally prohibitive to model every metal-enriched star in a cosmological simulation so we employ a radiative stellar cluster routine. For gas with a metallicity above above 10^{-4} $Z_\odot$, we trigger the creation of a star particle once a collapsing region has the properties of a molecular cloud, having a density corresponding to a dynamical time of 3×10^6 yr ($\sim 5 \times 10^{-22}$ g cm^{-3}) and would form a particle with a minimum mass of 1000 $M_\odot$ assuming that it inherits 7% of the cold gas in the star-forming cloud. Each particle therefore represents an entire star cluster with a distribution of individual stars.

In both routines, each star particle inherits the metallicity of its accreted gas and injects metals into the surrounding medium after a supernova. The Population III model triggers a pair-instability supernova for stars with masses between 140 and 260 $M_\odot$ and a Type II supernovae for stars between 11 and 40 $M_\odot$[119] at the end of a mass-dependent lifetime[120]. For metal-enriched stars, we inject 6.8×10^{48} erg $M_\odot^{-1}$ over the 20 Myr lifetimes of the star particle[121] and initialize the supernovae in a

resolved blast wave of radius 10 pc.

3.2.1 Radiative Transfer and Chemistry Model

To include the effects of photoionization and photo-heating, we solve the radiative transfer equation using ENZO+MORAY[77]. We apply a time-dependent Lyman-Werner radiation background[119, 122] and we use the star particles created from our star formation routines as point sources of Lyman-Werner and ionizing radiation. To reduce the computational load of ray-tracing individual photons throughout the simulation volume, we use an adaptive ray-tracing[75] scheme applying the Hierarchical Equal Area isoLatitude Pixelation (HEALPIX)[76] of a sphere to split photons as they travel from the source. This scheme subdivides the surface of a sphere into 12 equal area pixels that can be further divided by factors of 4 resulting in $12 \times 4^{\text{level}}$ equal area pixels. Photons travel along the normal of the HEALPIX pixels until they are split into higher HEALPIX levels when the number of photons per cell falls below 5.1.

For metal-enriched star clusters, we assume each star particle generates 1.12×10^{46} erg $\mathrm{M}_{\odot}^{-1}$ of ionizing radiation at 21.6 eV in a monochromatic spectrum. This implicitly assumes that radiating stellar clusters follow a Salpeter IMF with mass cut offs at 0.1 and 100 $\mathrm{M}_{\odot}$. Population III star particles are given ionizing luminosities consistent with their mass[120]. We also solve for the abundances of nine species (H I, H II, He I, He II, He III, e^-, H^-, H_2^+, H_2) with a non-equilibrium solver[123] that uses the chemical energy of each cell and a look-up table for metal cooling rates[124] produced by the photoionization solver CLOUDY[125].

3.2.2 Halo Analysis

We use the dark matter halo-finding code ROCKSTAR[126] to generate a master list of self-gravitating bound regions. We then use CONSISTENT TREES[127] to produce

a halo merger tree. We then further process the trees using YT[128] and a merger tree organizing code written for this project to create a time-ordered list of position and radii during halo assembly.

Because self-gravitating regions may exist inside of larger haloes, our code takes the raw merger trees and removes these sub-haloes by treating the encompassing region as a single halo with the largest virial radius of the mutually bound haloes to create a new halo list. Using the new list, our code reconstructs the merger tree by assuming haloes are merged once their center falls within the virial radius of a largest of the merging haloes. The tree then continues from this halo after a merger. Using this method, the mass of a halo is calculated as the total mass of dark matter, gas, and star particles within a sphere with a radius equal to the virial radius taken from Rockstar and may include mass from more than one halo from the original tree.

3.2.3 Spectrum Building

Having modelled stellar clusters, metals, temperature, gas, and radiation throughout our simulation, we are left with a rich source of cosmological data with which to generate synthetic spectra. In our model, we treat each star particle as a star cluster consisting of a probabilistic distribution of radiation in frequency space based on models using the metallicity and age-dependent Flexible Stellar Population Synthesis code[FSPS; 59] which is tuned to be consistent with observations. We model our particles assuming an aggregated mean of observed stars of similar composition and age which is consistent with the probabilistic cluster model used to create metal-enriched star particles and model radiative transfer in the cosmological simulation. This allows us to enforce consistency between stellar feedback in the cosmological simulation and stellar feedback in radiative transfer post-processing. However we note that the mean ionizing energy of photons from stellar population synthesis will be slightly different than the energy assumed in the simulation as the stellar population

evolves from brighter stars with more ionizing photons to dimmer, longer-lived stars with a redder spectra as shown in Figure 3.4 left. We expect this to cause slightly larger than physical ionized regions around older stars in the simulation, but this is tempered somewhat by the overall youth of stellar populations at $z = 15$.

3.2.3 Dust and Gas Model

We use the Monte Carlo ray-tracing code HYPERION[79] to propagate, extinguish, and scatter photons through a dusty medium. To initialize the radiation source, we arrange each star particle within a 3-D grid and apply the bolometric luminosity and spectra calculated with FSPS. We use the full grid hierarchy from the ENZO output to create a derived equivalent AMR grid with a predefined maximum highest level. Due to purely computational limitations, we select the highest grid level that will produce no more than 45^3 cells. Relevant physical quantities are then applied to the derived grid from the corresponding cells in the ENZO output.

For gas extinction, we use CLOUDY to produce an isotropic frequency and density dependent hydrogen opacity relationship and allow HYPERION's intrinsic local thermodynamic equilibrium tool to extrapolate emissivities over a broad specific energy range. We apply this model to the density of neutral hydrogen in each cell of our grid and assume that neutral hydrogen accounts for the greatest component of extinction of the nine species calculated in the cosmological simulation. For dust extinction, we use the Draine [129] ($R_v = 2.1$) model and assume that dust contributes 7% of the mass of metals in a cell. We also assume a solar abundance pattern and weight the metal density of each cell accordingly to produce a dust density. Our model uses 10^8 photons to produce a resultant spectra of 8,000 frequencies from 0.05 to 5 microns. We limit the photon propagation to the virial radius of the galactic halo and assume an optically thin medium to the observer outside of the halo.

3.2.3 Emission Lines

We also consider nebular emission lines from the chemical network in the warm ($T >$ 7000 K) and ionized regions in the vicinity of stellar clusters. While we track nine primordial species and a metallicity field to approximate the ISM and accurately model galaxy formation in the simulation, a more refined model is required to get the full complement of metal emission lines.

Once again, we turn to CLOUDY's photoionization solvers. To generate a high-resolution region for analysis, we reuse the derived AMR grid used for HYPERION to extract gas properties. Using the full spectra from FSPS for each star particle, we sum the spectra and luminosity within each cell and treat the sum as a single source in the cell center.

We use CLOUDY to solve and simulate the full complement of emission lines within each cell, constraining the model inputs to the spectra and luminosity from FSPS, the hydrogen density, and the metallicity using a solar abundance pattern[130] from the cosmological simulation to try to keep our photoionization calculation as close to our cosmological results as possible. Because of the dynamic, non-equilibrium nature of cosmological H II regions, we stop the simulation once the electron fraction reaches a value consistent with the local mean electron fraction from the ENZO chemistry solver rather than let CLOUDY find its own equilibrium. The emission lines from each cell are then summed to produce a single source emission line distribution.

We found that the relative line strengths were mostly invariant for a range of inner gas radii centred around 10^{17} cm within a sample of large haloes with a large number of individual star particles. We therefore assume the gas to have a minimum radius of 10^{17} cm (proper) and maximum radius equal to the half-width of the cell for each calculation of the emission emerging from each cell. Stellar clusters have a dynamic and complicated radial luminosity distribution, but our cosmological simulation only captures entire clusters for metal-enriched stars so we acknowledge the limitation of

this treatment.

Finally, we apply a frequency dependent ratio of the HYPERION resultant flux to the FSPS intrinsic flux to the corrected CLOUDY emission lines consistent with Park et al. [131] to simulate extinction and scattering of lines. We find that this method is more feasible than attempting to use enough photons to simultaneously resolve both emission lines and continuum with HYPERION. Our final spectra includes the sum of the CLOUDY results for each sub-region and the HYPERION results for the entire halo.

3.2.4 Filters, Magnitudes, and Images

3.2.4 Filters

Our analysis includes comparisons between our synthetic spectra as seen through HST and JWST by applying filters to our results. For Hubble, we use filters from WFC3 used for the later HUDF surveys. For JWST we assume the use of the Near-Infrared Spectrograph (NIRSpec) and the Near-Infrared Camera (NIRCam). Additionally, we apply a redshift to our spectrum to allow for direct comparison in the observer's frame. We report the total bolometric luminosity and intensity for telescope filters assuming an optically thin path to the observer outside of the virial radii unless otherwise stated.

3.2.4 Filter Fluxes

We also calculate the absolute and apparent magnitudes in each filter. Since spectra are discretely defined, we use a sum

$$\langle f_\nu(\nu_0)\rangle = \frac{(1+z)\int \frac{L_\nu(\nu_e)}{\nu_e} d\nu_e}{\int d\nu_e} \frac{1}{4\pi d_L^2}, \tag{3.2}$$

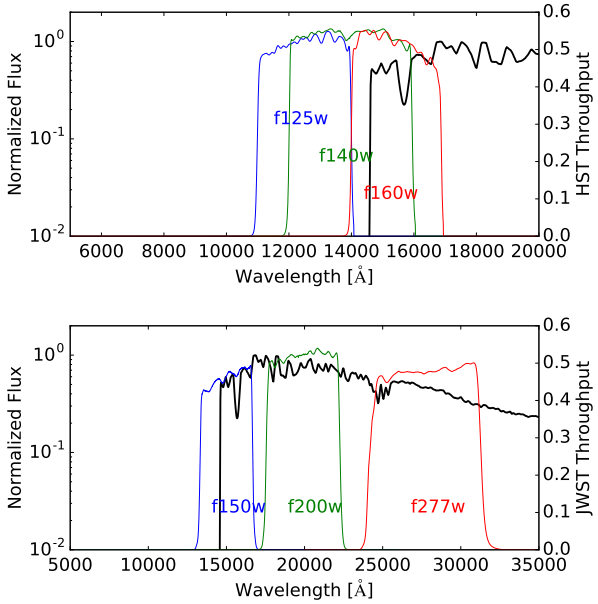

Figure 3.2: A sample synthetic spectra placed at $z = 15$ overlaid with selected HST and JWST filters. From top to bottom: A plot of the overlapping HST WFC3 wide band IR filter throughputs and a plot of JWST NIRCam wide band IR filter throughput, normalized to the largest value in units of erg s^{-1} cm^{-2} $Å^{-1}$.

to estimate the mean flux over the passband where ν_e and ν_0 are the wavelength in the rest and observed frame respectively and d_L is the luminosity distance at a redshift z. The factor of $(1 + z)$ acts to correct for the increase in intensity normally accounted for by the K correction. Filter throughputs are plotted against a sample spectra of an object at $z = 15$ in Figure 3.2.

3.2.4 Synthetic Imaging

Two dimensional images from HYPERION are produced using the built-in method of binning photons from the Monte Carlo gas extinction process at several predefined individual wavelengths. Images produced using this method do not include emission lines produced in nebulae, but include dust and gas scattering and emission as described in Section 3.2.3.1. To produce synthetic observations of early galaxies viewed

at the present day, we process the raw luminosity of each pixel to account for several distance, resolution, noise, and blurring effects.

Our monochromatic flux per pixel is given simply as $F = L(1+z)/(4\pi d_{\rm L}^2)$ presented in units of erg s^{-1} cm^{-2} Hz^{-1}. To account for the observed resolution through an expanding cosmology, we take the angular distance to be $d_{\rm A} = d_{\rm L}/(1+z)^2$. For a given resolution and flat universe, the proper width of a pixel is therefore given by

$$W_{\rm pixel} = d_{\rm A}\theta = \frac{c\theta}{H_0(1+z)} \int_0^z \frac{dz'}{\sqrt{\Omega_{\rm M,0}(1+z')^3 + \Omega_{\Lambda,0}}}. \tag{3.3}$$

Here θ is resolution of the space telescope camera. We use resolutions of 0.065" for NIRcam and 0.15" for WFC3 to resize the native simulated image to the appropriate angular resolution for a given redshift. We apply two interpolation schemes to images to simulate instrument effects. First we apply a Gaussian blur with a standard deviation of five instrument pixels to the image. We then resize the image to the instrument pixel size and applying pixel-binning interpolation to produce the final image. For the purpose of comparison, we provide images in the native resolution of the simulation and the same images after processing.

To account for noise, we assume JWST and Hubble sensitivities of $\sim 10^{-8}$ Jy and $\sim 2.5 \times 10^{-8}$ Jy respectively with a $S/N = 10$ after an exposure time of 10^4 s at the infrared frequencies of interest. We then extrapolate to a 1 Ms (~ 11.6 days) exposure for a final noise value of $\sim 10^{-11}$ Jy. Assuming a Gaussian distribution for noise, we take the mean and standard deviation to be half that value and add the noise flux directly to the image after resizing the pixels.

Since we processed a fixed number of monochromatic images in our initial analysis, the redshifts we present in our images are fixed by the average wavelengths of each filter, $z = \langle \breve{} _{\rm filter} \rangle / \breve{} _{\rm image} - 1$. This results in two to four redshifts in each filter band based on our initial sample of wavelengths. We choose 1500 Å(rest) as the wavelength for

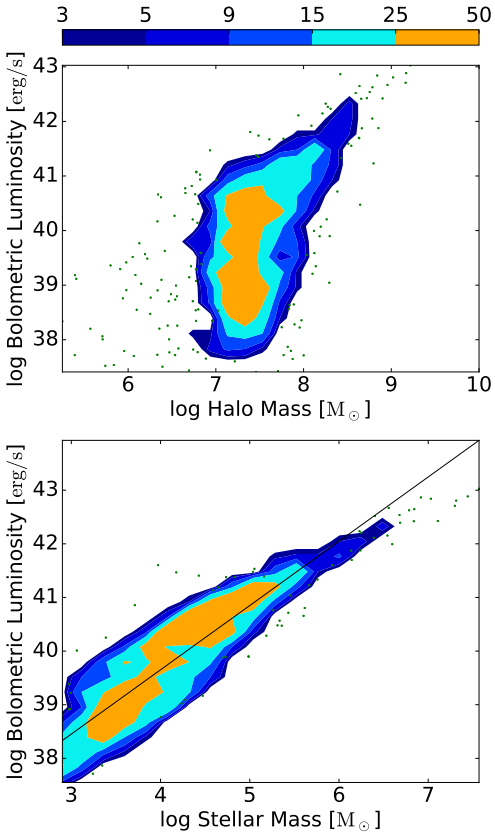

Figure 3.3: Contour histograms and scatter plots of total bolometric luminosity versus halo mass (top) and stellar mass (bottom), showing a wide distribution of luminosities for the haloes with masses below 10^8 $\mathbf{M}_\odot$, however a clear relationship between stellar mass and luminosity is present with the luminosity scatter caused by differing bursty star formation histories.

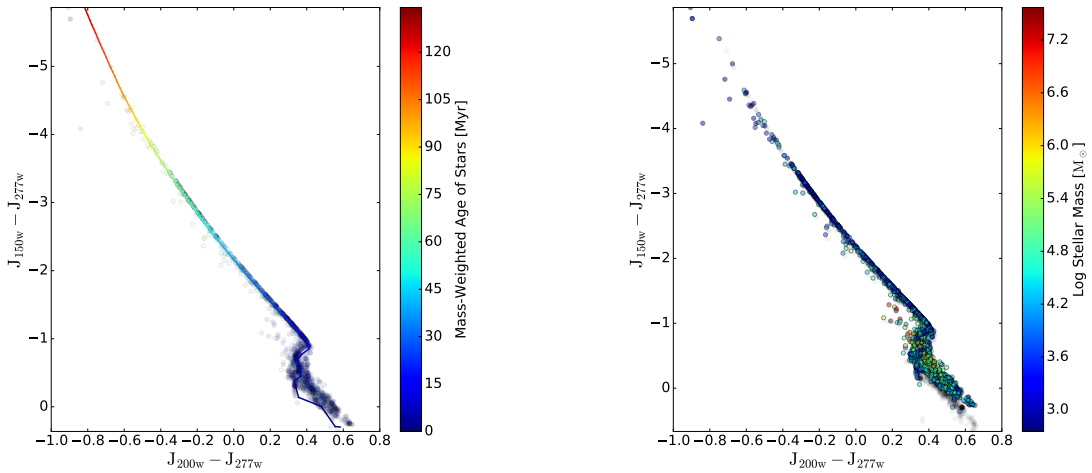

Figure 3.4: Colour-colour plots of star-hosting haloes coloured by their mass-averaged stellar age (left) and stellar masses (right), when the galaxy spectra are redshifted to $z = 15$. The line in the left plot represents the evolution of a single 0.01 $Z_\odot$ stellar cluster coloured by the same range of ages. The grey points right plot represent unprocessed stellar colours which mostly overlap the processed JWST colours with a small offset. Most of the least massive young galaxies lie in a single line as their small stellar populations reliably follow the line, whereas more massive galaxies congregate near J_{200w} - $J_{277w} \sim 0.25$, having a stellar population composed of stars with a variety of ages and metallicities. The mean stellar age plays the biggest role in determining the typical galaxy colours, given the bursty nature of star formation in these high redshift galaxies.

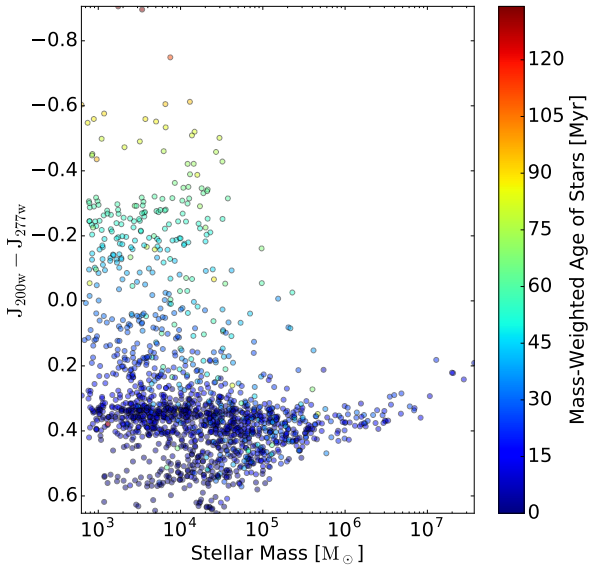

Figure 3.5: Colour J_{200w} - J_{277w} versus stellar mass coloured by the mass-weighted stellar age, assuming $z = 15$, showing a clear trend toward older populations in the least massive galaxies, whereas galaxies with $M_\star \gtrsim 10^6$ $M_\odot$ show a slight decreasing trend with increasing stellar mass.

both the Hubble and JWST filter images to avoid proximity to strong emission lines. We note that this implicitly assumes a similar star formation history for haloes at $8 \leq z \leq 15$ and so we perform this procedure as an exercise with this understanding.

To produce optical composite images, photons are binned at 50 wavelengths between 3800 and 7500 Å(rest). We use a multi-lobe piecewise Gaussian fit of the CIE XYZ colour matching functions[132] for the flux in each pixel and then transform to RGB using the CIE E white point matrix. The intensity of each pixel in the image is then scaled to the power of 1/4 to accentuate light scattering.

3.3 Results

We segregate our results into a section on the aggregate statistics on our entire sample and a section on synthetic observations of two individual large galaxies. For the entire star-containing halo population, we provide luminosity curves, colour-colour plots,

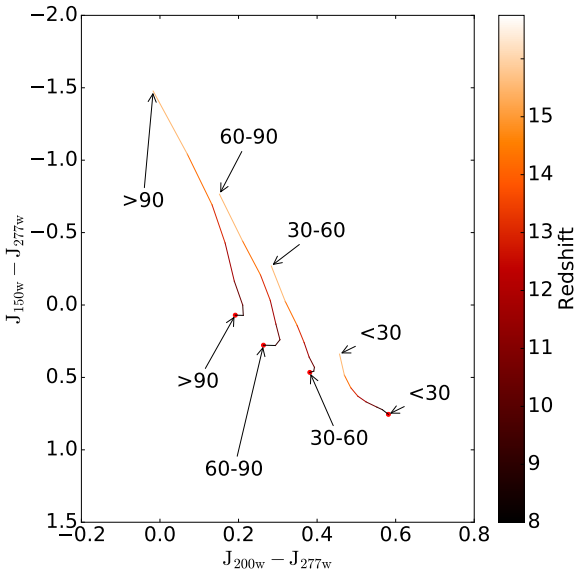

Figure 3.6: The evolution of average colour-colour plot as the spectra are redshifted in the range $z = 8 - 15$ when categorized by mean stellar age in the ranges (in units of Myr) indicated in the plot. The Lyman break causes the reddening in $J_{150w} - J_{277w}$ with redshift, whereas the older stellar populations trend redward in $J_{200w} - J_{277w}$.

emission line ratios and equivalent widths, composite spectra, and BPT diagrams and correlations with stellar mass. For the individual galaxies, we produce synthetic images as seen by HST and JWST and compare to the physical properties of the dark matter halo and the associated galaxy. We also compare weighted mean values for each of these parameters to total flux with respect to viewing angle for the largest galaxy in our simulation.

3.3.1 Aggregate Halo Statistics

Our sample of 1654 galaxies allow us to explore the distribution of spectra, emission lines, and luminosity of haloes with respect to their mass and composition. Figure 3.3 shows the bolometric luminosity distribution of our sample with respect to halo and stellar masses. haloes between 10^7 and 10^8 $M_\odot$ form the boundary between star containing galaxies and non-luminous haloes due to both the inefficient cooling

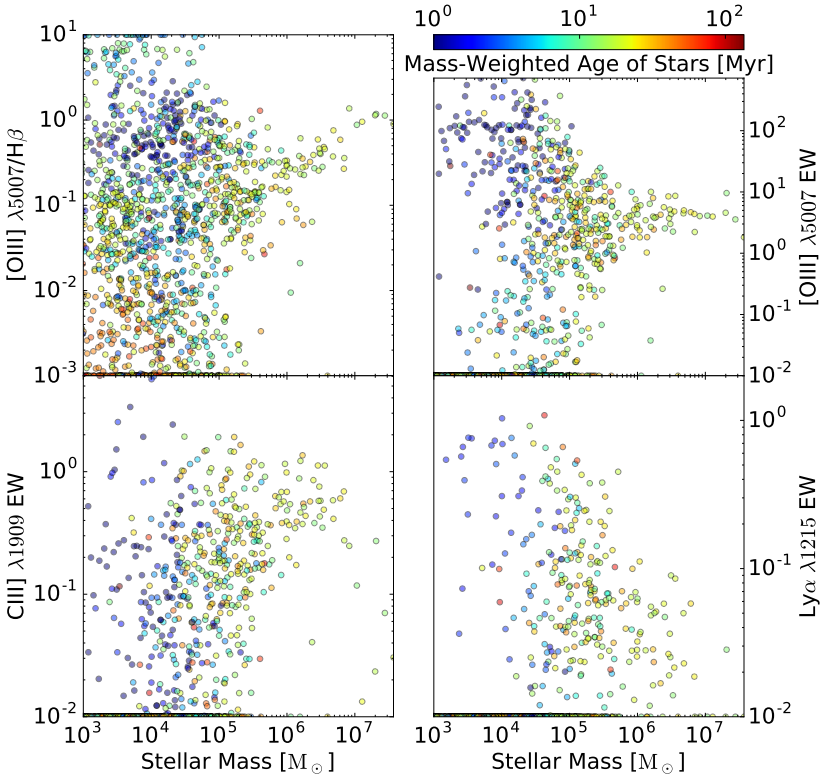

Figure 3.7: Emission line measures as a function of stellar mass. Upper left: [O III] λ5007 to Hβ ratio. Upper right: [O III] λ5007 equivalent width (EW). Bottom left: C III] λ1909. Bottom right: Lyα equivalent width. All emission line equivalent width and ratio plots are coloured by mass-weighted average age of the stellar population with definitions in the colour bar. Extreme values at low mass were plotted at the extreme of the plot window.

inhibiting star formation and shallower potential wells. This boundary appears on the plot as a $\sim 10^4$ range in luminosity inside this mass range. Higher halo masses are much more strongly correlated to luminosity, but our sample size diminishes at this end of our mass distribution. The relationship between luminosity and stellar mass is much more orderly and apparently linear, however luminosities still vary as much as a factor of 30 between 10^3 and 10^4 $M_\odot$. This is mainly due to variations in the composition and distribution of stars within each halo. Because haloes hosting small stellar populations are typically low mass, they are prone to photoevaporation and gas blowout[133] by supernovae which can occasionally leave stellar populations exposed, cutting off star formation. Galaxies with low stellar masses are therefore found to have a wide range of mean stellar ages consisting of either populations of bright, young stars or dim, older stars. At high stellar mass, the variability in luminosity is reduced to less than order of magnitude for a given stellar mass. In deeper potential wells, much of the remaining variability comes from the recent formation history of the galaxy. Systems with high merger rates or recent major mergers have disrupted gas distributions and bursts of star formation which may increase their luminosity with respect to stable, more isolated galaxies. These galaxies are also prone to stronger outflows due to the increased supernovae rate associated with higher star formation rates, but this is moderated by the deepness of their potential wells and the density of their gas.

The left panel of Figure 3.4 shows a colour-colour plot of our sample of galaxies coloured by mass-weighted mean stellar age. We observe a roughly linear relationship in magnitude space with a tendency for haloes with older stellar populations to inhabit a tail from $J_{150w} - J_{277w} < -1.0$ and $J_{200w} - J_{277w} < 0.4$. A well-correlated "ridge" forms in the figure as the age of the mean stellar population increases, moving the peak emission out of the UV and into less variable portions of the spectra. These haloes are usually the low to intermediate mass systems that have lost enough gas to extinguish

star formation. The redness of their spectrum can mostly be explained by an older stellar population dominated by stars with ages closer to 100 Myr. A line tracing the evolution of a single 1000 $M_\odot$, 0.01 $Z_\odot$ stellar cluster is shown to mostly follow the distribution with some notable exceptions redward of the line due both to the addition of emission lines and dust and gas attenuation. haloes with high stellar mass ($> 10^6$ $M_\odot$) are seen to congregate in the centre of the plot around $J_{150w} - J_{277w} = 0.5$ and $J_{200w} - J_{277w} = 0.4$ (right panel of Figure 3.4). Furthermore, the reddening of the galactic spectra is most apparent in larger galaxies with deeper potential wells and higher densities of gas and dust. When the processed colours are compared against the intrinsic FSPS composite, colours are seen to decrease by as much as 0.05 in $J_{200w} - J_{277w}$ and 0.5 in $J_{150w} - J_{277w}$.

3.3.1 Emission Line Strengths and Ratios

Figure 3.5 shows the JWST colour of each halo versus stellar mass. haloes with older stellar populations generally occupy the red portion of the plot (Low $J_{200w} - J_{277w}$) as expected. haloes with higher stellar mass tend to have $J_{200w} - J_{277w}$ values between 0.0 and -0.9 while intermediate and low stellar mass haloes appear to scatter without correlation between $J_{200w} - J_{277w}$ values of 0.7 and 0.2. While the range can be explained by the source spectra and stellar age, some of the variability comes from processing through gas and dust.

By changing the filtering of the full spectra, we are able to recalculate colours for different redshifts with the assumption that the mean stellar age is an approximate proxy for a comparable star formation history if we translate the star formation rates from higher redshift to lower redshift for the duration of the halo's assembly. However while we note that this is usually only valid for extraordinary cases, as an exercise, the effect of an uneven sampling of our galactic SED due solely to redshifting and mean stellar age is presented due to the significant impact it has on our

final colours. Figure 3.6 shows the mean values of the colour-colour diagram in Figure 3.4 evolved from $z = 8$ to $z = 15$ for four bins of stellar age in 30 Myr increments. As redshift increases, filters move towards the top left of the plot as filters begin to overlap with the Lyman break. Older stellar populations were found to exhibit higher $\mathrm{J_{200w} - J_{277w}}$ and $\mathrm{J_{150w} - J_{277w}}$ at all redshifts allowing the colour-colour plot to act as a tracer of both mean stellar age and redshift during reionization. When binned by log stellar mass, the data did not exhibit an observable difference in either colour at any individual redshift.

We provide plots of the equivalent widths of the [O III] λ5007, C III] λ1909 and Lyα lines for our entire sample in Figure 3.7. The relationship between halo stellar mass and equivalent width variance is seen to be generally inversely proportional to mass. Due to the extreme variance at low mass, we disregard un-observable equivalent widths below 0.01 Å. We expect that these data result from haloes with extraordinarily low metallicity or gas mass ratios such as haloes that have photo-evaporated or haloes without young stellar populations.

An initial burst of star formation in small haloes produce higher [O III] EW and [O III]/Hβ ratios as the halo is heated and ionized. Star formation is subsequently shut off since gas can no longer efficiently cool and supernovae expel most of the gas in the shallower haloes. haloes that are photo-evaporated by their proximity to larger galaxies, or are otherwise isolated from gas inflows, or have their star formation inhibited have progressively older stellar populations and drift downward in both [O III] plots. haloes that accrete enough cool gas to resume star formation until their haloes are again heated and ionized, restarting the cycle. haloes that continue to grow in this manner trace a "zig-zag" path as their stellar masses increase. Above a stellar mass of around 10^5 $\mathrm{M_\odot}$, haloes are typically large enough that star formation events create confined H II regions and a single halo can consist of multiple regions of high and low formation rates. These haloes have lower variability in the [O III] EW

Table 3.1: Linear regression analysis between flux ($z = 15$) and stellar mass.

Filter	β_1	$SE_{\beta,1}$	β_0	R^2
f125w	3.0326	0.1595	-44.8256	0.1802
f140w	1.4737	0.0270	-29.8067	0.6443
f160w	1.4154	0.0245	-29.2539	0.6705
f115w	1.2554	0.0299	-32.4697	0.5169
f150w	1.4243	0.0249	-29.3746	0.6657
f200w	1.2606	0.0168	-28.1623	0.7730
f277w	1.2165	0.0145	-28.0872	0.8110
Bolometric	1.1984	0.0137	34.8578	0.8233

Notes: Correlations are given between log flux (in units of $\mathrm{erg/s/cm^2}$) and log stellar mass for Hubble (top) and JWST (middle) IR filters at $z = 15$ as well as the bolometric luminosity (in units of erg/s). The columns show filter, slope, the standard error of the slope, zero-point, and R^2, respectively. The functional form is assumed to be $\log f = fi_0 + fi_1 \log M_\star$.

and [O III]/Hβ ratio plots as younger and older stellar populations are averaged.

In galaxies with $M_\star \leq 10^{4.5}$ $M_\odot$, the highest C III] EWs are correlated to young stellar populations but are still only 1–3 Å. Above that mass, larger C III] EWs are associated with intermediate age populations and galaxies with a stellar masses more than $\sim 3 \times 10^5 M_\odot$. This behaviour is not dissimilar to the distribution of [O III] EW with respect to stellar mass and age, but exhibits more variability at high mass.

We show intrinsic rather than emergent Lyα equivalent widths, which would require the implementation of a dedicated Lyα radiative transfer code. We find that intrinsic Lyα equivalent widths are generally insubstantial and the maximum Lyα EW further decreases with increasing $M_\star$ from $\sim$ 1Å for $M_\star \leq 10^5$ down to less than 0.1Å for $M_\star \geq 10^7$ due to the lower neutral hydrogen fractions in bright galaxies.

3.3.1 Composite Spectra

Table 3.1 shows the slope of the magnitudes in various HST and JWST filters as a function of stellar mass for objects observed at $z = 15$. HST filter f125w and JWST filter f115w examine wavelengths that lie partially beyond the Lyman break in the

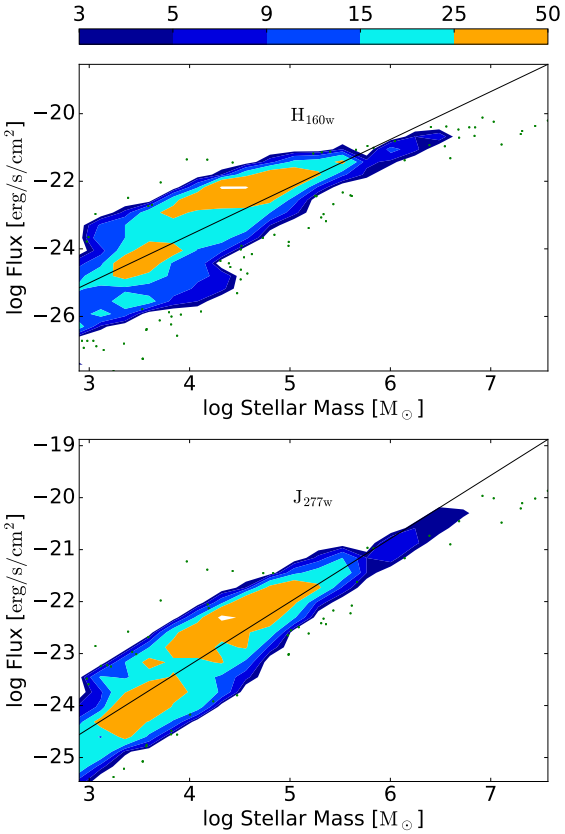

Figure 3.8: Contour histograms and scatter plots corresponding to the Hubble f160w (top) and JWST f277w (bottom) filters. While the regressions are appropriate at lower stellar masses, they tend to overestimate flux for log $M_\star > 6$.

Table 3.2: Linear regression analysis between apparent magnitude ($z = 15$) and stellar mass.

Filter	β_1	$SE_{\beta,1}$	β_0	R^2
J	-7.3825	0.4905	90.8858	0.1211
H	-3.4369	0.0563	49.5863	0.6938
K	-3.0903	0.0389	46.7610	0.7931

Notes: Correlations are given for various filters, redshifting the spectra to $z = 15$. The columns show filter, slope, the standard error of the slope, zero-point, and R^2, respectively. The functional form is assumed to be $m_x = \beta_0 + \beta_1 \log M_\star$.

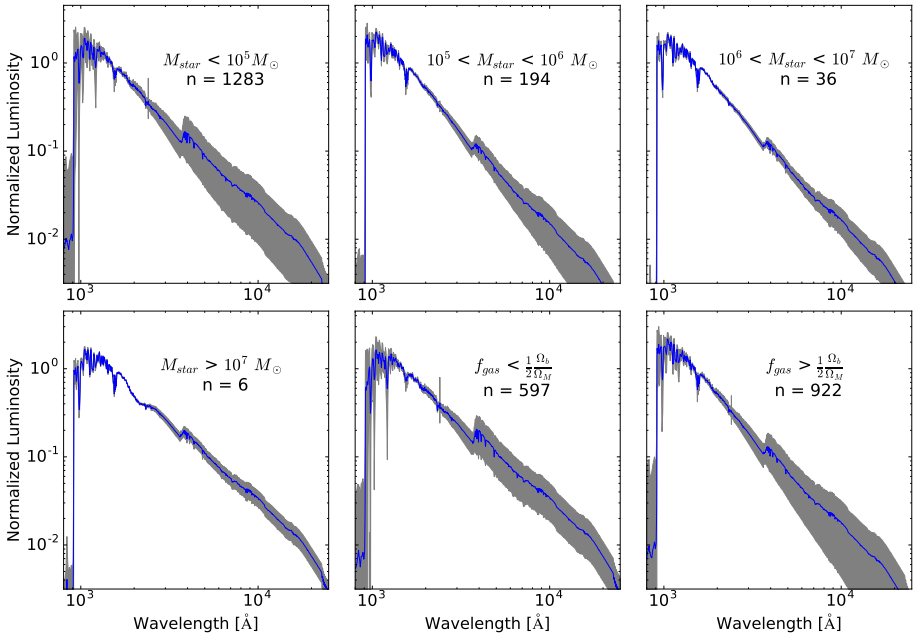

Figure 3.9: Stacked galactic spectra with mean values in blue and 1σ bands in grey in different stellar mass range (top row and bottom right) and gas-poor (bottom middle) and gas-rich (bottom right) haloes. Luminosities are normalized to the mean value at 1500 Å(rest), and the overall luminosities can be inferred from Figure 3.3.

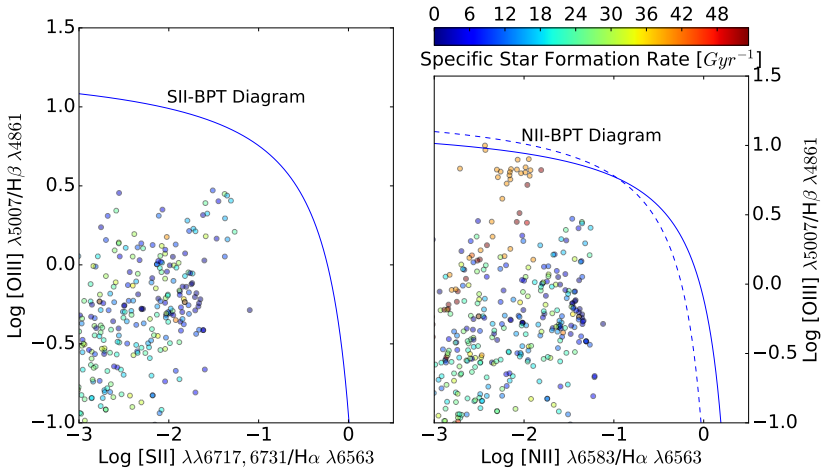

Figure 3.10: S II and N II BPT diagrams of the emission line ratios coloured by specific star formation rate. The AGN line in the work by Kauffmann et al. [134] is shown as a solid line and the work by Kewley et al. [135] is shown as a dashed line with AGN occupying the region above and to the right of the lines.

rest frame and exhibit low correlation. For the other filters, linear regression analysis demonstrates R^2 varies between 0.64 and 0.77 in each filter, implying relatively large variation of individual halo luminosity when summed over the frequency space corresponding to an individual spectra. The locus of points used to generate the regression of the bolometric luminosity are presented in the bottom panel of Figure 3.3. Figure 3.8 shows corresponding countor histograms for HST filter f160w and JWST filter f277w which have the highest infrared mean wavelengths and are thus the most useful filters in either telescope for studying linear trends in this epoch. While linear fits seem to be appropriate for haloes with lower stellar masses, we see a tendency for the fits to overestimate the mean flux and luminosity of our spectra for $M_\star > 10^6\ M_\odot$. When narrower bands corresponding to the Vega colour designations are used, the R^2 values are generally higher as shown in Table 3.2 for measures of absolute magnitude at $z = 15$. This can be somewhat explained by the variation in emission lines demonstrated in part by Figure 3.7 and the tendency for larger bands to include more lines and thus more variability. Additionally, J, H and K filters demonstrate a higher tendency towards a linear relationship with higher wavelength. The slope of absolute magnitude with respect to solar mass generally becomes more gradual (less negative) with wavelength.

Figure 3.9 shows composite spectra for four ranges of stellar mass as well as gas mass fractions below and above half the mean baryon fraction (Ω_b/Ω_M). Each plot shows the mean and standard deviation of the spectra among the stated sample with each composite spectra normalized to 1500 Å(rest), where the overall normalization can be inferred from the luminosities in Figure 3.3. Like the distribution of emission line strengths, the spread of the spectra appears to be inversely related to the mass of the halo. This may be partially explained by the sampling bias due to small numbers of star particles in small haloes. For larger halos ($M_\star = 10^6 - 10^7\ M_\odot$) with several hundred or more stellar particles, the wider standard deviation may be related to

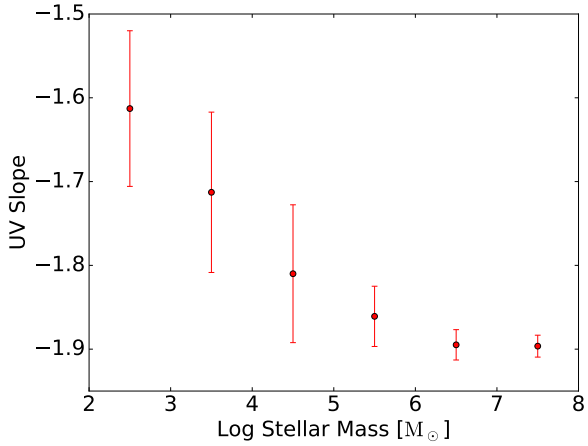

Figure 3.11: The UV slope of averaged spectra versus stellar mass, showing the galaxies becoming bluer with increasing stellar mass up to 10^6 $\mathbf{M}_\odot$. This steepening of the UV slope occurs because all galaxies above this mass range host active star formation, whereas only a fraction of less massive galaxies host active star formation.

greater variability in the metallicity and temperature of the CSM about each halo and less variability in the centre of the clusters containing the largest halos.

Figure 3.10 shows the Baldwin, Phillips and Terlevich[BPT; 136] diagrams of both ([O III] λ5007)/Hβ to (S II $\lambda\lambda$6717,6731)/Hα and ([O III] λ5007)/Hβ to (N II λ6583)/Hα. BPT diagrams are customarily used to delineate the boundary between normal star-forming galaxies and active galactic nuclei. In our data, all points lie below the AGN boundary for S II[134] and the AGN boundary for N II[135]. Though some objects graze the boundary in the N II diagram, there is some evidence that this is a feature of star-formation dominated spectra for high-redshift objects[137].

The average spectral slope in the range 1200–2500 Å(rest) is plotted in Figure 3.11 assuming flux follows a power law relationship with respect to wavelength ($f_\lambda \propto \lambda^\beta$). UV slopes are calculated using a linear regression on the full SEDs for the indicated mass bins between 1200 and 2500 Å(rest). As discussed, bins of low stellar mass can include populations of halos with relatively old and red stellar populations whereas bins of higher stellar mass include a large distribution of young and older stellar

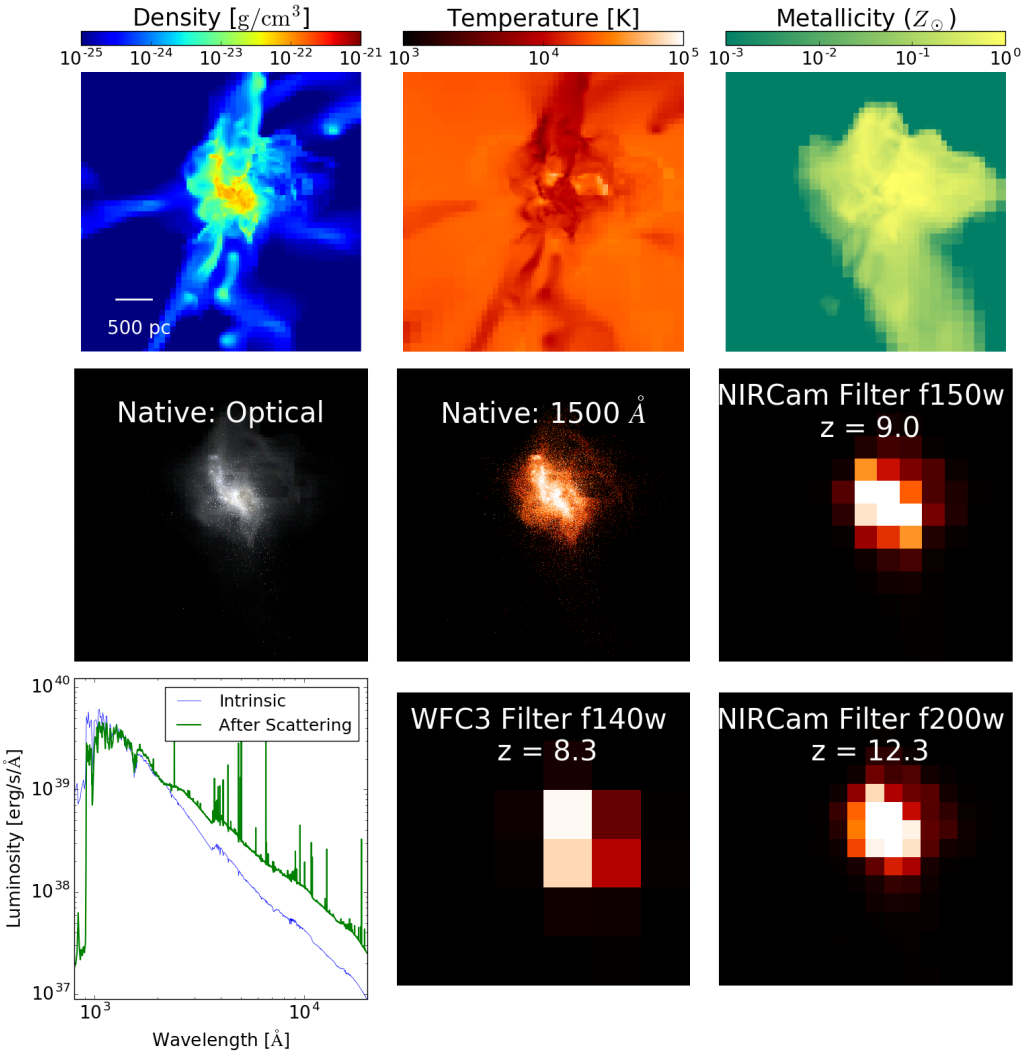

Figure 3.12: Synthetic imaging and spectrum of Halo A ($M_{\rm tot} = 1.05 \times 10^9$ M$_\odot$, $M_\star = 2.04 \times 10^7$ M$_\odot$). Top Row: Density-weighted projections of density, temperature, and metallicity. Middle Row: composite of optical frequency images, a monochromatic image of the halo at 1500 Å and the same image as seen through the JWST NIRCam F150W filter (1.5 μm). Bottom Row: intrinsic stellar spectrum (thin blue line) and processed galactic spectrum with dust and gas absorption, re-emission, and emission lines (thick green line), the 1500 Å image as seen through Hubble's WFC3 F140 filter (1.4 μm) and JWST NIRCam F200W filter (2.0 μm) with the latter having a lensing magnification factor $\mu = 10$.

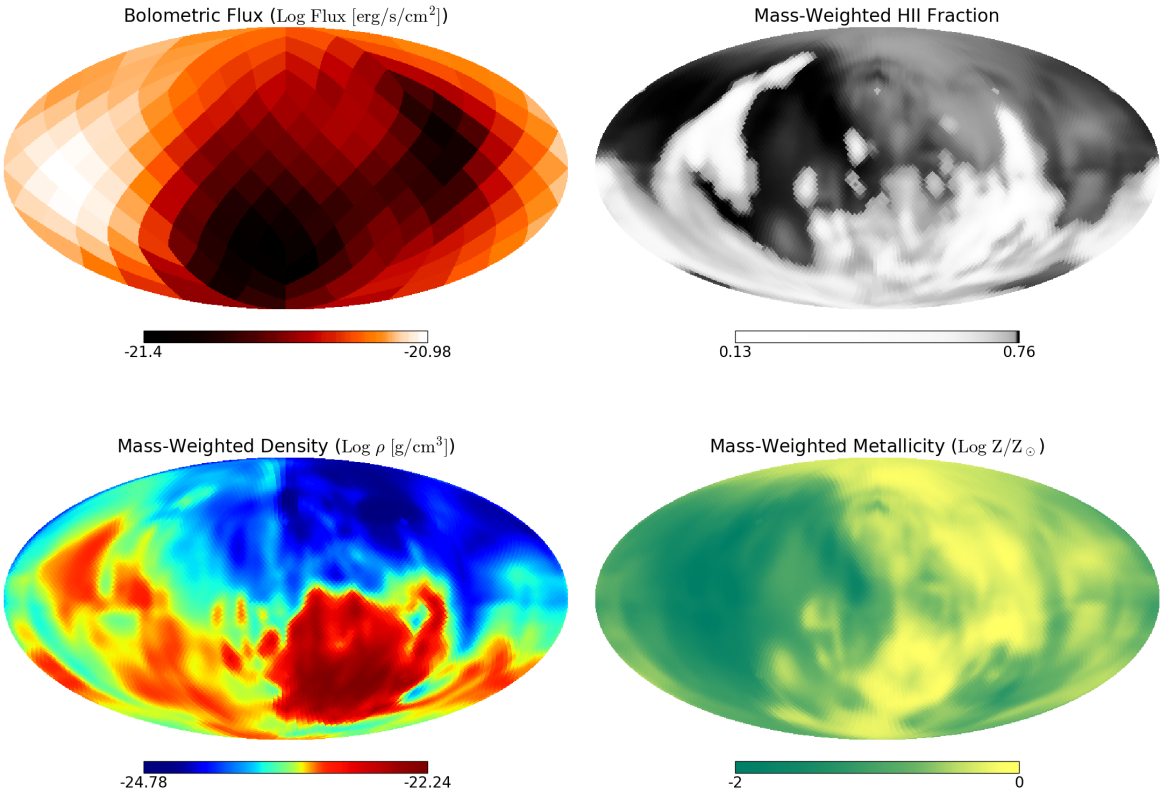

Figure 3.13: Variations of emergent flux and gas properties of Halo A along different lines of sight. Top row: Ecliptic view of total flux for Halo A at $z = 15$ (left) and the mass-averaged H II fraction (right). Bottom row: Mass-averaged density and metallicity along the same normals integrated to the virial radius of Halo A.

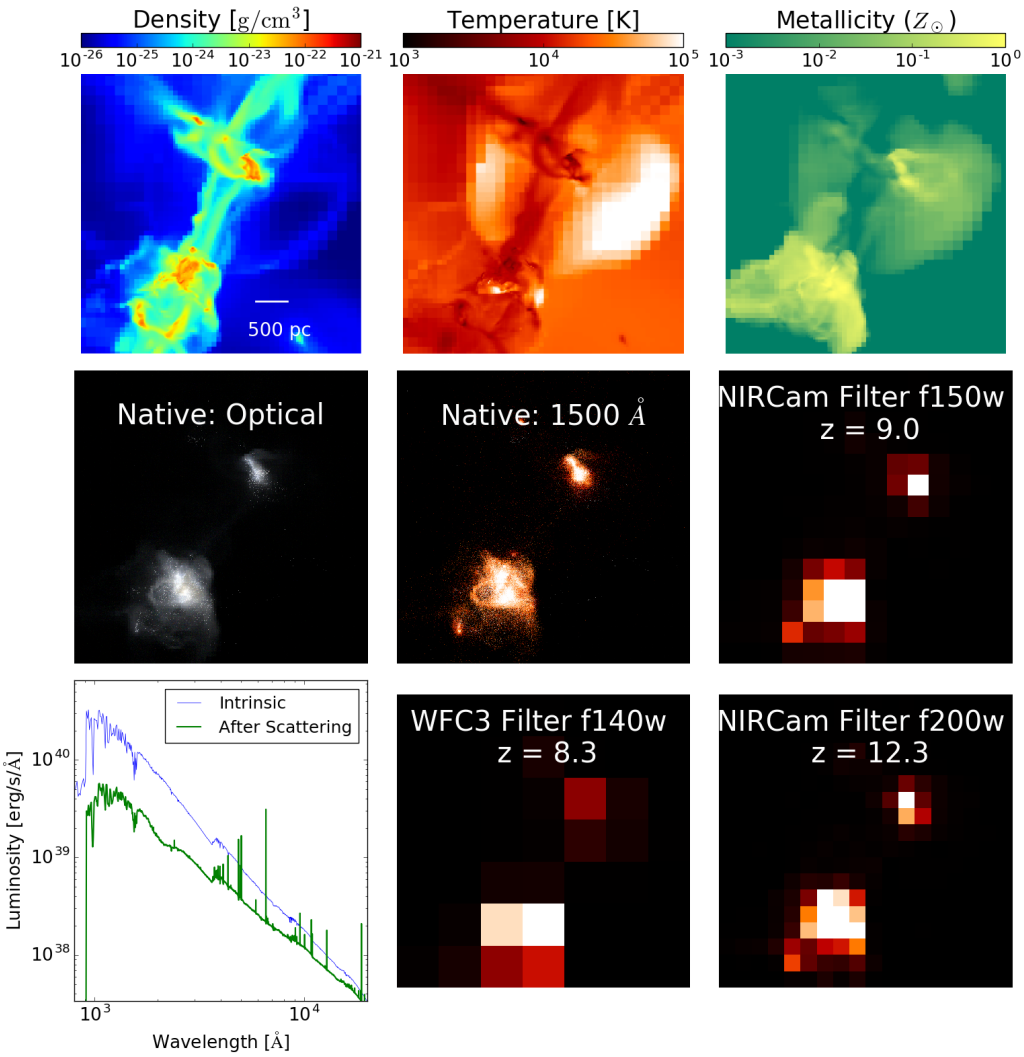

Figure 3.14: Halo B ($M_{\rm tot}$ = 1.62 × 10^9 $M_\odot$, $M_\star$ = 3.4 × 10^7 $M_\odot$) plotted in the same manner as Halo A in Figure 3.12.

Table 3.3: Individual halo properties

Halo	$\log M_{\rm tot}$ $[M_\odot]$	$\log M_\star$ $[M_\odot]$	$f_{\rm gas}$	$Z_\star$ $[Z_\odot]$	$\log L_{\rm tot}$ [erg s^{-1}]
A	9.02	7.31	0.164	0.410	42.88
B	9.21	7.57	0.133	0.440	43.03

Notes: The columns show halo mass, stellar mass, gas mass fraction, mass-averaged stellar metallicity, and total bolometric luminosity.

populations, resulting in a fairly consistent mean stellar age for our entire sample of large galaxies. Thus, halos with stellar masses between 10^7 and 10^8 $M_\odot$ ($n = 5$) have relatively low variability and average UV slopes of around $\beta = -1.85$. The intrinsic FSPS galactic spectra for the same sample is between $\beta = -1.85$ and –1.90 implying that our method resulted in a slightly shallower slope for our largest objects. Other mass bins show little to no change in the UV slope after applying our pipeline.

3.3.2 Individual Halos

We present two cases from the Renaissance Simulations to demonstrate the impact and utility of our dust scattering and emission line method. Relevant statistics for the halos discussed are provided in Table 3.3.

Halo A (Figure 3.12) is the third most massive halo in our simulation with a total mass of 1.05×10^9 $M_\odot$ and a stellar mass of 2.04×10^7 $M_\odot$. We see from the density projection (top left panel) that the halo is centred on a single large galaxy surrounded by several satellite galaxies and sub-halos. Halo A has a mass-weighted mean metallicity of 0.242 $Z_\odot$, which corresponds to the presence of enough dust to attenuate the galactic spectra. Defining the circum-stellar medium (CSM) as the medium within the virial radius of a halo that exists about but not necessarily between the halo's stellar population, we observe that the metallicity distribution (top right) is uneven with large volumes of the CSM un-enriched. The optical composite (middle left) shows stellar populations mostly concentrated in the main galaxy within regions of high gas density. We also see a smaller diffuse population of star particles towards

the bottom of the image that have been stripped from the main body of the halo into a region of relatively low gas density. In the SED (bottom left), higher gas densities contribute to a significant degree of frequency-dependent scattering and reprocessing of the intrinsic stellar spectra towards lower frequencies. Due to diffuse emission[cf. 138], the bolometric luminosity of the galaxy after processing through our pipeline exceeds the intrinsic luminosity due solely to stellar sources by 0.64 mag (80% brighter). We also observe that Halo A would be discernible above the noise at $z = 8.3$ using WFC3 and would exhibit some structure through NIRCam at $z = 12$ assuming gravitational lensing by a factor of $\mu = 10$.

Hyperion allows for the calculation of the flux incident onto a plane of arbitrary orientation. By using HEALPix to generate equally spaced normals about a sphere, we generate a composite image of flux from a single galaxy as a function of the observer's viewing angle. Line integration of physical quantities along those normals from the centre of the halo to its virial radius produces corresponding plots of density and metallicity for comparison.

Figure 3.13 shows the integrated flux, H II fraction, mean density, and metallicity as a function of viewing angle about Halo A normalized at $z = 10$ without IGM absorption. Depending on the viewing angle, the total integrated flux at the observer from Halo A varies by a factor of ~ 3 emphasizing the anisotropic nature of modelling ISM and CSM attenuation and scattering despite a relatively central arrangement of stars and gas. Furthermore, line integrals of mass-weighted mean density through the centre of the halo vary by more than two orders of magnitude depending on the normal direction. Normals along high mean density correspond to lower bolometric flux, but normals along lower mean densities do not result in the highest flux at the observer. Since this halo exhibits heavy scattering and a 0.64 magnitude increase in bolometric luminosity due to diffuse emission, the brightest flux corresponds to regions of intermediate density where enough gas is present to contribute to emission, but

not enough to exhibit self-shielding. Mass-weighted metallicity shows a slightly more complicated relationship as some regions of both high and low densities are metal-enriched and the most metal poor directions have intermediate-gas densities. The brightest normals appear to be therefore correlated to the lowest gas metallicities implying a lack of prior star formation in those regions. The plot of H II fraction confirms the presence of confined H II regions that are observed in Figure 3.12 as the hottest pockets of gas in the temperature projection plot. These H II regions appear to be powering diffuse emission and the greater flux. Taken together, confined H II regions around young stars in intermediate-density metal-poor gas are producing diffuse emission that result in a significantly brighter flux at the observer than could be explained with intrinsic stellar spectra, but with great variability with respect to viewing angle.

A system of merging galaxies within Halo B is shown in Figure 3.14. This halo is notable for its high mass-weighted mean stellar metallicity of 0.440 $Z_\odot$ and contains the largest total mass of any halo in our simulation (1.62×10^9 $M_\odot$). Like Halo A, Halo B is plainly visible through HST and JWST assuming a gravitational lensing by a factor of $\mu = 10$. It appears as two distinct visible galaxies connected by a faint filament of stellar clusters. The larger galaxy in the lower portion of the projections is metal-enriched, showing near Solar metallicity in the brightest regions and metallicities above 10^{-1} $Z_\odot$ in its CSM. The smaller galaxy is also metal-enriched but the adjacent filamentary structures are notably metal poor despite the presence of stars. This implies that the stars and structure of the filament are relatively young.

The hottest regions of the temperature projection ($T \geq 10^5$ K) trace multiple supernova remnants centred in a region of disrupted gas that includes the smaller galaxy. This further implies that the halo has been disrupted into its current configuration from a set of two more cohesive merging galaxies with established metal-enriched stellar populations. Temperature projections also indicate the presence of H II regions

in the larger galaxy, which also appear as diffuse radiation in the 1500 Å(rest) image. The intrinsic bolometric luminosity of the stellar sources peak at approximately 3×10^{40} erg s^{-1} Å^{-1} at 935 Å(rest), but is attenuated by the gas and dust to a peak of around 6×10^{39} erg s^{-1} Å^{-1} at 1050 Å(rest) with roughly similar attenuation for all frequencies simulated.

3.4 Discussion

Due to the anisotropic nature of dust and gas scattering and absorption, a fully three dimensional model is required for representative modelling of the spectral energy distribution of a galaxy. Furthermore, the effect of viewing angle is shown to produce large variation in flux at the observer in even in relatively well-ordered systems. This may therefore result in large uncertainties when interpreting observations of the first galaxies, however most of the overall variability in the results is confined to halos with total masses below 10^8 $M_\odot$. Above this mass, results converge in colour-colour diagrams, equivalent and line ratio plots, and plots of composite spectra.

Some of this convergence may be explained by the similarly ionized cosmological environment about large halos with relative high star formation rates and some of it may be explained by deeper gravity wells acting against the tendency for halos to become gas-poor through photo-evaporation or gas blowout. Conversely, the divergence at low mass can be explained by bursts of star formation and diversity in the H II regions around galaxies.

Our picture of radiation through galaxies in the EoR is incomplete however. Our method calculates the photoionization in the H II regions around clusters by assuming the cluster radiates as a single source. Because the simulation forms clusters that have a minimum mass of 1000 $M_\odot$, the nature of the ISM between stars within a cluster is not simulated directly by our model. Furthermore, we do not apply the Monte-Carlo process directly to the scattering and attenuation of emission lines so we do not

capture the effect of an uneven medium at larger scales either.

The size of our stellar cluster particles implies the assumption that stars do not diffuse through a galaxy during the course of our simulation. This has the effect of both over-estimating the flux of photons around clusters and underestimating the flux throughout the rest of the ISM for older clusters. This may also have an impact on the star formation rate and the distribution of supernovae. We also do not include the spectra or luminosity of Population III stars or accreting black holes in the model at this time so we cannot speak to their contribution to the photometry and spectra of early galaxies.

Since our spectra are simulated for a closed volume about a halo, we do not capture the effect of the outer circum-galactic medium or the intergalactic medium (IGM). While we do account for cosmological effects, several intermediate and foreground effects may cause observations of galaxies simulated by this work to differ materially from observed galaxies that are otherwise similar in nature. We encourage the use of an appropriate model for the IGM in comparisons. For example, one could use the galaxy spectrum as the background of a ray-trace through the IGM, as used by Trident[139]. This will include all important effects on the spectrum outside of the virial radius, including absorption from H I and metal species as well as galaxy foreground effects.

3.4.1 Comparable Works

3.4.1 Zackrisson et al. (2013)

Using stellar SEDs from the Yggdrasil population synthesis code[60] and Cloudy, Zackrisson et al. [140] explore the evolution of the UV slope of galaxies over time and with respect to Hβ EW for a range Lyman continuum escape fractions. They argue that for high escape fractions, galaxies with $M_\star \geq 10^7$ M$_\odot$ should be detectable with JWST up to $z \simeq 9$ where our entire sample of galaxies with $M_\star \geq 10^7$ M$_\odot$ is

visible to redshift 12 with $\mu = 10$. They note that the contribution of dust is harder to determine and suggest the use of ALMA to constrain the IR dust emission peak of observations.

3.4.1 Cen and Kim (2014)

Cen and Kimm [141] use ENZO to calculate a zoom-in region about a 3×10^{14} $M_{\odot}$ halo. They produce stellar SEDs with GISSEL[57] and use the code SUNRISE[142, 143] to model dust absorption and scattering. Emission lines are added to the spectra of young star clusters using the code MAPPINGSIII[143] by assuming a constant star formation rate for 10 Myr. To motivate upcoming observations by ALMA, they explored peak IR wavelengths, luminosity functions, and FUV-NUV colors and found their results to be in good agreement with observations. This work concurs with their result showing markers of bursty star formation in low mass halos.

3.4.1 Wilkins et al. (2016)

Using the GADGET Bluetides Simulation[6], Wilkins et al. [144] applied CLOUDY to generate emission lines lines for EoR galaxies. They compared the effect of different stellar population synthesis models on the UV slope and found a ~ 0.2 variation in β. They predict somewhat steeper UV slopes (-2.4 to -2.5 for FSPS) in their sample using $\beta = 1.8 \times (m_{\mathrm{fuv}} - m_{\mathrm{nuv}}) - 2.0$ and FUV and NUV magnitudes whereas our study directly calculates UV slopes using a regression (Figure 3.11). Their study of the effect on redshift also finds that galaxies became more blue at higher redshift corresponding to younger stellar populations. Our work concurs with redder colours in the higher mean stellar age bins, but is confined to a single redshift and therefore does not track the evolution of the distribution of colours as galaxies age.

3.4.1 Cullen et al. 2017

A recent submission by Cullen et al. [145] explores the effect of dust on galaxies in the GADGET First Billion Years Project[7]. Stellar population synthesis is calculated using BPASSV2[146] and emission lines are calculated using CLOUDY. In contrast to this work and the work of Cen and Kimm [141], dust attenuation is accomplished by comparing a suite of different analytic models rather than a Monte Carlo process. One of their most consistent dust attenuation laws is reported as $A_{1600} = 2.10^{1.9}_{-0.3}(\beta + 2.52)$ at $z = 5$ where β is the UV slope. They note that this implies a higher star formation rate than previously deduced and appeal to ALMA for confirmation.

3.4.2 Applications

Our data set includes synthetic observations that would be visible with current telescopes, but the vast majority of our mock observations are too far and too dim for the current generation of hardware. This work therefore extends our measures and figures to regimes that await validation by JWST and other future telescopes. Furthermore, our sample is large enough for some measures to be compared to a statistically significant body of observed EoR galaxies and therefore serves as a prediction of trends and distributions of colour-colour plots, luminosity, and emission lines. We also see utility in the use of our investigation as a means for the preliminary categorization and characterization of future observations.

3.4.3 Future Enhancements

The JWST team is developing an image processing calculator[1] that processes raw source photometric data into synthetic JWST results. The potential exists to integrate the source code into this pipeline to refine the analysis and ensure better confluence with observational data beyond the methods explored thus far.

[1] https://demo-jwst.etc.stsci.edu/

Emission line calculations are currently limited to an augmented luminosity calculation that needs to be further refined and calibrated. A method that directly simulated the scattering of the emission lines throughout the ISM is preferred.

The current method neglects the inclusion of Population III stellar spectra in its first iteration due to the exclusion of this type of star from the isochrones available in FSPS. Theoretical source spectra are available in YGGDRASIL and will be integrated into the second iteration. Additionally, by including composite spectra models of accretion disks and the region around black holes, the potential exists to extend this method to simulations of galactic nuclei and starbursts about black holes.

Additionally, with the development of synthetic photometry and spectra pipelines, tracking the evolution of the flux and spectra over time presents a novel line of investigation and a natural extension of the work completed to this point. With few extensions, all the results presented in the previous section may be converted into a time-series analysis by connecting data from each simulation data output.

3.5 Conclusions

With deep field observations using the Hubble Frontier Fields and the forthcoming JWST enabling the collection of a statistically significant sample of galaxies at high redshift, cosmological simulations of the Epoch of Reionization offer an opportunity to make predictions. We employ results from the "rare peak" zoom-in region of the Renaissance Simulations to stage a Monte Carlo photon simulation of continuum radiation through dust and gas as well as calculations of nebular emission lines. We generate synthetic photometry and spectra for two of our largest individual galaxies and provide photometric measures of the entire aggregate sample. Our study of the larger individual galaxies reveals the following insights:

1. Dust and gas attenuation is non-isotropic and wavelength-dependent for some halos. Our first example shows that flux versus inclination is not necessarily

a function of column density for irregular galaxies. The distribution of H II regions and the age of bursts of star formation may result in viewing angles where a galaxy may appear several times brighter.

2. The intrinsic spectra produced by a stellar population synthesis model may understate the final luminosity of a galaxy after the calculation of gas and dust scattering in addition to the effect of H II regions in some situations.

Our study of the entire sample of star-containing halos reveals the following trends:

1. Halos with the lowest total mass have the highest variability in bolometric luminosity (4 orders of magnitude). Likewise, halos with the lowest stellar mass have the greatest variability in [O III]/Hβ, [O III] EW and C III] EW. This is due to cycles of star formation feedback having a significant impact on the gas in the smallest halos. Lyα equivalent widths are less than 1Å and exhibit an inverse relationship with $M_\star$ and electron fraction.

2. The slope of luminosity versus stellar mass becomes shallower and more linear with the mean wavelength of a filter band. Variations in the spectra between halos are least between the highest stellar mass halos and greatest between our lowest stellar mas halos.

3. Our method causes a small decrease in $\mathrm{J_{200w} - J_{277w}}$ colour and a up to a ~ 0.5 decrease in $\mathrm{J_{150w} - J_{277w}}$ colour versus the intrinsic FSPS stellar spectra for larger-mass halos.

4. UV slopes decrease as stellar mass increases for halo with stellar masses between 10^3 to 10^8 $\mathrm{M_\odot}$. Our method results in shallower UV slopes than the intrinsic stellar population synthesis spectra for the highest mass objects.

We have shown the impact of anisotropic, non-homogeneous dust and gas distributions on mock photometry and predictions for galactic spectra. Our treatment

illustrates a method for the characterization of future observations of the early Universe and provides a large sample of mock observations that demonstrate physically-motivated trends in emission lines, colours, and luminosity from a large, representative cosmological simulation.

CHAPTER 4
EMISSION LINES, POPULATION III STARS, AND X-RAY BINARIES

This chapter describes improvements to the methodology and implementation of the synthetic observation modeling pipeline to Population III galaxies in the same cosmological simulation. Hereafter is the work as published in the Monthly Notices of the Royal Astronomical Society in February 2018 with John Wise, Aycin Aykutalp, Brian O'Shea, Michael Norman, and Hao Xu as coauthors.

We produce synthetic spectra and observations for metal-free stellar populations and high mass X-ray binaries in the Renaissance Simulations at a redshift of 15. We extend our methodology from the first paper in the series by modelling the production and extinction of emission lines throughout a dusty and metal-enriched interstellar and circum-galactic media extracted from the simulation, using a Monte Carlo calculation. To capture the impact of high-energy photons, we include all frequencies from hard X-ray to far infrared with enough frequency resolution to discern line emission and absorption profiles. The most common lines in our sample in order of their rate of occurrence are Lyα, the C IV $\lambda\lambda 1548, 1551$ doublet, H-α, and the Ca II $\lambda\lambda\lambda 8498, 8542, 8662$ triplet. The best scenario for a direct observation of a metal-free stellar population is a merger between two Population III galaxies. In mergers between metal-enriched and metal-free stellar populations, some characteristics may be inferred indirectly. Single Population III galaxies are too dim to be observed photometrically at $z = 15$. Lyα emission is discernible by *JWST* as an increase in $\mathrm{J_{200w}} - \mathrm{J_{277w}}$ colour off the intrinsic stellar tracks. Observations of metal-free stars will be difficult, though not impossible, with the next generation of space telescopes.

4.1 Introduction and Background

The advent of large and high-resolution cosmological simulations such as the Renaissance Simulations[2, 112] provide an opportunity to glean observables from theoretical and numerically-deduced phenomena. However because radiative transfer is computationally expensive inside a full simulation, post-processing is usually required to better extrapolate the fine features of the spectral energy distribution related emission lines and dust extinction.

Therefore the contemporary frontier of synthetic spectrometry and photometry lies in the sophistication and physical accuracy of post-processing techniques. As the second paper in the series chronicling the methodological development of the Caius pipeline, this work seeks to invest more computational power in the modelling of absorption, scattering, and emission of photons and explores the impact of high-energy photons from sources unique to the early universe.

4.1.1 Population III stars and X-ray Binaries

Prior to the formation of the first generation of stars, the primordial medium was essentially metal-free. The lack of metal cooling theoretically increases the Jeans mass of molecular cloud and allows for the possibility for the formation of more massive stars than the observed initial mass function (IMF) of stars in the local universe. However the primordial IMF is limited at the upper range by the effect of radiation pressure, the nature of the protostar, the effective sound speed, and the propensity of the medium to clump[see reviews by 147, 148]. These early "Population III" stars were luminous and hot for their masses and thus contributed to the ionization and heating of the surrounding medium.

Massive Population III stars are likely to end in neutron stars and black holes after a short mass-dependent lifespan[120]. When part of binary systems, compact

remnants may thereupon accrete material from a longer-lived stellar partner, converting potential energy into high-energy photons in their accretion disks. In this scenario, termed an X-ray binary, the flux of X-rays and UV photons ionize metals in the interstellar medium (ISM) to multiply-ionized states like C IV. Indeed, C IV lines have been confirmed in the spectrum of analogous low-redshift systems of low mass ($M_\star < Mbh$) X-ray binaries[e.g. 149], and high mass X-ray binaries[HMXB; e.g. 150].

4.1.2 Emission Lines

While there has been progress on the modelling of emission lines and dust[140, 141, 144, 151], the work of solving photoionization is usually left to routines or analysis run on isolated scenarios rather than within a cosmological context. This work endeavours to simulate photochemistry as part of an extinction and emission routine that appreciates a fully three-dimensional arrangement of dust, gas, and stars. In Sec. 4.2, we propose a methodology for generating and propagating the intrinsic spectrum of metal-enriched stars, metal-free Population III stars, and HMXBs through gas and dust to produce resultant galactic continuum and emission lines. In Sec. 4.3, diagnostics of observables from our treatment are presented including emission line strengths and photometry for the forthcoming James Webb Space Telescope (JWST). Finally, the observational and physical implications of our results are discussed in Sec. 4.4 and summarized in Sec. 4.5.

4.2 Methods

We use the "rare-peak" zoom-in region of the Renaissance Simulations[2, 112], which are performed using the hydrodynamic adaptive-mesh refinement (AMR) code ENZO with radiative transfer[77] and focus on the first generations of stars and galaxies early in the Epoch of Reionization. The simulations are run using $\Omega_M = 0.266$,

$\Omega_\Lambda = 0.734$, $\Omega_b = 0.0449$, $h = 0.71$, $\sigma_8 = 0.8344$, and $n = 0.9624$ from the 7-year *Wilkinson Microwave Anisotropy Probe* results[WMAP; 115], achieving an effective dark matter resolution of $2.9{\times}10^4$ $M_\odot$ at $z = 15$ and a spatial resolution of 19 comoving parsecs. We identified 1654 galaxies containing stellar clusters within the "rare-peak" simulation at $z = 15$ using dark matter halo-finding code ROCKSTAR[126]. Of these galaxies, we focus our analysis on 146 that contain metal-free stellar populations.

4.2.1 Stellar Spectra

We use the Flexible Stellar Population Synthesis code[FSPS; 59] to generate source spectra of metal-enriched stellar clusters from the age and metallicities of particles in the simulation. Both FSPS and the simulation routines treat stellar clusters as probabilistic distributions of stars and treat luminosity as a linear function of mass. We exploit this similarity to assign spectral energy distributions (SEDs) to stellar cluster particles for radiative transfer post-processing in a manner consistent with the assumptions used to produce those particles. Using quantities calculated in the simulation, we assign each particle a metallicity isochrome and allow FSPS to interpolate an SED based on the particle's age before weighting our result by the mass of the cluster.

For metal-free stars, we the Renaissance Simulations generate stellar particles corresponding to individual stars rather than clusters in the simulation by randomly sampling the distribution given by Equation 3.1 when the appropriate environmental conditions are achieved[151]. This form obeys the Salpeter [152] distribution above a characteristic mass, M_c, and has an exponential cut off at low mass[119, 153]. We limit Population III star particle mass to the range 1 $M_\odot$ to 300 $M_\odot$ and use $x = 1.3$, $\beta = 1.6$, and $M_c = 40$ $M_\odot$. Generally, the peak of the distribution is given by

$$M_{\text{peak}} = M_c \left(\frac{\beta}{x}\right)^{1/\beta}, \tag{4.1}$$

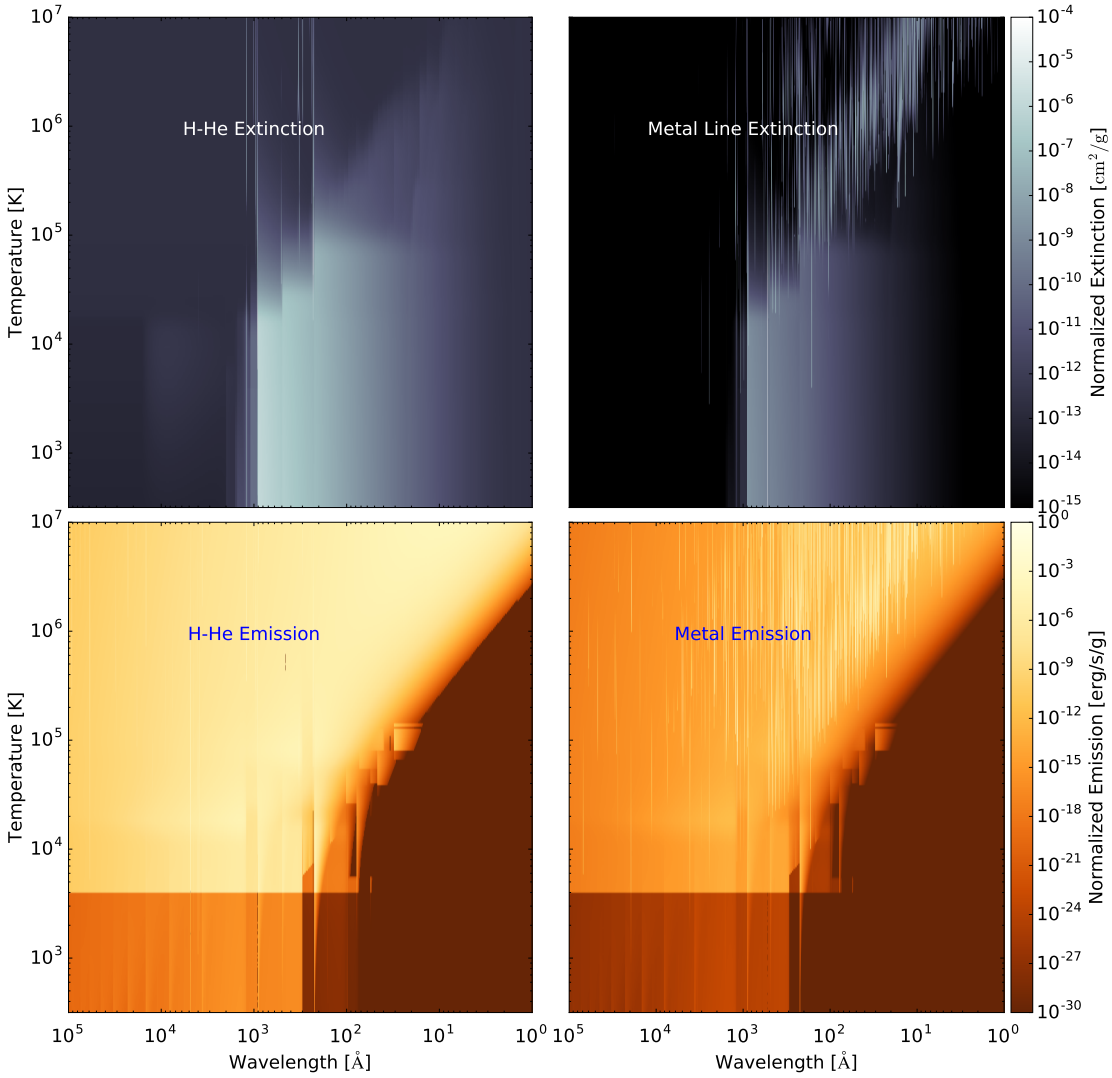

Figure 4.1: Top Row: Total extinction profiles for gas and metal emission lines and a gas absorption continuum as a function of wavelength and temperature. Bottom Row: Corresponding emission profiles assuming thermodynamic equilibrium.

which corresponds to $\sim 46\ \mathrm{M}_\odot$ in our simulation after accounting for the mass cut-offs. As noted by Zackrisson et al. [60] in the description of the YGGDRASIL metal-free stellar SED calculator, the exact form of the initial mass function (IMF) and therefore the spectra of Population III stars is a matter of great uncertainty. YGGDRASIL offers three prescriptions with three different IMFs. The PopIII.1 tool assumes a Schaerer [120] power law with slope $\alpha = -2.35$ and stellar masses from 50 to 500 $\mathrm{M}_\odot$ and models the most antecedent generation of stars prior to any radiative feedback and binary formation. The PopIII.2 model assumes a log-normal distribution with a characteristic mass of 10 $\mathrm{M}_\odot$ and models an IMF that includes stars from 1 to 500 $\mathrm{M}_\odot$ assuming primordial abundances but some impact from prior star formation and radiative processes[154]. The third model assumes a metal-enriched IMF[155] with a piece-wise power law for different mass regimes.

For this work, we determined the PopIII.1 model to be too top heavy for the lower end of our mass range and the Kroupa model to be inconsistent with the goal of differentiating metal-enriched and metal-free stellar populations so we generate our SED using the PopIII.2 model for stars smaller than 55 $\mathrm{M}_\odot$ and the PopIII.1 model for larger stars. We generate and match SEDs to the age and mass of the simulation star particles assuming an instantaneous burst. Since we treat the effect of extinction separately in our calculations, we do not include a covering fraction to produce the SED. We note that there are some discrepancies between flux of ionizing radiation modelled in the simulation and the flux calculated from YGGDRASIL due to our practice of using an average IMF to model individual stars in post-processing. We expect this to manifest as inconsistencies between the flux of ionizing radiation from the metal-free SEDs and the size of ionized regions in the simulation so we hereafter give priority to the values of electron fraction and temperature from the simulation in our radiative transfer analysis.

4.2.2 Emission Line Extinction

The antecedent treatment of emission lines from Barrow et al. [151] used the photo-ionization solver CLOUDY[125] to determine emission line strength in simulation AMR cells containing stellar populations. Line emissions were therefore limited to a small fraction of the interstellar medium (ISM) and almost none of the circum-galacitic medium (CGM). A separate Monte Carlo gas and dust extinction calculation of the continuum using HYPERION[79] was used to attenuate the lines in conjunction with an empirical correction from Park et al. [131]. In this work, we more thoroughly examine the use of CLOUDY and HYPERION as tools for emission line extinction and line transfers in arbitrary stellar, dust, and gas arrangements while eschewing the use of empirical attenuation models.

In a similar manner to our prior method, we use gas densities and metallicities from the cosmological simulation and stellar spectra to stage a CLOUDY calculation for AMR cells containing interior stellar populations. For cells with more than one stellar particle, which may include combinations of metal-enriched clusters and metal-free stars, spectra are summed into a single source for the calculation. In the simulation, stellar particles are formed within a single cell by design, but may move between cells after their formation. As a result, the highest refinement level within a halo usually contains one, or at most, a few stellar particles. However, the cells contain too little medium to calculate the photochemistry in the ISM after the tenth level of refinement. Therefore we attempt to balance this with our desire to limit the use of particle SED summing by allowing up to the ninth level of the simulation AMR grid. We run CLOUDY until the electron fraction matches the value from the corresponding cell rather than allow the calculation to come to a thermal equilibrium and apply Doppler broadening to the lines by using the temperature of the cell and the mass of the emitting molecule. We take enough samples of the spectra to produce a discernible Gaussian distribution of most lines, which increases the computational load of our

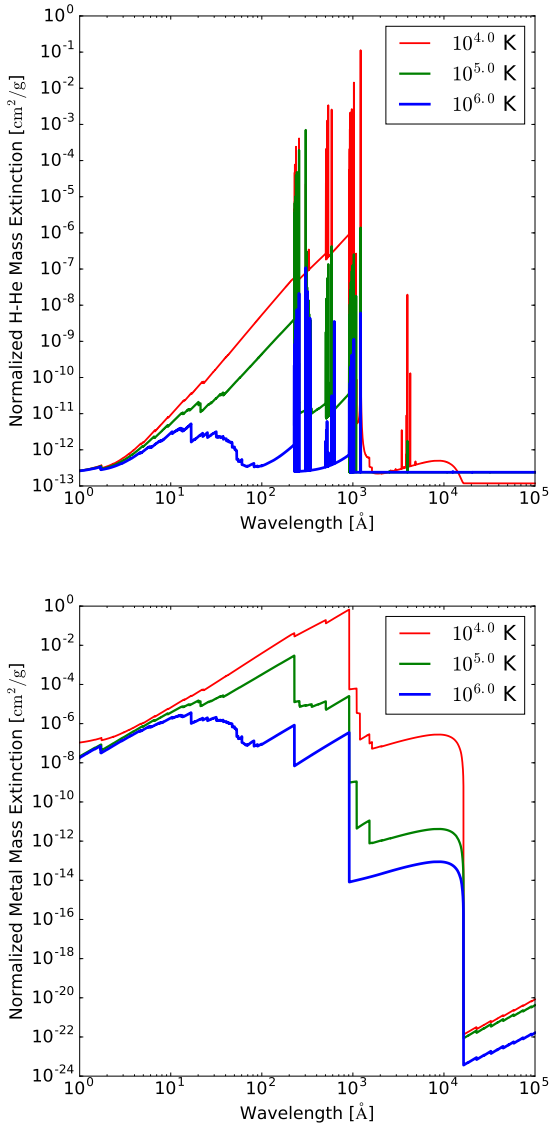

Figure 4.2: Isothermal cross-sections of extinction profiles. Left: Mass extinction coefficient for hydrogen and helium continuum and lines. Right: Mass extinction coefficient for metal lines with a hydrogen and helium continuum. Both plots are normalized by their maximum value in Figure 4.1 and are coloured red, green, and blue for gas of temperatures 10^4,10^5, and 10^6 respectively.

pipeline considerably when compared to our prior investigation. The line profiles are then redistributed back to the intrinsic spectra of each particle proportionally to their fraction of the total luminosity of the summed source. The result is usually a relatively small addition to the spectra from diffuse emission, but we include this calculation in our method to capture any unique photochemical interactions in regions with high flux from a local source.

In addition to the lines added to the intrinsic stellar spectra, we model emission and absorption more generally throughout the interstellar and circumstellar medium. To account for a chemically inhomogeneous interstellar medium, we treat our halos as similarly inhomogeneous distributions of metallicity by using the precise emission line wavelengths and source molecule to segregate line opacities and emissions generated by non-metals from those generated by metals. We calculate extinction, albedo, and emission for 400 equally log-spaced temperatures between $10^{2.5}$ and 10^{7} K using a flat spectrum in thermodynamic equilibrium and constant density and metallicity. For simplicity, we assume solar abundance patterns[130] when the metallicity of the gas exceeds 10^{-6} $Z_{\odot}$ and turn off the presence of metals entirely below that value. Extinction of lines is calculated by generating a high-resolution frequency-dependent line opacity map with Cloudy for frequencies corresponding to emission lines and adding the result to the absorption profile of the continuum. As shown in Figure 4.1, this allows us to create a profile for extinction that scales with metal density and one that scales with non-metal density. Notably, the emission profiles show a clear delineation between temperatures that represent thermally ionized hydrogen and neutral species at around 4000 K which corresponds roughly to 50% ionization of hydrogen according to the Saha equation. Both the emission and extinction profiles include the bremsstrahlung effect. For the metal profiles, we include the continuum extinction and emission due to hydrogen and helium by necessity to ensure that each photon has some extinction, but reason that this only accounts for a negligible over-

accounting of extinction by gas. Figure 4.2 shows how Gaussian broadening results in overlapping absorption profiles for species at low wavelengths, allowing metals to absorb X-ray emission efficiently. Additionally we use a third profile for dust opacities using Draine [129] ($R_v = 2.1$) that we scale as a fraction of the metal density.

Gas, metal, and dust extinction and emission profiles are used to perform a radiative transfer calculation with HYPERION by propagating 5×10^8 photons at 5×10^4 log-spaced wavelengths from 10 to 50000 Å(rest). These values are chosen such that they have sufficient resolution to capture line profiles of up to third period elements and calculate rest-frame radiative interactions from infrared through X-ray photon energies. While final emission profiles interpolate all values in the temperature range, we are forced to average extinction profiles into ten bands for the Monte Carlo algorithm. As shown in Figure 4.1, extinction for individual species usually extends across a broad range of temperatures and since the medium within each cell would likely exhibit a range of temperatures at higher resolution, our use of averaged bands is still representative of the physical analogues to our simulations without losing too many features in the profile. Compared to the antecedent method, the inclusion of opacities and emission profiles allows for the treatment of line transfer of photons from external sources, anisotropic absorption and emission lines, and calculation for emission line strength from H II regions larger than the size of a cell.

We estimate the specific radiative power of baryons in a cell by using the equation

$$\mathscr{E} = 4\sigma T^4 \frac{\int_{\nu_{\min}}^{\nu_{\max}} (\kappa_\nu/\rho) B_\nu(T,\nu) d\nu}{\int_{\nu_{\min}}^{\nu_{\max}} B_\nu(T,\nu) d\nu}, \tag{4.2}$$

in agreement with Lucy [78] where $B_\nu(T)$ is the Planck spectral radiance distribution given by

$$B_\nu(T,\nu) = \frac{2h\nu^3}{c^2} \frac{1}{e^{h\nu/kT} - 1}. \tag{4.3}$$

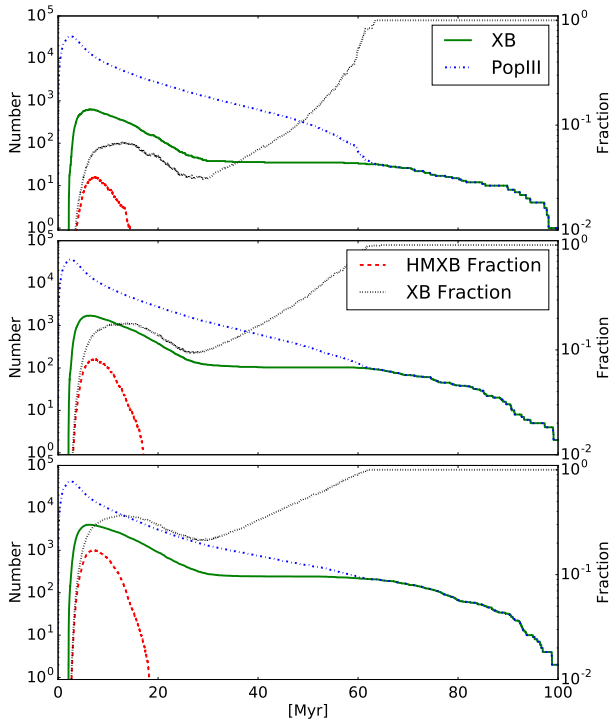

Figure 4.3: Number of Population III stars (green), number of X-ray binaries (blue), fraction of X-ray binaries (black), and fraction of high mass X-ray binaries (red) for a burst of star formation assuming that 10%(top), 25%(middle), and 50%(bottom) of the stars form initially in close binaries and accrete at the Eddington limit. The persistence of an individual particle is largely a function of sampling of the IMF, but the number and fraction of HMXBs is related to the close binary fraction.

The quantity κ_ν/ρ is the mass absorption coefficient formed by dividing the absorption opacity by the density of the medium. The other variables have their standard physical definitions. The specific power $\mathscr{E}$, determined in units of $\mathbf{erg\ s^{-1}g^{-1}}$, sets the emitted radiative power per unit mass.

We find that some lines and scenarios with high scattering opacities prove to be infeasible to model using a Monte Carlo method so we rescale the scattering and absorption coefficients to produce a physically similar phenomenon with fewer scatterings. We reason that as long as the quantity $L \times \kappa_\nu$ is a constant where L is the path length of an individual photon, the probability of absorption remains fixed. We

also reason that as long as a photon scatters at least once within a cell, the final direction of the photon is indistinguishable from a scenario where it scatters many times. Therefore, we note that the dispersion of the radius of a three-dimensional random walk is given by $\langle R^2 \rangle = N\lambda^2$ where R is the radius from the starting position, N is the number of scatterings, and $\lambda = 1/\kappa_s$ is the mean free path. The path length is simply $L = N\lambda$ and the average number scatterings before crossing a cell is $N_1 = R^2\kappa_{s,1}^2$. For a chosen maximum feasible number of scatterings N_2, we determine the corresponding scattering coefficient to be

$$\kappa_{s,2} = \frac{\sqrt{N_2}}{R}. \tag{4.4}$$

Likewise because we take the path length times the absorption coefficient to be constant

$$\frac{L_1}{L_2} = \frac{\kappa_{\nu,2}}{\kappa_{\nu,1}} = \frac{\kappa_{\mathrm{s},1}}{\kappa_{\mathrm{s},2}}, \tag{4.5}$$

and we determine the corresponding absorption coefficient to be

$$\kappa_{\nu,2} = \frac{R\kappa_{s,1}\kappa_{\nu,1}}{\sqrt{N_2}}. \tag{4.6}$$

Therefore for a given cell width, an opacity distribution, and a predetermined number of scatterings, we can recreate a physically similar scenario to the true opacities in optically thick regions. We choose N_2 to be 1000 to ensure that scatterings occur with an appropriately high resolution within a cell and only apply this correction to situations where $N_1 > N_2$. As an example, $N_2 = 1000$ corresponds to photons with a Lyman-α scattering cross-section of 10^{-16} cm^2 in a 10 parsec box and a hydrogen density of $\sim 1.7 \times 10^{-26}$ g cm^{-3}.

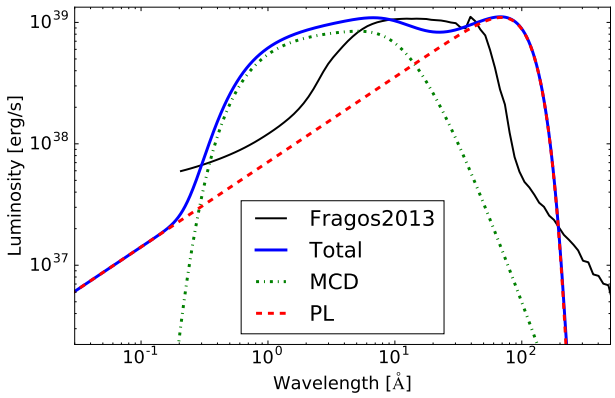

Figure 4.4: Multi-color disk (MCD) and power law (PL) components of a SED from a 40 $\mathbf{M}_{\odot}$ black hole accreting at the Eddington Limit. Absorption at wavelengths above 200 Å attenuate the power law considerably.

4.2.3 High Mass X-Ray Binaries

Armed with theoretical spectra of Population III stars and a generalized emission line routine, we extend our investigation to the impact of high mass X-ray binaries.

4.2.3 Luminous X-Ray Binary Fraction Simulation

Self-consistent formation of binary metal-free stars are outside of the scope of the cosmological simulation so we attempt to set reasonable bounds to parameters associated with their population using a semi-analytical treatment. We simulate the life cycle of a burst of Population III stars with masses sampled from the Population III IMF (Equation 3.1), mass-dependent lifetimes from[120], and an IMF-dependent stellar endpoints[156] including the possibility that no remnant is left in the case of a pair-instability supernovae. To even out statistical noise, we simulate a metal-free starburst of 36,050 systems assuming scenarios where half, 25%, and 10% of systems are formed as "close binaries." That is, the stars are close enough that should the shortest-lived member form a black hole or neutron star at the end of its life, the longer-lived member will accrete its mass onto the remnant and thus form an X-ray

binary. The number of systems comes from the integration of a star formation rate that peaks in at one million years and peters out exponentially over the next four million years. We further assume Eddington [61] mass accretion rates for luminous compact objects and recalculate the lifetime and remnant type of stars as they lose mass. These scenarios are presented in Figure 4.3 which shows that the persistence of X-ray binary systems is largely a function of lucky sampling of the IMF. The maximum number of X-ray binaries in the 50% calculation is $\sim$ **6.5** times as many as in the 10% calculation in this example, but this too is subject to the whims of random sampling for any individual halo.

For this study, we are less interested in the precise global fraction of HMXBs and more interested in whether they plausibly exist and therefore warrant study as a possible source for high energy photons in the SED of galaxies with metal-free stars. From our rough calculation, we can conclude that the presence of HMXBs are possible in any halo that once contained two or more metal-free stars from a few million years after the initial burst until about 17 Myr. Since our sample of halos focus on galaxies with mixed populations of metal-free and metal-enriched stars, we reason that most of our galaxies are subject to the region of the predicted HMXB distribution corresponding to 4-17 Myr after the starburst and indeed most halos have small populations of lower-mass, longer living metal-free stars. For that scenario, we convert as many as two of the Population III star particles into HMXBs. If the maximum age of the metal-free star particles in the halo is less than 2 Myr, we do not convert any of them into HMXBs because those stellar systems are too young to contain a compact object. We note that HMXBs are possible in metal-enriched stellar populations, but with lower frequency due to the propensity of metal-enriched gas to fragment and form less massive stars and fewer compact objects. We therefore do not include metal-enriched HMXBs in our study.

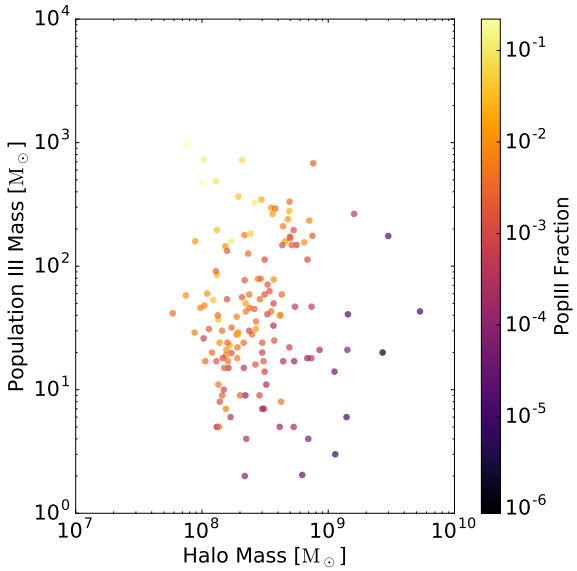

Figure 4.5: Plot of total metal-free stellar mass versus total halo mass coloured by metal-free stellar fraction of the total stellar mass.

4.2.3 X-Ray Binary Spectra

For simplicity and because of Pop III IMF uncertainty, we assume a black hole mass equal to the simulation characteristic mass of 40 $\mathbf{M}_\odot$ to calculate its spectrum. We assume a radiative efficiency of 0.1 and that emission is equally distributed between a multi-color accretion disk and a power law of the form $\dot{E} \propto E^{-1.7}$ in units of eV.

For the multi-color disk we use the temperature profile from Ebisawa et al. [68] given by

$$T_{\rm eff} = \left[\frac{3GM\dot{M}}{8\pi\sigma r^3}\left(1 - \sqrt{\frac{r_{\rm in}}{r}}\right)\frac{r_{\rm in}}{r}\right]^{1/4}, \tag{4.7}$$

where σ is the Stefan–Boltzmann constant and the innermost radius, $r_{\rm in}$, is set to six gravitational radii. We also apply the correction $T_{\rm col} = 1.7\ T_{\rm eff}$ due to the Comptonization of the disk and calculate color temperatures out to 5000 gravitational radii. A black body distribution is calculated for each temperature and weighted by the factor $2\pi r\Delta r$. The resulting distribution is finally normalized to half the Eddington

luminosity, which is given by

$$L_{\rm edd} = \frac{4\pi G M m_{\rm p} c}{\sigma_{\rm T}}, \tag{4.8}$$

where $m_{\rm p}$ is the mass of a proton. We also apply hydrogen and helium absorption to the power law assuming primordial abundances and distribute the other half of the black hole's luminosity to the absorbed result. The resulting spectra for a 40 $\mathbf{M}_{\odot}$ black hole is shown in Figure 4.4 absent the spectra for the binary star.

4.2.4 Spectral Energy Distribution Analysis

The filtering and imaging routines are effectively the same as those discussed in Barrow et al. [151]. To summarize, we calculate flux using *JWST* and *HST* filter throughputs to integrate the processed SED after applying cosmological corrections as a function of redshift. Images are created by summing photons intersecting a distant plane using Hyperion and applying noise, Gaussian blur, and the telescope's resolution when processed through a telescope prescription.

For bolometric flux, the equations are

$$d_{\rm L} = \frac{c(1+z)}{H_0} \int_0^z \frac{dz'}{\sqrt{\Omega_{\rm M,0}(1+z')^3 + \Omega_{\Lambda,0}}} \tag{4.9}$$

$$f(\nu_0) = \frac{1}{4\pi d_{\rm L}^2} \int_0^{\infty} \frac{L_\nu(\nu_{\rm e})}{\nu_{\rm e}} R(\nu_e) d\nu_{\rm e}, \tag{4.10}$$

where all variables take their standard definitions. We leave any further cosmological and instrumental adjustments like aperture and surface brightness to the reader.

4.3 Results

There are 146 halos in the "rare peak" zoom-in region of the Renaissance Simulations with active metal-free stellar populations. As shown in Figure 4.5, most of these halos

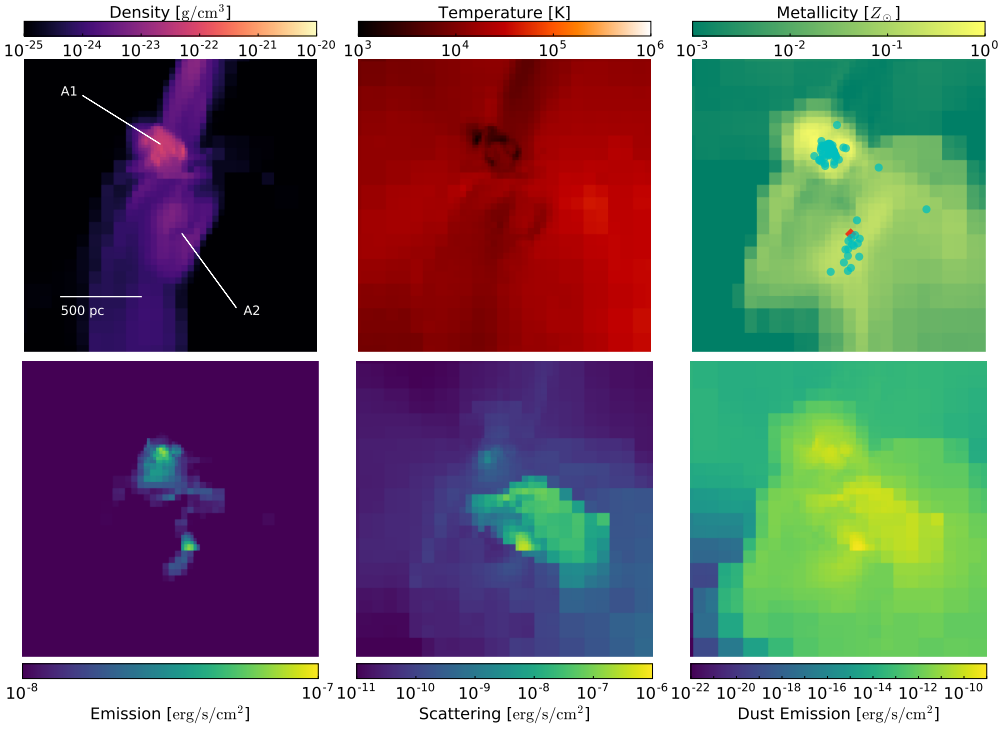

Figure 4.6: Top row: Integral of density-weighted mean density (left), density-weighted mean temperature (middle), and density-weighted mean metallicity (right). Bottom row: Integrated total emission (left), scattering per unit area (middle), and integrated dust emission (right). The location of HMXBs are shown as red circles. Cyan circles are metal-enriched stellar clusters. Subhalos A1 and A2 are labelled in the top left plot for reference.

are small with a mean halo mass of only 3.40×10^7 $M_\odot$ owing to the tendency for these stars to form and die soon after a halo first cools into molecular clouds early in its evolution. Unfortunately, small halos imply small clusters of metal-free stars and low luminosity, therefore reducing the chance of a direct observation by any telescopes planned for the near future. However, sometimes mergers can mix stellar populations and generate scenarios where larger and brighter halos are influenced by ionizing photons from Population III stars and X-ray binaries, creating an opportunity to indirectly observe these objects sooner. More rarely, a Population III starburst may occur forming a relatively bright "Population III galaxy"[e.g. 157, 158].

Our simulation shows an example of both scenarios so we dedicate the first section of our discussion of our results on those two specific halos as well as the machinery of our radiative transfer pipeline. We then explore the emission lines trends and spectra of the full sample before finally presenting our photometric results.

4.3.1 Stellar Population Merger Scenario

As described in Table 3.3, Halo A has a total mass of 1.30×10^8 $M_\odot$, a metal-enriched stellar population of 5.47×10^5 $M_\odot$, and two Population III stars totalling 6 $M_\odot$ which we treat as high-mass x-ray binaries. The halo is composed of a compact, dense ($> 10^{-23}$ g cm^{-3}) clump (sub-halo A1) merging with a larger, lower density clump (sub-halo A2) as shown in the density weighted projections in the top row of Figure 4.6. Sub-halo A1 hosts cool, metal-enriched gas while the sub-halo A2 is on average an order of magnitude hotter and hosts both metal-enriched and metal-free gas. The hottest gas ($T > 3\times10^4$ K) is concentrated in the CGM and in a supernova remnant to the right of the sub-halos as viewed in the figure. Sub-halo A2 contains the metal-free stars and by extension the HMXBs.

We integrate emission and scattering per unit volume from dust and gas along the projection axis used to produce the density, temperature, and metallicity figures

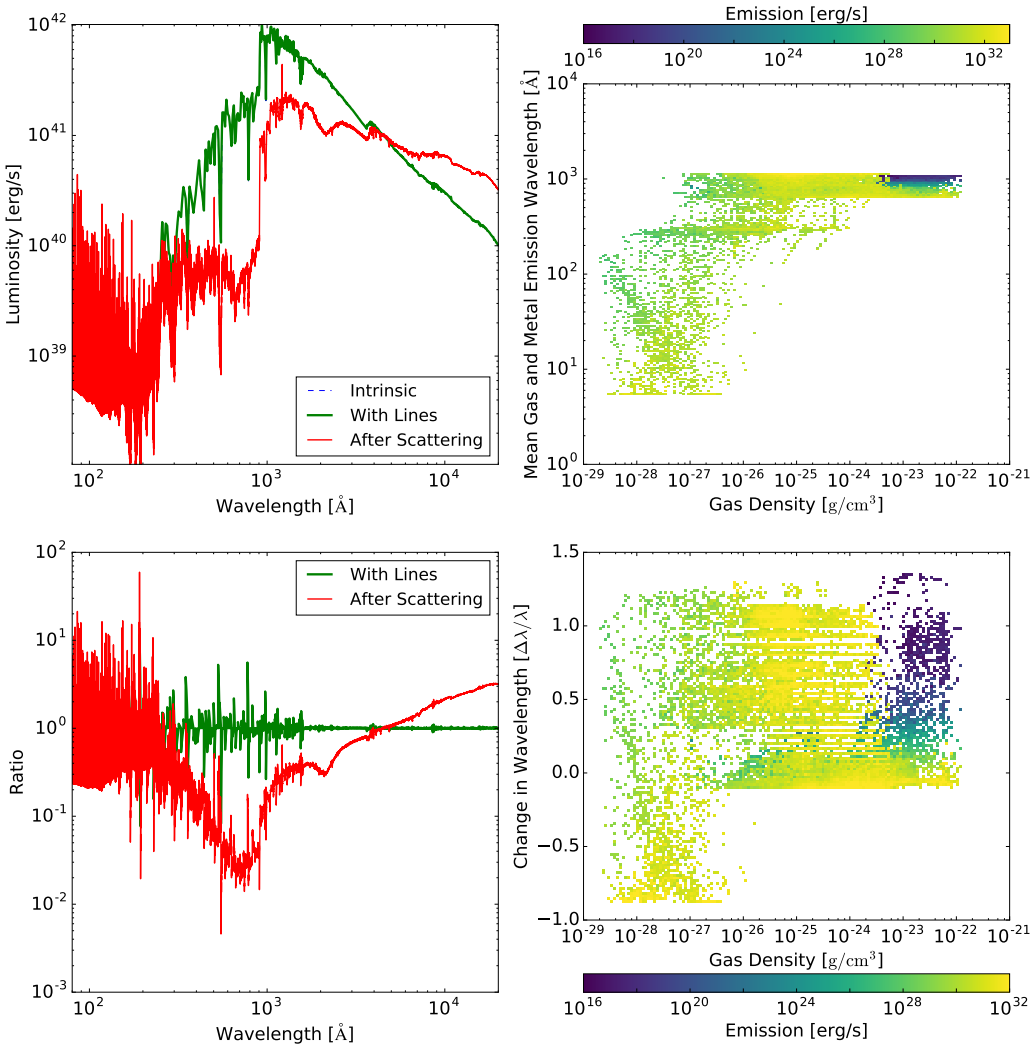

Figure 4.7: Top row: The spectra of Halo A shown before the application of lines (blue) with lines from gas in close proximity to the star (green) and after extinction (red). Here the blue and green lines appear as nearly identical in the chosen scale. The plot on the top right shows the mean emission wavelength and power of the gas as a function of gas density. Bottom row: Left-hand plot shows the ratio of emission to the nearest wavelength in the intrinsic spectrum. Some noise is present due to the relative coarseness of the intrinsic spectrum. The plot on the bottom right is the mean difference between the mean emission wavelength and the mean absorption wavelength for the combination of both gas and dust.

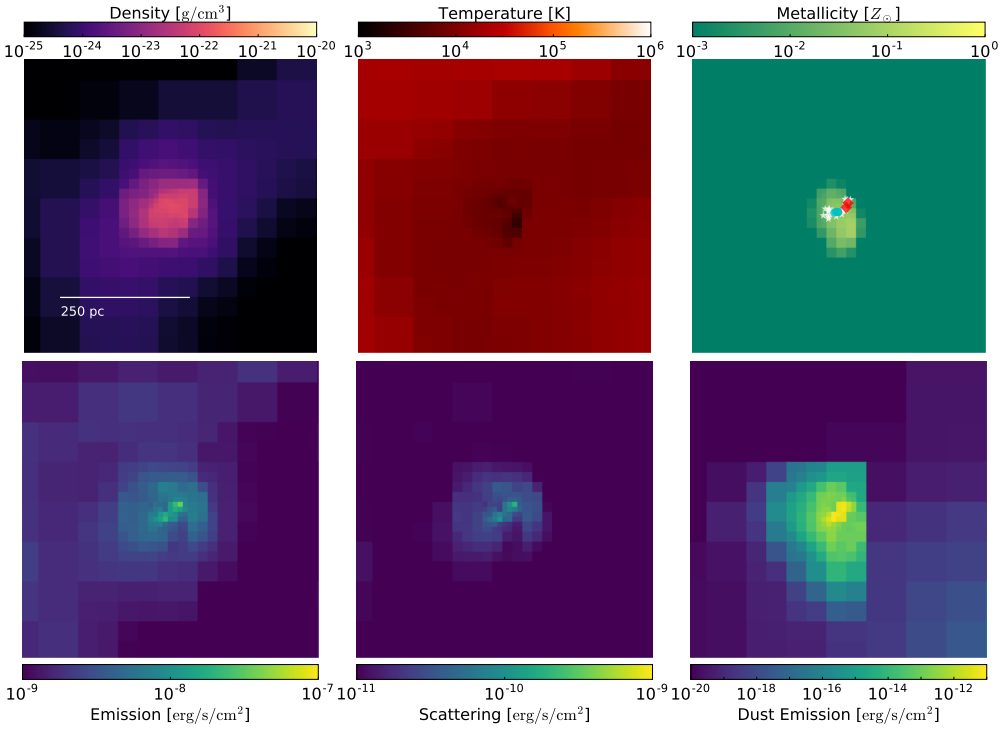

Figure 4.8: A compact Population III stellar cluster plotted in the same manner as Figure 4.6. The location of HMXBs are shown as red circles while individual Population III stars are shown in white. Cyan circles are metal-enriched stellar clusters.

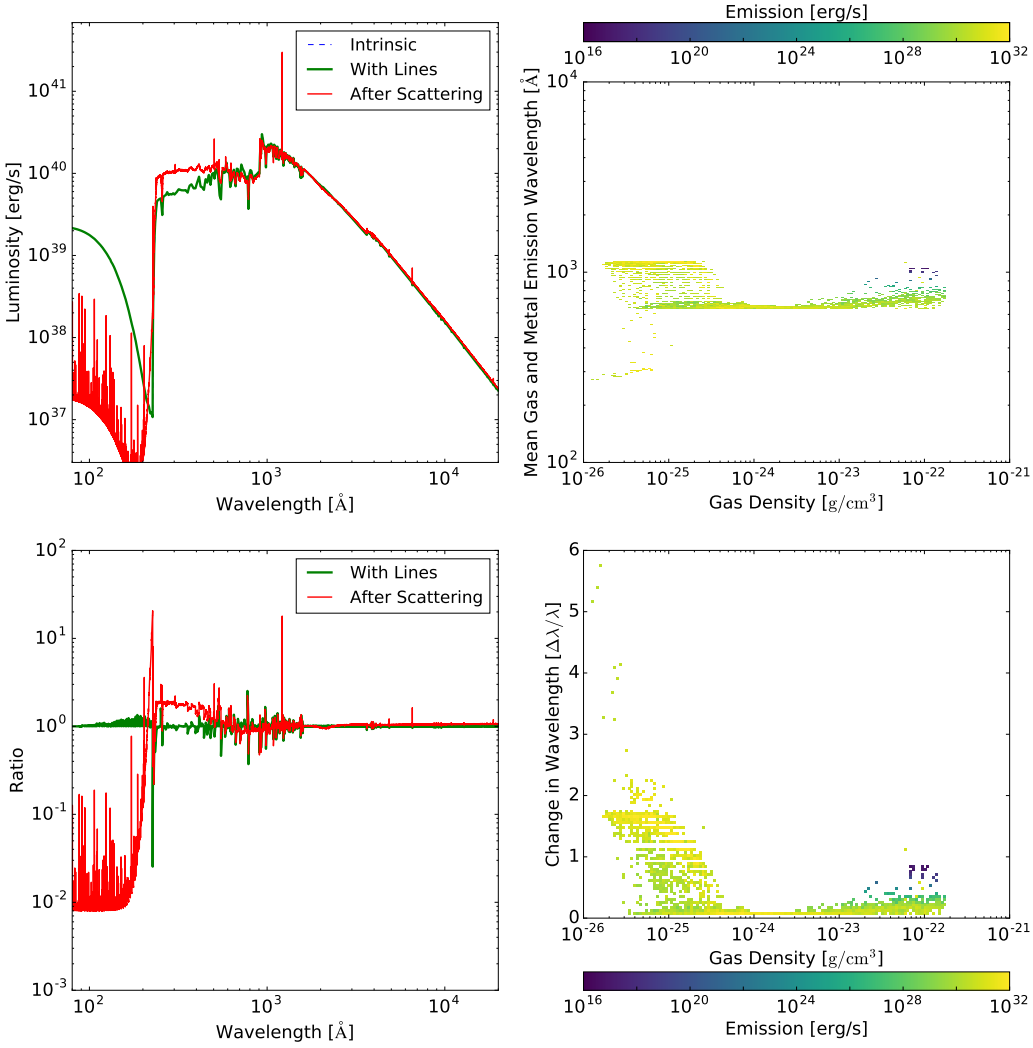

Figure 4.9: Halo B plotted in the same manner as Figure 4.7.

resulting in plots of integrated specific luminosity in units of erg $s^{-1}cm^{-2}$ which is proportional to but not equivalent to flux. Under the assumption of local thermodynamic equilibrium, the combination of dense, cool, and metal/dust-rich gas in sub-halo A1 results in thermal emission on the order of 10^{-8} to 10^{-7} erg $s^{-1}cm^{-2}$. The emission contribution from dust peaks at $\sim 4\times10^{-10}$ erg $s^{-1}cm^{-2}$ within a burst metal-enriched stars in close proximity to the HMXBs. Though this region has a lower metallicity than the peaks found in A1 as well a lower density of dust, warmer temperatures contribute to a higher overall dust emission.

To estimate scattering energy, we calculate the mean absorption-weighted albedo using the intrinsic stellar spectra and the density fraction of the constituents in the relationship

$$\langle\alpha\rangle_x = \frac{\int \kappa_{\nu,x} I_\nu \alpha_x d\nu}{\int \kappa_{\nu,x} I_\nu d\nu} \tag{4.11}$$

$$\langle\mathscr{E}\rangle_{\text{scattering}} \approx f_{\text{gas+metals}}\mathscr{E}_{\text{gas+metals}}\frac{\langle\alpha\rangle_{\text{gas+metals}}}{1-\langle\alpha\rangle_{\text{gas+metals}}} + f_{\text{dust}}\mathscr{E}_{\text{dust}}\frac{\langle\alpha\rangle_{\text{dust}}}{1-\langle\alpha\rangle_{\text{dust}}}, \tag{4.12}$$

where I_ν is the incident frequency-dependent flux. We find that the scattering in sub-halo A1 is limited to less than 10^{-9} erg $s^{-1}cm^{-2}$ while scattering in sub-halo A2 is of the order of 10^{-9} to 10^{-7} erg $s^{-1}cm^{-2}$. Taken together, this implies that the reprocessing of the intrinsic spectra in A1 is absorption and emission-dominated while the reprocessing of the high mass X-ray binaries in A2 is a roughly equally-weighted combination of gas emission, absorption, and scattering.

As shown in Figure 4.7 (top left and bottom left) there are few differences between the intrinsic spectra and the spectra with local emission lines since the regions used to calculate those lines are compact. However, the impact of extinction of the spectra through the rest of the ISM is very pronounced. High-energy photons from the HMXB are reprocessed into emission lines by the metal-enriched gas while hydrogen-ionizing radiation is absorbed and reprocessed into IR photons. Lyman-Werner absorption

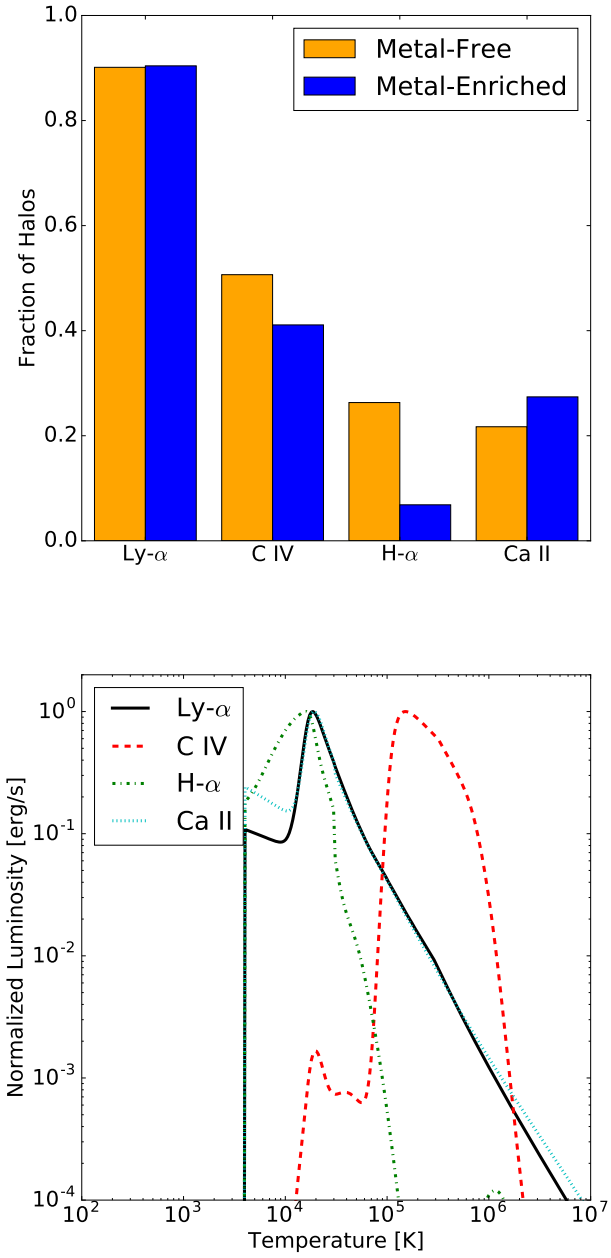

Figure 4.10: Left: Four most common emission lines amongst halos in our simulation with active Population III stars (red) and only metal-enriched stars (blue). Right: Emission versus gas temperature normalized by the maximum emission of each line calculated for a fixed density and metallicity of 10^{-25} g cm^{-3} and 0.1 $Z_{\odot}$ respectively. C IV refers to the $\lambda\lambda 1548, 1551$ UV doublet and Ca II refers to the $\lambda\lambda\lambda 8498, 8542, 8662$ IR triplet.

is also pronounced except at Lyα where a high equivalent-width line forms from excitations in neutral hydrogen within sub-halo A1. Thus, the spectra of Halo A demonstrates the signature of a cool metal-rich halo merging with a warm metal-free halo.

The components contributing to the reddening of the spectra is further demonstrated when we segregate the emission from gas and plot it against density and mean emission wavelength (Figure 4.7 top right). The hottest gas ($> 10^7$ K) forms an artificial ridge at ~ 5.3 Å at the limit of our calculation of the emission profile (Figure 4.1) and a second ridge at 1.14×10^3 Å at our minimum temperature of 316 K Between these two bounds we see that the lowest-density gas tends to be hotter and therefore more luminous per unit mass as we would expect. These bins correspond to the large number of emission lines seen at the high energy end of the post-extinction spectra. However most of the emission is coming from the cooler, medium density gas in A1. As mentioned, dust emission is weak, but present throughout the various density and temperature environments in the halo and therefore we see dust contributing to the spectra over the entire range of wavelengths simulated. The reddening plot (Figure 4.7 bottom right) shows the relative change in wavelength between absorption and emission. Like the scattering plot (Figure 4.6, bottom center), absorption wavelength is an absorption weighted mean using the intrinsic spectrum. Therefore the mean change is

$$\langle \nu \rangle_{\text{absorption,x}} = \frac{\int \kappa_{\nu,x} I_\nu \nu d\nu}{\int \kappa_{\nu,x} I_\nu d\nu}, \tag{4.13}$$

$$\langle \nu \rangle_{\text{emission,x}} = \frac{\int j_{\nu,x} \nu d\nu}{\int j_{\nu,x} d\nu}, \tag{4.14}$$

$$\begin{aligned} \Delta\lambda \approx\ & f_{\text{gas+metals}} \mathscr{E}_{\text{gas+metals}} (\langle \lambda \rangle_{\text{emission,gas+metals}} - \langle \lambda \rangle_{\text{absorption,gas+metals}}) \\ & + f_{\text{dust}} \mathscr{E}_{\text{dust}} (\langle \lambda \rangle_{\text{emission,dust}} - \langle \lambda \rangle_{\text{absorption,dust}}). \end{aligned} \tag{4.15}$$

The relative change, $\Delta\lambda/\langle\lambda\rangle_{\text{absorption}}$, shows three distinct phenomena. At the low density end, we see that the hot gas has the propensity to either increase or decrease the wavelength of the spectra for mean absorption wavelengths ~ 600 Å. For moderate densities, all the gas contributes to the reddening of the spectra, and at high densities the contribution from high-density pockets of cool gas is seen to cause low-power reddening. Since the analysis of emission and absorption are drawn analytically from bulk characteristics, they do not paint a complete picture of reprocessing of the spectra. The impact of scattering and iterative energy balance in the Monte Carlo calculation as well as the precise three-dimensional distribution of gas, metals, and dust accounts for the difference between the intuition gained in the phase and projection plots and the fully simulated result in Figure 4.7 (top left). However, we predict the signature of the merger scenario to be markers of very high and relatively low energy gas and metals within the same halo.

4.3.2 Population III Galaxy Scenario

Halo B has a total mass of 2.30×10^7 $M_\odot$, 9144 $M_\odot$ of metal-enriched stars with an intrinsic bolometric luminosity of 4.38×10^6 $L_\odot$. There are an additional 30 Population III stars totalling 712 $M_\odot$. Once again, we convert two of those stars into HMXBs with a 40 $M_\odot$ compact object accreting at the Eddington rate. Combined, the HMXBs and Population III stars have an intrinsic bolometric luminosity of 4.79×10^6 $L_\odot$ of which the HMXBs contribute 2.72×10^6 $L_\odot$ mostly in soft and hard X-rays. Thus the intrinsic spectra is dominated by HMXBs in the X-ray, metal-free stars in the hydrogen-ionizing UV band, and metal enriched stars at higher wavelengths.

As shown in Figure 4.8, allof the metal-free stars reside in the sole clump in a region of high density ($> 10^{-22}$g cm^{-3}) gas, high metallicity, and relatively low temperature gas ($< 10^4$ K). The range of temperatures are particularly remarkable because they imply that this cluster of Population III stars, the second largest in the entire simu-

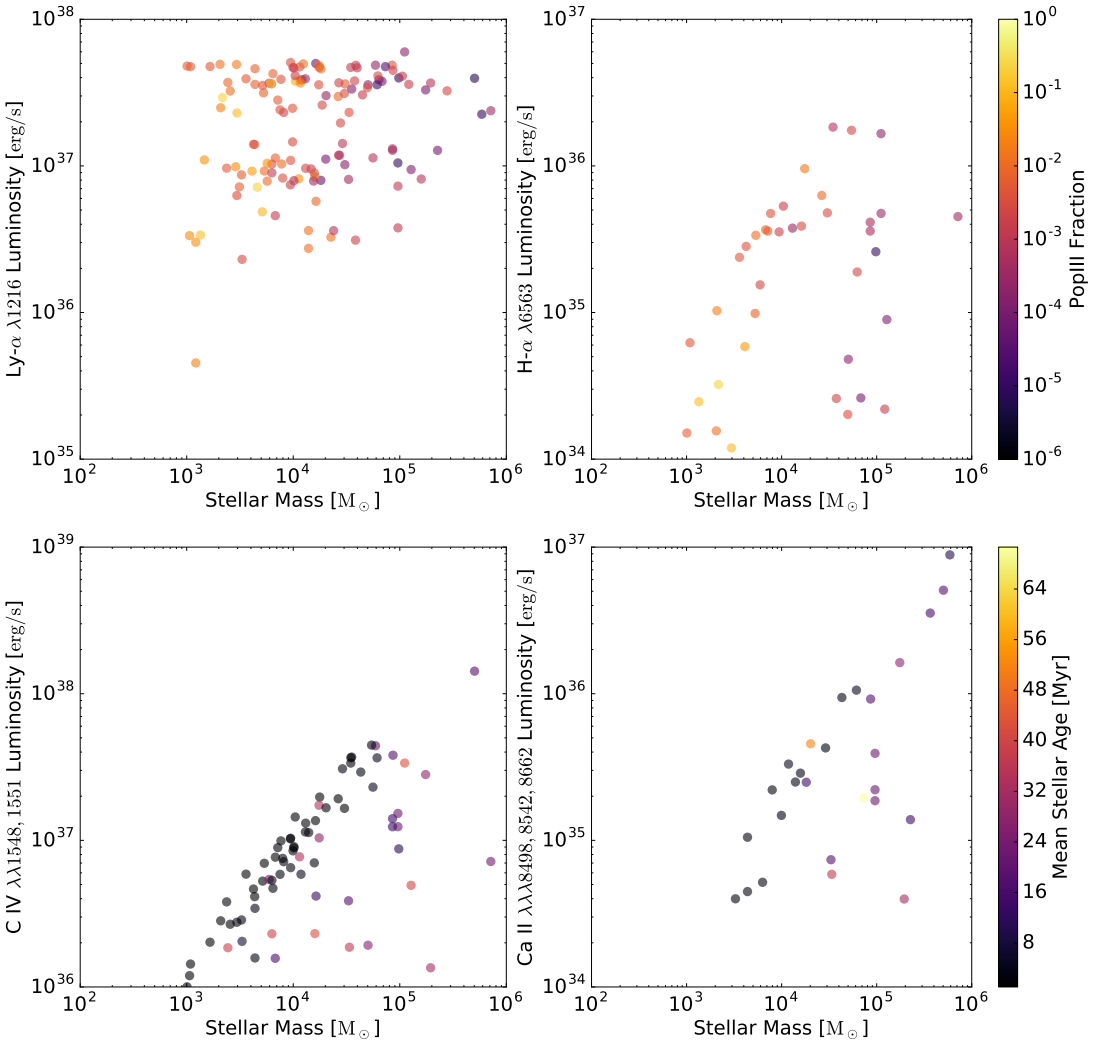

Figure 4.11: Top row: Total luminosity of Lyα (left) and H-α (right) coloured by the ratio of the mass of Population III stars to the total stellar mass. Bottom row: C IV doublet (left) and Ca II triplet (right) luminosities coloured by mean stellar age, inclusive of both metal-free and metal-enriched stars. C IV is a product of an hot plasma and a high ionizing flux. Ca II lines have been examined in the broad line regions of AGN and in stellar atmospheres.

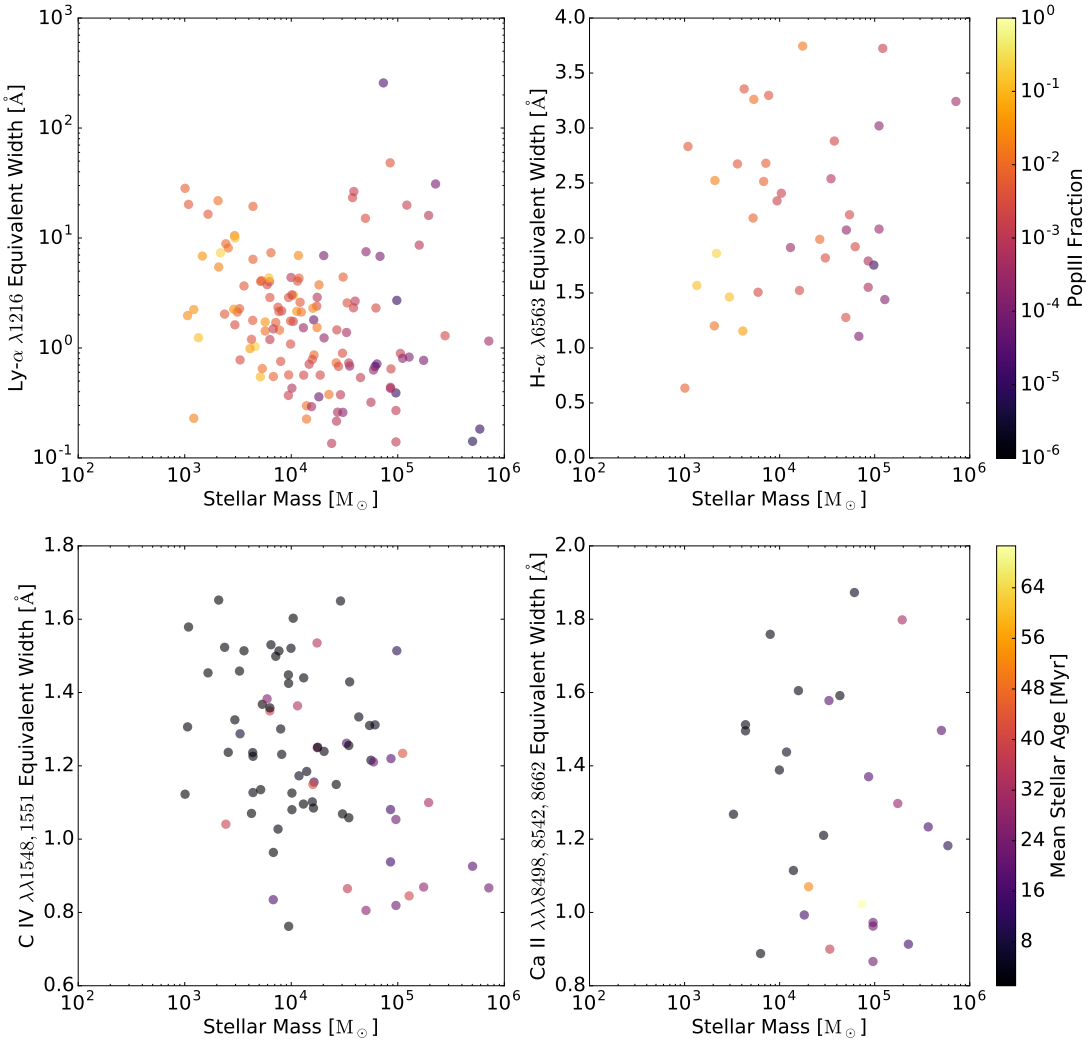

Figure 4.12: Same as Figure 4.11 but showing equivalent width rather than luminosity. Lyα equivalent width shows a negative log-log relationship with increasing stellar mass as a product of a nearly flat luminosity-mass relationship.

lation, has yet to undergo significant heating from ionizing radiation and a disruptive supernova. The cool gas results in absorption-dominated spectra reprocessing and low emittive power renders dust essentially irrelevant for our radiative transfer routines in this halo. The metal-enriched stars are embedded within the cluster of metal-free stars and have a mean age of only 3.5×10^5 yr and a mean metallicity of $0.17\ Z_\odot$ after quickly being triggered by the death of a Population III star in the cool medium.

The simple structure of Halo B results in two distinct signatures in the spectra as seen in Figure 4.9 (top left and bottom left). While Halo A reprocessed emission from the HMXB into emission lines at roughly the same wavelength, we see that Halo B absorbs those photons and re-emits them as hydrogen-ionizing radiation. Also unlike Halo A, ionizing radiation is a strong component of both the intrinsic and reprocessed spectra and stronger than in the intrinsic spectra ($f_{\rm esc} > 1$). Figure 4.9 (top right) confirms that all of the emission is confined to the UV. The estimated mean change in wavelength due to absorption and re-emission (bottom right) is reddening by as much as factor of 7 $\Delta\lambda/\lambda$.

Of the emission lines, Lyα is again the most prominent UV emission line feature and about the same luminosity as the Lyα emission in Halo A despite having a lower bolometric luminosity by about an order of magnitude. This implies that Lyα alone cannot be used to distinguish between these two scenarios, but in the presence of H-α and the Ca II $\lambda\lambda\lambda 8498, 8542, 8662$ triplet in the final spectra result from the cooler gas in Halo B.

4.3.3 Emission Lines

Since emission lines are generated as part of a Monte Carlo calculation, no *a priori* knowledge of the continuum emission can be used to identify the lines or calculate their equivalent widths. Therefore we subject the SEDs to a series of tests to determine the presence, source, and peak wavelengths of the lines based on the first

and second derivatives of the continuum. This includes a check that eliminates line candidates with equivalent widths below 0.75 Å unless the peak is two or more times the continuum, which has the effect of removing weak, but present features from our study so our counts should be interpreted as lower bounds. We also restrict our line catalogues to rest wavelengths greater than the Lyman limit.

The most common emission lines in order of their frequency within our sample are the Lyα λ 1216 line, the C IV $\lambda\lambda 1548, 1551$ doublet lines, the Balmer α (H-α) line, and the Ca II $\lambda\lambda\lambda 8498, 8542, 8662$ triplet lines which appear in the spectra of 90%, 51%, 26%, and 22% of the 146 halos respectively. To construct a control group, we found the closest match between the intrinsic JWST NIRCam F277 wideband filter of a half-sample of halos with metal-free stars to the intrinsic flux of 73 halos without metal-free stars or HMXBs within the "rare-peak" simulation at the same redshift. Within that group, Lyα was detectable in 90%, the C IV $\lambda\lambda 1548, 1551$ doublet in 41%, H-α in 7%, and Ca II $\lambda\lambda\lambda 8498, 8542, 8662$ in 27%, as shown in Figure 4.10 (left). This implies that H-α is significantly more rare or weak in the spectra of our control group than in our sample of halos with metal-free stars and HMXBs.

4.3.3 Lyman-α

Substantial Lyα emission is prominent in gas with temperatures between 10^4 and 10^5 K. Because these temperatures are associated with warm H II regions and Population III stars that are generally short-lived and embedded in their birth clouds, higher Lyα emission is a feature in most of our SEDs. Unlike the other common emission lines, we see fairly consistent Lyα luminosity between 10^{36} and 10^{38} erg s^{-1} in halos with high and low fractions of Population III stars as well as high and low masses of metal-enriched stars (Figure 4.11, top left). Consequently, there is a mostly well-correlated inverse relationship between equivalent width and both total stellar mass as well as Population III fraction (Figure 4.12, top left). As shown in [151], the mass-weighted

mean age of metal-enriched stars in halos with total stellar masses between 10^5 and 10^6 $M_\odot$ begin to settle into a narrow range as the H II regions around stars no longer encompass the entire halo. This allows star formation to transition from a series of bursts to a pattern of continuous formation. While emission continues from star-forming regions, the average stellar cluster is older and divorced from its birth molecular cloud and thus Lyα emission does not scale with stellar mass. Secondarily, the extinction cross section of Lyα photons in neutral hydrogen is high, implying that scattering through dense gas may attenuate emission along any line of sight.

While our prior treatment shows that the inverse relationship between intrinsic Lyα equivalent width (EW) and total stellar mass is generally extensible to metal-enriched stellar populations in similar environments, below 10^4 $M_\odot$, the pattern is exclusive to starbursts as several halos have had their star formation extinguished and have low intrinsic Lyα EW. For our sample, high metal-free stellar mass to total stellar mass fractions consistently exhibit the highest Lyα EWs (> 5 Å) in our sample after extinction.

4.3.3 C IV $\lambda\lambda$1548, 1551

C IV UV emission lines are an intrinsic feature of active galactic nuclei[AGN; see review by 159]. Their inclusion in our results demonstrate the consideration of line transfer from high-energy interactions to lower-energy photons in our calculations. Due to the ionization energies of carbon, C IV $\lambda\lambda$1548, 1551 emission requires temperatures between 10^5 and 10^6 K. In this temperature range, absorption cross sections are highest for X-rays in metal-enriched gas, so the presence of high-energy sources like HMXBs directly impacts the prominence of this line. The occurrence of the C IV UV emission lines in approximately half of the halos in our sample is therefore partially a product of our decision to affix a HMXB to almost all of our halos.

In environments with low-metallicity ISMs and CGMs like those we see in our

sample, X-ray escape fractions are generally high so despite a fixed number of HMXBs, the doublet's luminosity grows proportionally to the mass of the halo as seen in Figure 4.11 (bottom left). The doublet is also mostly confined to halos with very young stellar populations (< 24 Myr) as these halos are more likely to have hot gas heated either by supernovae or photo-heating from young stars. This is in contrast with Lyα emission which also implied young stellar populations but required the persistence of colder star-forming gas.

C IV UV doublet equivalent widths were consistently between about 0.8 and 1.7 Å as their strength is closely tied to absorption of the incident spectra which, in conjunction with the availability of metal-enriched gas, caps their equivalent widths.

4.3.3 H-α

The Balmer series in ionized hydrogen forms from a recombination cascade in diffuse medium. This is tempered by collisional excitations in warm gas where the density and energy of particles or photons are high enough to ensure continuous re-ionization. Balmer-series emission is more susceptible to this effect than Lyα due to the lower energy of their transitions. Thus the relative luminosity of these lines both peak and drop off at lower temperatures.

H-α luminosity scales with stellar mass and the fraction of Population III stars in our sample. As shown in Figure 4.10, H-α emission implies gas temperatures below 5×10^4 K and by extension the coolest star-forming halos and molecular clouds. However unlike Lyα emission, H-α emission has a higher escape fraction in neutral hydrogen and is therefore less susceptible to attenuation in dense gas. As shown in Figure 4.12 (top-right), H-α EW also scales weakly with stellar mass and is the only one of the prominent emission lines to do so in agreement with observations of Hα-derived specific star formation rates of higher mass galaxies at $z \sim 2$ by Erb et al. [160]. Higher fractions of metal-free stars are roughly inversely related to H-α

EW which is a function of both the overall tendency for Population III stars to be a smaller fraction of the stellar mass in larger halos and heating from metal-free stars. With *JWST*, H-α emission for objects at $z = 15$ should appear in the MIRI F1000W band. We note that IR Paschen-α transitions at 18750 Å were also present in 33 halos due to the recombination cascade.

4.3.3 Ca II $\lambda\lambda\lambda 8498, 8542, 8662$

The ionization potential of Ca^+ is $\sim$ 11.9 eV, making it susceptible to ionization by strong Lyα (10.19 eV) due to the presence of a meta-stable energy state of 1.7 eV Ca^+ that provides the difference[161]. Thus the Ca II NIR triplet emission neatly overlaps the thermal trends of Lyα and is only weakly related to temperature in its absence. Therefore, like Lyα, Ca II NIR triplet emission is tied to AGN[162] and bursts of star-formation in metal-enriched gas[163]. However, as shown in Figure 4.9, gas metal-enrichment within large Population III stellar clusters is sufficient to generate this line so its presence does not automatically indicate a metal-enriched stellar population. We observe a well-correlated power law relationship between the emission of this triplet and the luminosity of the halo and no discernible relationship in equivalent widths. These trends imply that halos are mostly transparent to Ca II emission and the precise arrangement of the gas, dust, and metals are less important than the incident flux and the temperature of metal-enriched gas. With *JWST*, Ca II emission for objects at $z = 15$ should appear in the MIRI F1280W and F1500W bands.

4.3.4 Aggregate Spectrographic and Photometric Results

We produce *JWST* colours by applying a filter throughput to our SEDs after accounting for the effects of redshifting. For our sample, we find that the intrinsic SED of our stars and HMXBs are poor predictors of the final colours produced by our radiative

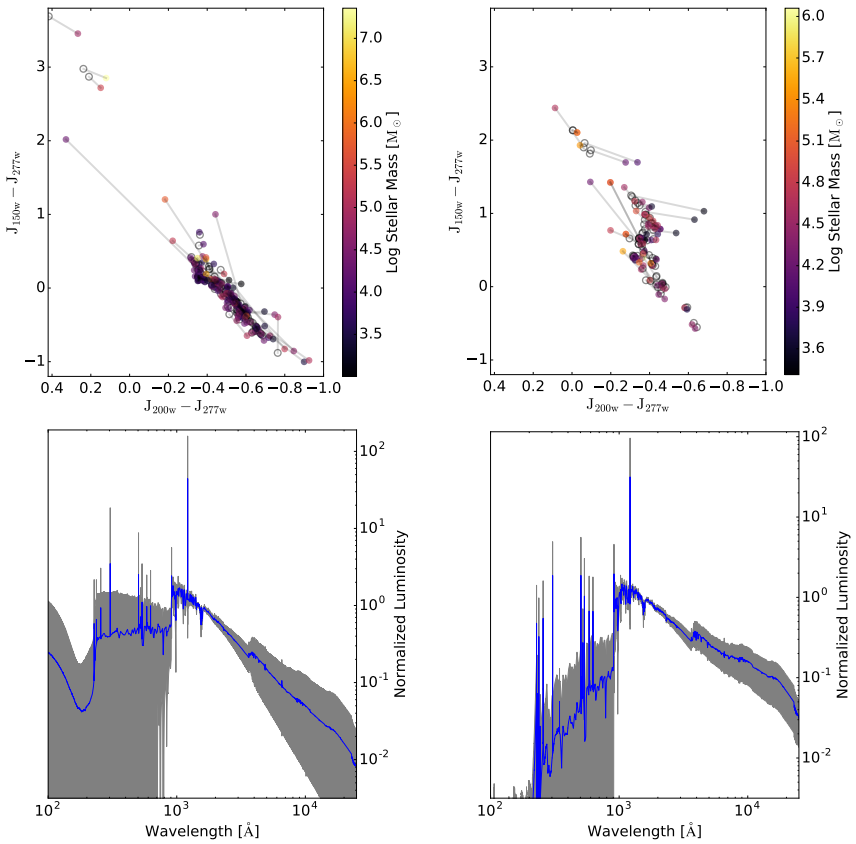

Figure 4.13: The right-hand panels show a control sample of galaxies without metal-free stars or HMXB, but with the similar intrinsic J_{277w} fluxes to our sample of galaxies with both (left-hand). Top: *JWST* colour-colour plot of the sample of halos with at least 1 $M_\odot$ Population III stars coloured by their total stellar masses at a redshift of $z = 15$. Grey points and lines show changes from the intrinsic stellar and HMXB spectra. Bottom: Mean final spectral energy distribution (νf_ν vs Å) of the sample shaded by one standard deviation above and below the mean and normalized by the values at 1500Å.

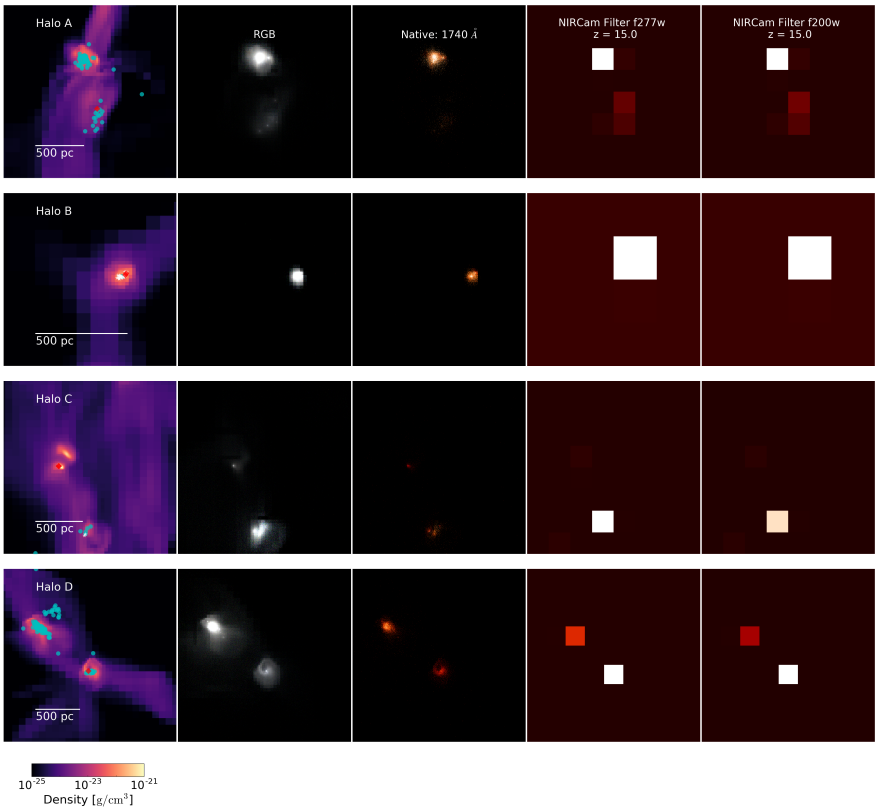

Figure 4.14: Left to right: Mean density, rest frame optical RGB composite, monochromatic image corresponding to the J_{277w} image, J_{277w} image, and J_{200w} image for halo A, B, C, and D with a magnification factor of 10 and a 1 Ms exposure time. Markers in the density plots are cyan, white, and red for metal-enriched stellar clusters, metal-free stars, and HMXBs respectively.

Table 4.1: Individual metal-poor halo properties.

Halo	$\log M_{\rm tot}$ $[M_\odot]$	$\log M_{\star,\rm ME}$ $[M_\odot]$	$\log M_{\star,\rm MF}$ $[M_\odot]$	$\log \rm J_{277w}$ [erg s^{-1}cm^{-2}]	$\rm S/N_{max}$	$\log \rm J_{200w}$ [erg s^{-1}cm^{-2}]	$\rm S/N_{max}$
A	8.47	5.74	0.78	−20.22	4.71	−20.16	2.54
B	7.69	3.96	2.85	−21.46	0.64	−21.22	1.50
C	8.65	5.49	2.42	−21.34	3.74	−21.09	5.04
D	8.56	5.63	0.48	−20.04	6.23	−19.87	4.09

Notes: The columns show halo mass, metal-enriched stellar mass, metal-free stellar mass, and *JWST* $\rm J_{200w}$ and $\rm J_{277w}$ filter fluxes at $z = 15$. Signal to noise ratios are for the brightest pixels shown in Figure 4.14 with a 1 Ms exposure time and $\mu = 10$.

transfer calculations. As shown in Figure 4.13 (top left), halos with final $\rm J_{200w} - J_{277w}$ and $\rm J_{150w} - J_{277w}$ colours around 0.45 and 0.25 respectively are likely to have changed little or reddened slightly after our calculations. Conversely, many halos with intrinsic colours in this range have their colours change drastically after processing. Shifts to a bluer colour implies reddening from higher energy photons from metal-free stars into the UV range of the filter and were mostly absent from the analysis of metal-enriched populations in the antecedent work. Drastic changes in $\rm J_{150w} - J_{277w}$ occur because the $\rm J_{150w}$ filter straddles the Lyman limit at $z = 15$ so the colour is extremely sensitive to the production and escape fraction of ionizing radiation. The prominent Lyα lines at $\sim$ 19,450 Å(observer) are captured by *JWST* NIRCam's $\rm J_{200w}$ filter with the caveat that they are likely to be subject to extinction in the IGM not captured by our analysis. We expect this extinction to be particularly prominent early during the Epoch of Reionization and will seek to capture this effect in future studies. Here, the strength of this line increased $\rm J_{200w} - J_{277w}$ colours in many low stellar mass halos, sometimes dramatically.

Figure 4.13 (bottom left) shows a composite of all the final SEDs in our sample normalized to emission at 1500 Å(rest). In addition to the oft-mentioned Lyα line, we see several lines in the Lyman continuum. We did not explore these features because we expect neutral hydrogen to drastically attenuate ionizing emission in the IGM, but we note that several strong He I and He II emission lines are present in the ISM

and CGM of most of the halos in our sample. In general, the fraction of ionizing radiation varied drastically between our halos due to the wide range of Population III stellar mass fractions. At the extremes, ionizing radiation was completely attenuated in some cases and represented the peak emitted energy in others. In the UV, results were more consistent as halos fell into the narrow range of 0.3 to 0.8 $\mathrm{J}_{200\mathrm{w}} - \mathrm{J}_{277\mathrm{w}}$ demonstrated in the colour-colour plot with a few a outliers.

The control group of 73 halos with similar intrinsic J_{277w} flux, but composed of metal-enriched stars and no HMXBs are plotted in the right-hand panels of Figure 4.13. Colours show fewer outliers are generally more red in both colors. The aggregate spectra show more prominent emission lines from metals in the Lyman continuum and a shallower UV, visual, and infrared slope.

We explore photometry for the halos examined in Section 4.3.1 and 4.3.2 as well as two more merger scenarios (Halos C and D). The composition and *JWST* fluxes for all four halos are shown in Table 4.1. For our analysis, we take background noise to be Gaussian with a mean and standard deviation given by

$$\langle N \rangle = \frac{5 \times 10^{-8} \mathrm{Jy}}{\sqrt{t_{\mathrm{exposure}}}}, \tag{4.16}$$

which approximates the sensitivity of *JWST*'s NIRCam. We choose the lower band of the pixel colormap to be the maximum of our mean noise value and one standard deviation below the mean pixel flux which produces tinting of the low flux pixels in our processed images. We take the signal to noise ratio to be the brightest pixel divided by $2\langle N \rangle$.

Each halo is brighter than the noise through *JWST* at $z = 15$ assuming a 1 Ms exposure time and a factor of 10 magnification using gravitational lensing. Generally however, galaxies of this kind are not resolved by *JWST* and extend over only 1-2 pixels. The stellar population merger scenario (Halo A) occupies four pixels and appears as two distinct sub-halos of two pixels each. The Population III galaxy

scenario (Halo B) illuminates a single pixel and produces a stronger flux in the J_{200w} filter than the J_{277w} filter, but we do not expect it to be directly observable with *JWST* at this redshift without an extensive exposure time. Halo C however also features a high fraction of Population III stars and should be observable with a S/N of 5 in our example. Halo D would be the brightest of the four, but only contains a single Population III star amidst a much more luminous metal-enriched stellar population.

4.4 Discussion

To facilitate our study of the spectrographic impact of Population III stars and HMXBs, we have contributed a few methodological improvements to radiative transfer post-processing of cosmological simulations. At the core of our calculations is the dust radiative transfer code HYPERION which we extend to gas and emission lines by creating two dimensional arrays of extinction and emission prescriptions with CLOUDY. With irony, we note that our relatively simple treatment of dust leaves the most to be desired and improvements to our dust models will be part of the focus of future investigations. However, galaxy dust ratios at high redshift have been shown to vary greatly with the assumed grain accretion timescales[164] which itself varies sensitively with ISM density[165] and composition, making dust difficult to constrain.

We also briefly explore the prevalence of high mass X-ray binaries in Section 4.2.3. Since the impetus for those calculations was a desire to physically motivate their inclusion in our study, we were less concerned with the implications of their global fraction on the cosmological environment, but that subject certainly deserves some consideration. The multi-color accretion disk model implies an inverse relationship between black hole mass and peak temperature. This suggests that larger black holes emit more of their radiation as hydrogen-ionizing photons than smaller ones, which emit most of their energy at wavelengths too small to interact with gas in the ISM and CGM, but contribute to slow heating of the IGM for photons in the 500 eV to 1

keV energy range[166]. This may have considerable implications for reionization, star formation, and estimates for escape fractions if luminous high mass compact objects are determined to be fairly prevalent. Furthermore, X-ray emission from binaries have been shown to strongly contribute to the cosmic X-ray background[112].

Generally, metal-free stars at high-redshift remain elusive to direct detection with their supernovae as the best chance of detection[e.g. 167]. Galaxies where Population III starbursts comprise most or all the stellar mass like Halo B were too small and dim to be observed with *JWST* even with generous exposure times and gravitational lensing. In scenarios with a merger between a halo with a metal-enriched stellar population and a metal-free stellar population, the metal enriched population provides enough of a boost to the luminosity to make the halo discernible, but dense gas in deeper potential wells limits the permeability of ionizing and UV radiation. In this case, it may be possible to estimate the temperature profile from the UV slope and deduce the presence of a hot, ionizing source like a HMXB or a metal-free stellar cluster. However, the best and rarest scenario for observation was a merger between two galaxies with metal-free stars (Halo C), but there was only one such configuration in our simulation comoving box size of $133.6\ \mathrm{Mpc}^3$. Therefore, we predict that direct observation is possible at this redshift, but fairly improbable with the current generation of hardware.

In their analysis of the void region of the Renaissance Simulations, Xu et al. [99] discover Population III star formation in the terminating redshift of $z = 7.6$ in halos that were generally larger than those hosting these stars in the rare peak volume. Late formation is enabled by strong LW flux from metal-enriched stars suppressing formation in the surrounding pristine gas and may continue to even lower redshift. Their sample includes rather large Population III starbursts with one in excess of $10^3\ \mathrm{M}_\odot$. There are twelve halos with active Population III stellar populations at the terminating redshift of the void simulation in a comoving volume of $220.5\ \mathrm{Mpc}^3$.

Given their luminosity and redshift, some of these would likely be detectable with *JWST*.

Our use of averaged metal-free IMF prescriptions likely has little impact on observables like colour or imaging. By maintaining the size of the ionized region and temperatures from our simulation, the effect of this discrepancy is mostly minimized to calculation of the absorbed radiative energy within the Monte Carlo step. However since observation requires either a large number of metal-free stars or a metal-enriched population, the impact of small changes in the incident spectra of individual stars is vanishingly small, especially when compared to contributions from the other factors like the impact of morphology and viewing angle when observing irregular galaxies. For a detailed study of astrophysical radiative transfer phenomena on the other hand, a more robust spectral routine would be desirable.

For objects at high redshift, emission line diagnostics serve as more of a long term prediction and a theoretical exploration with the notable exception of the Lyα line, which sits near the center of the $\mathrm{J_{200w}}$ filter at $z = 15$ and is luminous enough to impact color. This is tempered by the tendency for this line to become lost against the continuum in brighter galaxies as starbursts comprise of a smaller fraction of the emission.

For HMXBs, the C IV UV doublet is a constant companion, growing in strength proportionally to the overall luminosity of the halo due to our decision to include them in most of our sample. Since HMXBs can form in metal-enriched populations, diagnostics of this emission line are somewhat extensible to observation of these objects in the local Universe. However, both C IV and the Ca II IR triplet are already a well-established feature of the broad-line regions of nearby accreting compact objects. We find them in our control sample of metal-enriched halos as well which undermines the premise that they are unique to the presence HMXB. We will therefore wait until we perform simulations to lower redshift before we attempt to glean more about the

emission-line diagnostics of present-day HMXBs. We also note that our use of solar chemical abundances may significantly underestimate the prevalence of C IV if gas in early galaxies are carbon-enhanced due to the lack of Type Ia supernovae. H-α emission was much more prevalent in our sample of halos with metal-free stars and more luminous in galaxies with a higher fraction of these stars. Though emission is relatively weak compared to the other lines, it may serve as a potential fingerprint for this class of halos.

4.5 Conclusion

We introduce a new radiative transfer post-processing pipeline, CAIUS, for ENZO cosmological simulations which we apply to explore the observability of metal-free stellar populations and high mass X-ray binaries. Our main findings are:

1. High mass X-ray binaries would peak at about 20% of the stellar systems within a Population III starburst if it is generously assumed that half the stars form as close binaries.

2. About six halos in our sample would be discernible with *JWST* with long exposure times (1-10 Ms) and gravitational lensing ($\mu = 10$).

3. Galaxies with high fractions of metal-free stars tend to have low luminosity at high redshift. Therefore the best scenario for direct observation of a metal-free stellar population might be a merger between two such galaxies though that configuration is rare in our simulations.

4. The youth of metal-free stars implies strong Lyα emission. Lyα EW are inversely proportional to the total stellar mass of the halo. Through filters, high EW appear as an increase in $\mathrm{J_{200w}} - \mathrm{J_{277w}}$ as compared to their intrinsic values from the underlying stellar spectra.

5. The inclusion of Population III stars and HMXBs significantly increased the prevalence of H-α emission versus the control group and H-α further scaled with the fraction of stellar mass that comes from Population III stars.

6. Strong Lyα emission gives rise to the Ca II IR triplet, which suffers less extinction than Lyα while indicating the same physical scenario.

7. Our sample of galaxies with Population III stars and HMXB were generally bluer than the control sample.

We have shown the impact of ISM and CGM extinction of the gas and dust continuum as well as emission lines on galaxies with high-energy sources in the early Universe. Our prescription treats extinction and photochemistry in both optically thin and optically thick media. With our pipeline, we are able to produce synthetic photometry and further process those results into instrument-relevant data. We will continue to improve our post-processing models as we explore more cosmological scenarios.

CHAPTER 5
OBSERVATIONAL SIGNATURES OF MASSIVE BLACK HOLE FORMATION IN THE EARLY UNIVERSE

This chapter describes the implementation of the synthetic observation modeling pipeline to a simulation of a Direct Collapse Black Hole that induces star formation in its host halo. Hereafter is the work as initially submitted to Nature Astronomy in December 2017 with Aycin Aykutalp and John Wise as co-authors. The revised version of this work is embargoed due to the publication policies of Springer Nature journals. That version is under review as of March 2018.

The existence of quasars when the Universe was less than a billion years old[168–170] imply that their progenitors are seeded at very early times and grow rapidly. However, black hole growth rates[171, 172] are limited by their own radiation feedback, requiring models to either invoke very high accretion rates or a massive black hole seed[173, 174]. We study a simulation of a nascent massive, so-called direct-collapse, black hole that induces a wave of nearby massive metal-free star formation, unique to this seeding scenario and to very high redshifts. We explore its observational signatures and find that they have extremely blue colors with emission line strengths dependent on the relative strength of star formation and black hole accretion. We also find that a seed black hole produces strong, H_2-dissociating Lyman-Werner radiation. The forthcoming James Webb Space Telescope will be able to detect and distinguish a young galaxy that hosts a direct-collapse black hole at redshift 15 with a 100,000 second exposure time, critical for constraining supermassive black hole seeding mechanisms and early growth rates.

5.1 Methods

5.1.1 Simulation

We explore a cosmological simulation from Aykutalp et al. [175] studying the radiation hydrodynamical response from a direct-collapse black hole (DCBH). The simulation is run using the adaptive mesh refinement (AMR) code ENZO citep2014ApJS..211...19B initialized assuming $\Omega_M = 0.266$, $\Omega_\Lambda = 0.734$, $\Omega_b = 0.0449$, $h = 0.701$, $\sigma_8 = 0.8344$, and $n = 0.9624$ from the 7-year WMAP results[115] with standard definitions for each variable. The total comoving volume of the simulation is $(3\ \mathrm{Mpc})^3$ with a root grid size of 128^3. Three nested grids centered on the site of the DCBH are applied wherein the effective initial resolution is 1024^3. The grids are progressively refined by factors of two based on baryon and dark matter density with a maximum refinement level of 10, resulting in a spatial resolution of 3.6 proper parsecs at $z = 15$. The total mass of the halo grows from $\sim 2.6 \times 10^8\ \mathrm{M}_\odot$ to $\sim 3.0 \times 10^8\ \mathrm{M}_\odot$ over the 48.6 Myr course of the simulation we study.

Molecular hydrogen (H_2) cooling in molecular clouds facilitates their gravitational collapse, subsequently proceeding to form stars[176]. In the presence of the strong ($J_{21} = 10^3$) LW background in our simulation, H_2 dissociates according to the equation

$$\mathrm{H_2} + h\nu_{\mathrm{LW}} \rightarrow 2\mathrm{H}, \tag{5.1}$$

wherein the absorption of the photon first raises molecular hydrogen into an excited energy state. It then decays into a vibrational-rotational mode that dissociates the molecule into atomic hydrogen approximately 11% of the time[177]. Consequently, H_2 cooling and star-formation is quenched until $z = 15$ and the cloud instead collapses into a DCBH[175]. At $z = 15$, the densest cell is converted into a radiating black hole particle of mass $5 \times 10^4\ \mathrm{M}_\odot$, which then consumes gas and produces an X-ray spectrum commiserate with its accretion rate[178].

The intrinsic radiation from the DCBH particle is assumed to take the form

$$F_i = F_0 \left(\frac{E}{1\text{keV}} \right)^{-\alpha} \exp(-E/E_c), \tag{5.2}$$

in units of erg s^{-1} cm^{-2} eV^{-1} for photon energies greater than 1 keV. Here the characteristic energy, E_c, is taken to be 100 keV and the characteristic spectral index, α, is taken to be 0.9. This equation takes the form of a low energy power law and a high energy exponential cut off. The normalization F_0 is set to 10% of the bolometric flux of the black holeSchleicher et al. [179], which is assumed to convert accreted mass to radiation with a 10% efficiency factor[62].

Thermodynamics in the X-ray dominated region (XDR) are handled by a separate photochemical calculation[180]. Temperatures are pre-calculated as a function of neutral hydrogen density, metallicity, the specie number density, and impinging flux using photochemical prescriptions from Mellema et al. [181] and called in the simulation from a look-up table. For flux, attenuation of the intrinsic X-ray spectrum is estimated by integrating the opacity of H I, He I, and He II in their primordial abundance as a function of the neutral column density. The machinery of photon propagation and ray tracing between cells is handled by Moray[77], which solves the cosmological radiative transfer equation.

Hydrogen-ionizing radiation will increase the electron and proton density, which facilitates the formation of molecular hydrogen in the following reactions:

$$H + e^- \rightarrow H^- + h\nu \tag{5.3}$$

$$H^- + H \rightarrow H_2 + e^-, \tag{5.4}$$

and

$$H^+ + H \rightarrow H_2^+ + h\nu \tag{5.5}$$

$$H_2^+ + H \rightarrow H_2 + H^+, \tag{5.6}$$

as discussed in the context of numerical cosmology by Abel et al. [182]. This leads to a burst of Population III star formation when the X-rays from accretion onto the DCBH ionize the gas. The initial mass function (IMF) for Population III stars in the simulation is given by 3.1 using formation prescriptions described by Abel et al. [117] with the same parameters discussed in Barrow et al. [151]. Though routines handling metal-enriched stellar populations were incorporated into the simulation, the volume we focus on in this investigation does not include those stars during the time frame of our study.

5.1.2 Radiative Transfer Post-Processing

For post-processing, we model the spectra of metal-free stars, HMXBs, and the DCBH in a manner that diverges marginally from the underlying assumptions in the simulation, however with negligible effects on our final results. We model an accretion disk and a power law for each black hole segment of the spectra. The temperature of a multi-color accretion disk goes as

$$T_{\rm eff} = \left[\frac{3GM\dot{M}}{8\pi\sigma r^3}\left(1 - \sqrt{\frac{r_{\rm in}}{r}}\right)\frac{r_{\rm in}}{r}\right]^{1/4}, \tag{5.7}$$

as noted by Ebisawa et al. [68]. Consequently, the peak temperature of the disk goes down with increasing black hole mass. Thus for massive black holes such as the one in our scenario, disk emission contributes to the halo's intrinsic LW radiation whereas the smaller compact objects formed from metal-free stars are much more prominent at higher energies and less so below the Lyman limit. HMXBs are added to metal free stars in post-processing. Barrow et al. [9] argued that in a large sample, the number is as few as $\sim$ 4% and as many as 20% depending on whether it is assumed that

close binaries are 10 and 50 % of the metal-free star systems respectively. However, each instance is assumed to be independent which implies that as few as zero or as many as all of the stars may be HMXBs in any sample with diminishing probability. Therefore, the contribution from HMXBs may be scaled as desired to as much as 45 times the values reported here or ignored completely. X-ray observations by the *Chandra* Deep Field South survey[183] and models by Madau and Fragos [184] imply that 2 HMXBs for halos at this redshift is plausible so we adopt this value in our study. The mean size of radiating binary remnant compact objects was determined to be $\sim 40\ \mathrm{M}_{\odot}$ in Barrow et al. [9], so we appropriate this value for the black hole mass in our treatment. For the DCBH, we apply the aforementioned HMXB model to the larger mass and accretion rate of the central black hole as recorded in the simulation whereas internally, the simulation employs the X-ray spectra described by Equation 5.2. In the simulation, the luminosity of the central black hole undergoes a high-frequency duty cycle as radiation pressure extinguishes accretion and thus radiation as described by Aykutalp et al. [175].

Radiation from metal-free stars in the simulation is modelled with a monochromatic spectrum at 21.6 eV with $1.12{\times}10^{46}\ \mathrm{erg\ M}_{\odot}^{-1}$ of ionizing radiation by integrating spectra from Schaerer [120]. In post-processing, we employ the PopIII.1 and PopIII.2 spectral energy distribution (SED) models from Yggdrasil[60], using the former for stars with masses below $55\ \mathrm{M}_{\odot}$ and the latter for larger stars. All three components are modeled with high spectral resolution for all wavelengths between 10 Å and 5×10^5 Å.

The radiative transfer routines we employ in post-processing are best described by Barrow et al. [9]. In summary, we calculate opacities and emissivities for gas, metals, and dust over the range of temperatures in our simulation and the range of wavelengths in our spectral modelling using Cloudy[125]. Then we use these profiles to run a Monte Carlo photon calculation using Hyperion[79]. Our spectral resolution

allows for the production of line profiles and implicitly modeled photochemical reactions. Our use of extinction and emission profiles allows for the generation of lines and continuum effects from multiple sources in arbitrary geometric arrangements. Finally, we apply cosmological and instrument filter corrections to create synthetic photometry from our results.

UV slopes are calculated using a linear regression on the processed SEDs for wavelengths between 1200 and 2500 Å (rest) assuming the form ($f_\lambda \propto \lambda^\beta$). Because our photometry considers sources smaller than a pixel on *JWST*, we convolve the applicable point spread functions[185] after calculating intensity from redshift and cosmology. Flux through a filter is calculated as

$$f_i(\nu_{\rm o}) = \frac{1}{4\pi d_{\rm L}^2} \int_0^\infty \frac{L_\nu(\nu_{\rm e})}{\nu_{\rm e}} R_i(\nu_o) d\nu_{\rm e}, \tag{5.8}$$

where $R_i(\nu_o)$ is the filter throughput for filter i in the observer's frame, ν_e is the emitted frequency, L_ν is the luminosity, and d_L is the luminosity distance given as

$$d_{\rm L} = \frac{c(1+z)}{H_0} \int_0^z \frac{dz'}{\sqrt{\Omega_{\rm M,0}(1+z')^3 + \Omega_{\Lambda,0}}}. \tag{5.9}$$

Colors are calculated as

$$F_{2-1} = -2.5 \times \left[log_{10} f_2(\nu_0) - log_{10} f_1(\nu_0) \right]. \tag{5.10}$$

5.2 Results

We simulate the formation and evolution of a direct-collapse black hole (DCBH)-hosting halo using the radiation hydrodynamics ENZO

citep2014ApJS..211...19B code. In our simulation, star formation is suppressed by the

dissociation of molecular hydrogen (H_2) due to a strong (J_{21}[1]$= 10^3$) Lyman Werner (LW; 11.2 – 13.6 eV) background until $z = 15$, when dense gas in the center of the halo coalesces into a DCBH. Then, ionizing radiation from the accreting black hole promotes the formation of H_2, overcoming the dissociation due to the LW background. This triggers star formation in the dense, converging gas in close proximity to the DCBH. The resulting starburst forms 90 massive, metal-free "Population III" stars with an initial total mass of 6932 $M_\odot$ quickly after the coalescence of the central black hole as described by Aykutalp et al. (2018, in prep) in more detail. The radiative transfer post-processing is performed using the Caius pipeline[9] on a 2 kpc wide cube centered on the DCBH (see Figure 5.1).

We refer to the unencumbered initial accretion of the DCBH for the first ~ 2 Myr the "ignition phase". This epoch is followed closely by main sequence evolution of Population III stars during the subsequent "starburst phase", which lasts until ~ 6 Myr. That phase is characterized by extremely low DCBH accretion rates ($< 1 \times 10^{-10}$ L_{Edd}) as the gas is both evacuated from the region around the black hole as well as consumed by star formation.

As the burst of Population III stars begin to die in supernovae by 6.6 Myr (Figure 5.1), an ionized region has grown to encompass both halos and eventually the nearby circum-galactic medium (CGM). Photo- and shock-heating raises the gas temperatures to $\sim 10^6$ K, producing thermal emission with luminosities comparable to emission from the stars and compact objects. The supernovae also chemically enrich and disrupt the gas in the host halo.

Between 6.6 Myr and 11.0 Myr, the Population III stars continue to die. With the densest medium already heated and ionized, each subsequent supernovae progressively heats the entire (2 kpc)^3 region to $10^5 - 10^6$ K, delaying the formation of a second generation of stars in the enriched gas. We refer to this as the "supernovae burst

[1] $J_{21} \equiv 10^{-21}$ erg s^{-1}cm^{-2}Hz^{-1}sr^{-1}

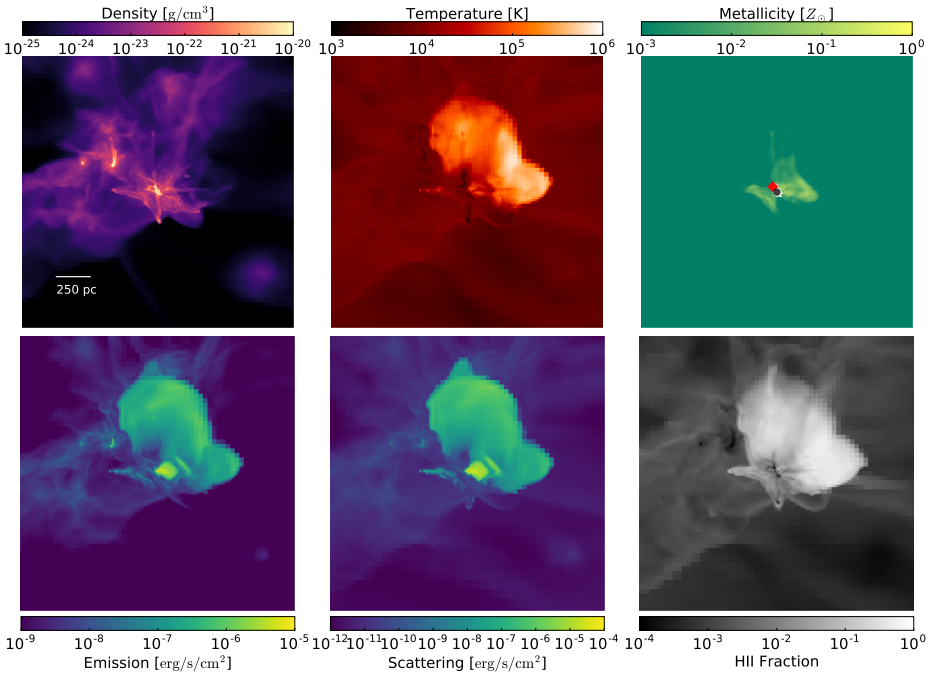

Figure 5.1: Halo during the beginning of the supernovae burst phase (6.6 Myr after the formation of the DCBH). Top row: Integral of density-weighted mean density (left), density-weighted mean temperature (middle), and density-weighted mean metallicity (right). Bottom row: Integrated total emission (left), scattering per unit area (middle), and ionized hydrogen fraction (right). In the top right plot, Population III stars are shown as white circles, the location of HMXBs are shown as red circles and the DCBH is shown as a black circle. The first supernovae after the star-formation burst are seen heating the CGM ~ 4 Myr after the insertion of the DCBH.

phase". During this phase, the DCBH initially begins to recover to a luminous, high-accretion state ($> 1 \times 10^{-4}$ L_{Edd}) before the supernovae-driven evacuation of the gas drives accretion down a quiescent level ($\sim 1 \times 10^{-10}$ L_{Edd}) at ~ 11 Myr. Despite the force of the supernovae, little of the gas permanently escapes the central halo due to the halo's deep and peaked potential well.

After the death of the last Population III star, the heated region finally begins to cool and recombine. As the gas loses thermal support, it falls back into the halos, further cooling and condensing. Figure 5.2 shows the halo 26.5 Myr after the

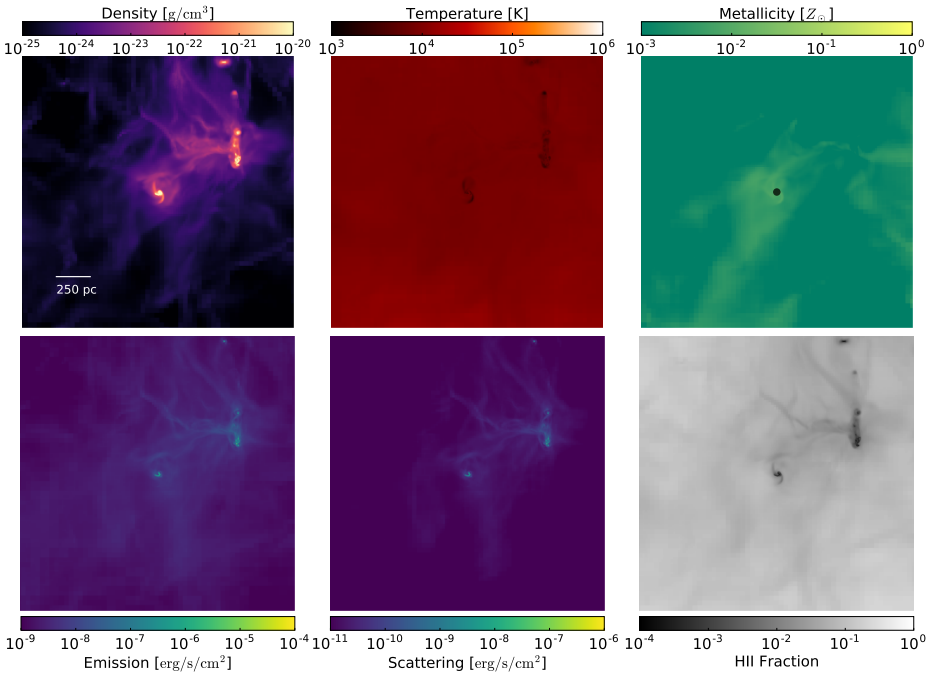

Figure 5.2: High accretion phase during the recovery phase (26.5 Myr after the formation of the DCBH) plotted in the same manner as Figure 5.1.

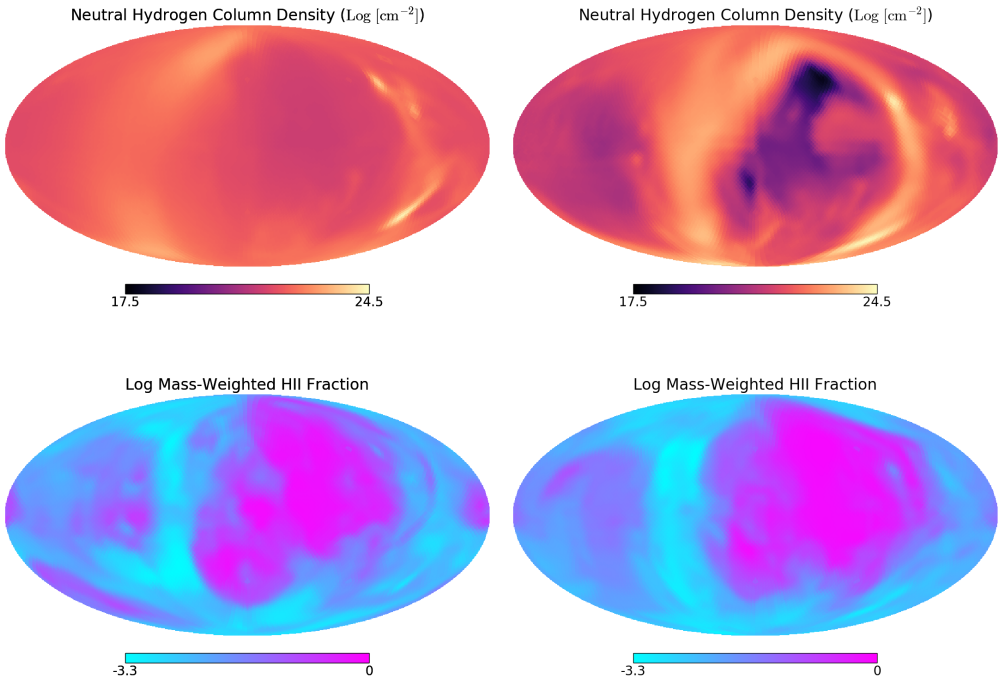

Figure 5.3: Physical parameters as a function of angle for the 6.6 Myr (left column) and 26.5 Myr (right column) points shown in Figure 5.6. From top to bottom are neutral hydrogen column density and mean H II fraction as labeled. Viewing angles were chosen with the aid of HEALPix[76]. Asymmetries are present in the temperature profile, the H II fraction, and the density profile. Accordingly, the composition and morphology of the medium acts to direct and attenuate radiation through channels about the central halo during the early starburst phase. The neutral hydrogen column density from the black hole outward to 1 kpc varies between $10^{21.4}$ and $10^{24.3}$ cm^{-2} at 6.6 Myr (top left) and between $10^{17.9}$ and $10^{24.4}$ cm^{-2} at 26.5 Myr (top right) depending on the angle (top row).

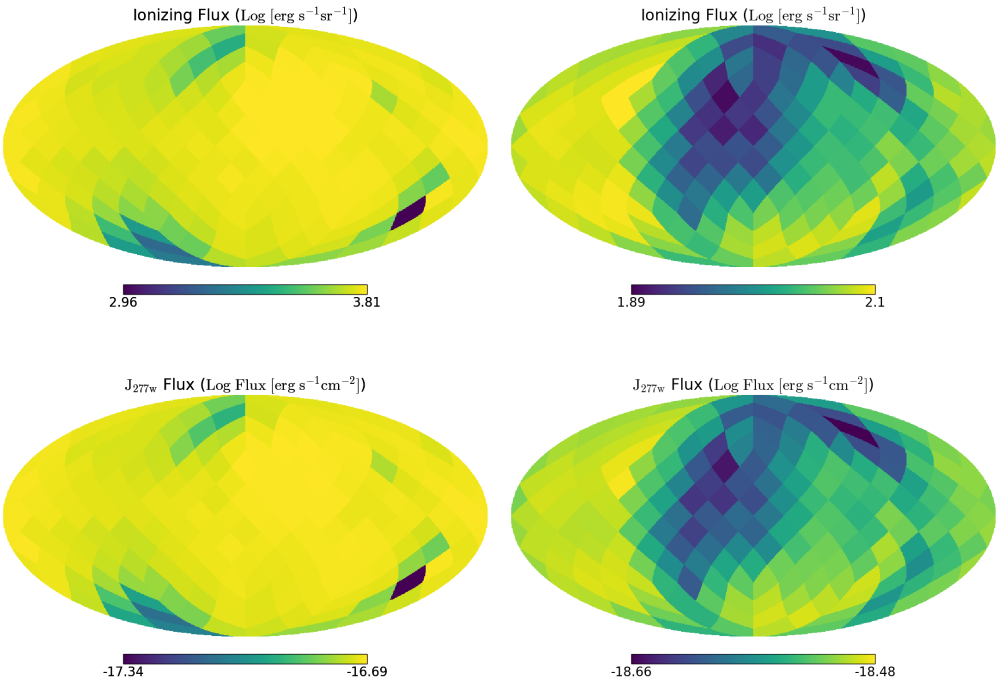

Figure 5.4: Observational parameters as a function of angle for the 6.6 Myr (left column) and 26.5 Myr (right column) points shown in Figure 5.6. From top to bottom are ionizing flux and $\mathbf{J}_{277\mathrm{w}}$ as labeled. Ionizing radiation varies by a factor of 7.08 at 6.6 Myr and only by a factor of 1.62 at 26.5 Myr (first row) as the medium becomes more isotropic. The observer's $\mathbf{J}_{277\mathrm{w}}$ flux at 6.6 Myr is also significantly higher and more varied than at 26.5 Myr (last row). Taken together, anisotropies are important in the ignition and starburst phase and less so through the supernovae burst and recovery phases.

formation of the DCBH. Here gas emission is mostly confined to emission lines and reprocessing of far ultraviolet and X-ray photons from the DCBH to energies below the hydrogen Lyman limit ($E = 13.6$ eV). This effect is aided by the dispersion of the metal-enriched gas through the CGM, which increases the absorption cross section at energies beyond the hydrogen and helium Lyman limits. We refer to this period as the "recovery phase". Herein the DCBH enters routine duty cycles of high and low accretion states and the thermodynamics of the halo CGM tends towards isotropy. Figure 5.3 and 5.4 show the characteristics of the 6.6 Myr and 26.5 Myr timesteps as a function of viewing angle to elucidate the asymmetrical radiation field of halo.

Several different mechanisms and sources contribute to the CGM spectra, which in turn contribute to varying fractions of luminosity as the system evolves with time. While active, metal-free stars are the largest component of the intrinsic LW radiation field, $\mathbf{LW_{in}}$, as shown in Figure 5.5 (top), but at 1 kpc from the DCBH, the radiation is boosted by the presence of hot gas during and after the supernovae burst phase. At this distance, the spectral radiance of $\mathbf{LW_{in}}$ fluctuates between $J_{21} = 0.7$ to as much as $J_{21} = 13$ during the recovery phase and peaks at $J_{21} = 55$ ($J_{21,\mathrm{LW}} \approx 1.38 \times 10^3$ at 200 pc) due to reprocessing of the $\sim 1.4 \times 10^{-3}$ $\mathrm{L_{Edd}}$ luminosity of the accreting black hole at the onset of the starburst phase. This DCBH-induced LW source may have strong implications for the nature of the background LW radiation field and the formation of subsequent DCBHs in proto-cluster environments that will host quasars at later times.

Also notably, $\mathbf{LW_{in}}$ is attenuated by molecular clouds as the starburst phase progresses. This implies that Population III stars are not significantly contributing to the extra-galactic LW field after their formation in this scenario.

High mass X-ray binaries (HMXB) form when one member of close Population III binaries die and leaves a compact remnant. HMXBs are a significant source of high-energy photons from the halo. However, we find that they are irrelevant to

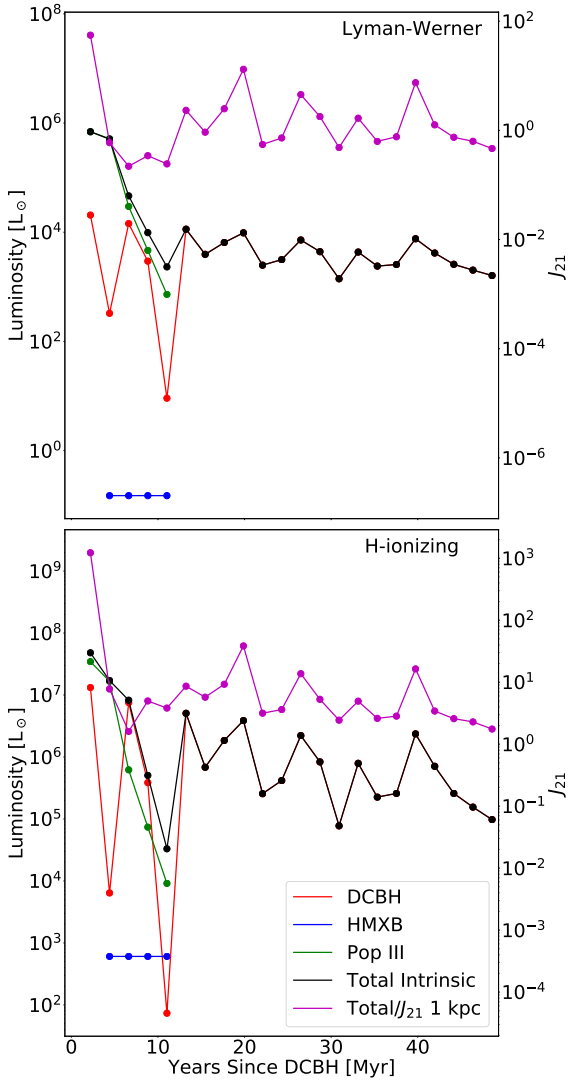

Figure 5.5: Evolution of the radiation field over time by source. Top: Intrinsic Lyman-Werner (LW) radiation by source as the halo evolves taken from the first time step after the formation of the DCBH. Also plotted are the total intrinsic LW radiation from point sources and the total, including diffuse emission, LW radiation field at 1 kpc (in J_{21} units on the right) from the central black hole. Bottom: Intrinsic hydrogen-ionizing radiation (13.6 – 100 eV) plotted in the same manner.

$\mathbf{LW_{in}}$ and contribute a marginal intrinsic hydrogen-ionizing radiation (13.6 - 100 eV) of 6.06×10^2 $L_\odot$ compared to the minimum total intrinsic ionizing field strength of 3.30×10^4 $L_\odot$ as shown in Figure 5.5 (bottom). The trends for ionizing radiation from metal-free stars and the central black hole are otherwise similar to those for $\mathbf{LW_{in}}$. This includes the attenuation of the intrinsic field during the first ten million years, however ionizing radiation is less boosted during the recovery phase at 1 kpc than LW.

We focus our study of the spectroscopic character of the scenario on four representative snapshots representing quiescent and luminescent periods of the DCBH during the beginning of the supernovae burst phase and during the middle of the recovery phase. Figure 5.6 shows the intrinsic and processed spectra of the DCBH scenario and compares this result to a sample of halos with similar intrinsic *James Webb Space Telescope*(JWST) $\mathbf{J_{277w}}$ fluxes from the rare peak volume of the DCBH-less ***Renaissance Simulations***[2, 112] before and after processing. As shown in the top panels of Figure 5.6, emission lines are not a prominent feature of the spectra during the starburst phase. This is due to two phenomena. First, the thermal energy from the supernovae and metal X-ray absorption heats a large volume of pristine gas outside the halo to temperatures from $\sim 10^4$ K to as high as 10^6 K. This produces strong continuum emission while precluding the emission of hydrogen and helium lines. Second, the metal-enriched region in the dense core near the DCBH is relatively cool and therefore less luminous (see Figure 5.1). Hence, the lack of lines is an identifying characteristic of the starburst and supernovae burst phases in this scenario. Compared to the control group, the DCBH has a steeper UV slope[3] ($\beta = -3.24$ and -3.27 versus -1.95 and -2.03 from left to right), stronger Lyman continuum radiation, and weaker Ly-α and other emission lines.

Figure 5.6 (bottom row) shows prominent emission line features during both the

[3]UV slopes are between 1200 and 2500 Å.

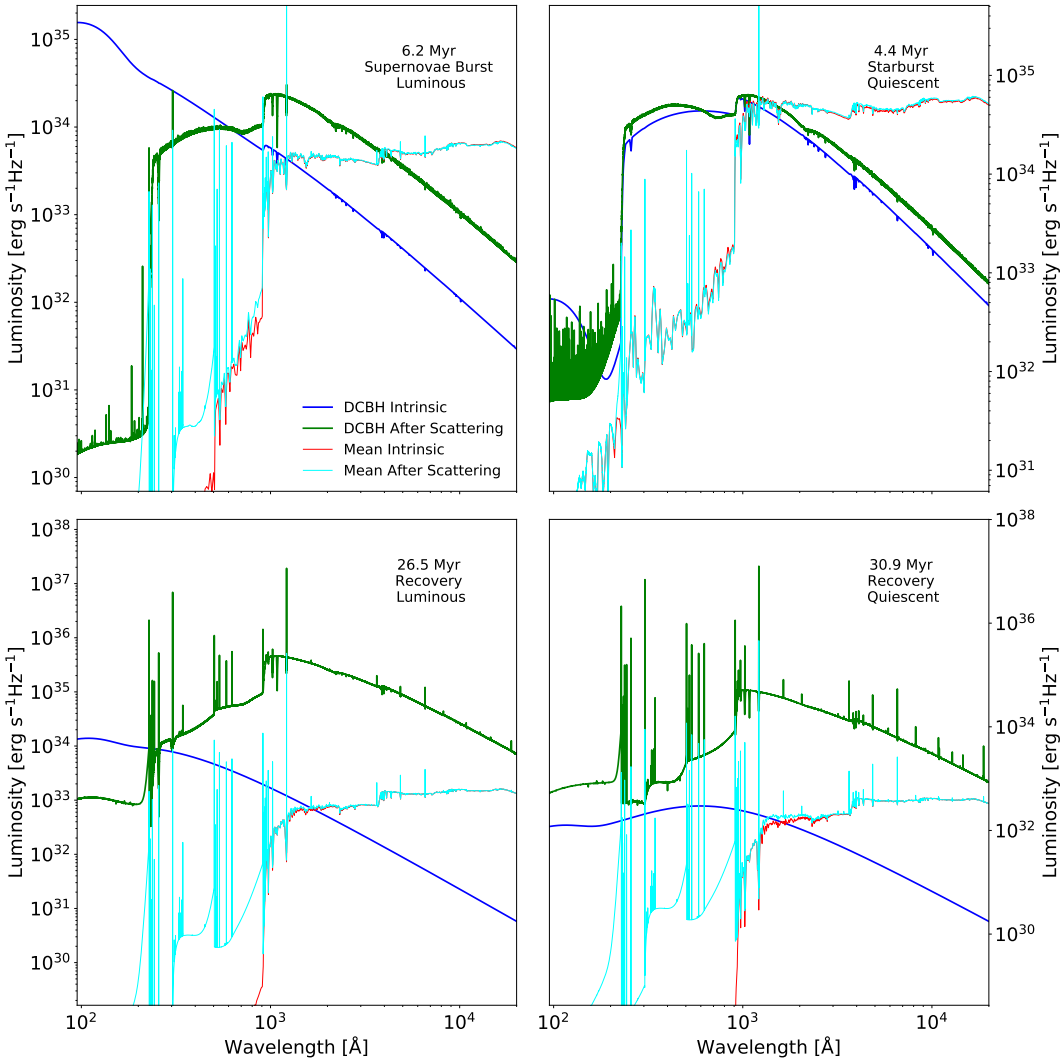

Figure 5.6: The intrinsic spectra of the DCBH scenario (dark blue) and the processed spectra of the DCBH scenario (green) plotted against the intrinsic (red) and processed (cyan) spectra of a sample of halos in the DCBH-less "rare peak" ***Renaissance Simulations*** that have intrinsic J_{277w} fluxes comparable to those from this scenario. The left panels correspond to periods of high DCBH accretion and the right panels correspond to quiescent periods. The top panels are during periods with active Population III stars and the bottom panels are without.

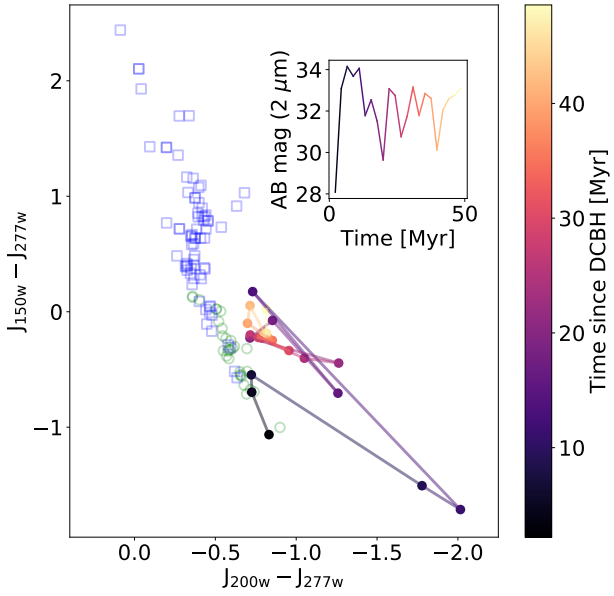

Figure 5.7: $J_{200w} - J_{277w}$ and $J_{150w} - J_{277w}$ color-color plot with magnitudes as defined in Equation 5.10. For comparison, we show galaxies from the Renaissance Simulations with more than 1% of their stellar mass in Population III stars (green circles) and comparably luminous galaxies with only metal-enriched stars (blue squares). The color-color path of our DCBH-hosting galaxy is tinted by Myr since the formation of the central black hole. The inset shows the monochromatic 2 μm AB apparent magnitude of the halo at $z = 15$ as a function of time for reference.

luminescent and quiescent periods of black hole accretion during the recovery phase. Spectra also demonstrate a steeper UV slope ($\beta = -3.07$ and -3.11) than the control group ($\beta = -1.41$ and -1.19)[4]. Since the medium is chemically enriched, X-ray photons are absorbed by heavier species and re-emitted at lower energies. This boosts the UV spectrum by as much as several hundred fold. We also find that sources of diffuse emission are mostly confined to the densest region closest to the black hole. Due to the ionization of the CGM during the starburst phase, UV and soft-X-ray photons easily escape the halo and reionize the local IGM.

The best chance of discerning this DCBH scenario from a more conventional cluster

[4]See Barrow et al. [151] for a discussion on the UV slope of low luminosity halos.

of Population III stars is late in the supernovae burst phase when the UV radiation is most boosted. As shown in a *JWST* color-color diagram (Figure 5.7), the scenario begins with colors similar to Population III clusters in the rare peak of the ***Renaissance Simulations***. However, during the supernovae burst phase, the colors diverge strongly towards the blue end in both $J_{200w} - J_{277w}$ and $J_{150w} - J_{277w}$. Then, colors return to typical $J_{150w} - J_{277w}$ values while meandering around bluer-than-typical $J_{200w} - J_{277w}$ values during the DCBH accretion-dominated recovery phase. Colors settle into a tighter, but unique range towards the end of the simulation. Thus, for all but the first 7 Myr, the colors of the halo are distinct enough to distinguish between this scenario and other galaxy types.

One of the best chances to directly observe this DCBH scenario at $z = 15$ with *JWST* is during the luminous period at the beginning of the supernovae burst phase. As shown in Figure 5.8 (bottom row), the galaxy would be plainly visible but unresolved after 6.6 Myr through the J_{200w} and J_{277w} filters with a S/N_{max} of 5.5 and 8.1 respectively assuming a 10^5 s exposure and no gravitational lensing. Unfortunately, the color of the halo would be similar to that of a Population III cluster at this time. This might not pose a problem for two reasons. First, while the halo has the same color as a young Population III galaxy, it is far more luminous than any similarly-colored galaxy in the rare peak of the ***Renaissance Simulations***. Second, color progresses quickly in the supernovae burst phase and the DCBH remains in a high-luminosity state for at least 1 Myr[175]. Between 6.6 Myr (third location along the track in Figure 5.7) and 8.8 Myr (fourth location), the DCBH-hosting galaxy is extraordinarily blue and luminous for a period of time.

The most discernible and detectable point is at 2.2 Myr (Figure 5.8, top row) due to the full contribution of the 90 Population III stars in conjunction with a strongly accreting DCBH. At this moment, a 10^5 s exposure with *JWST* will result in a S/N_{max} is 12.4 and 19.5 in the J_{200w} and J_{277w} filters respectively. The galaxy

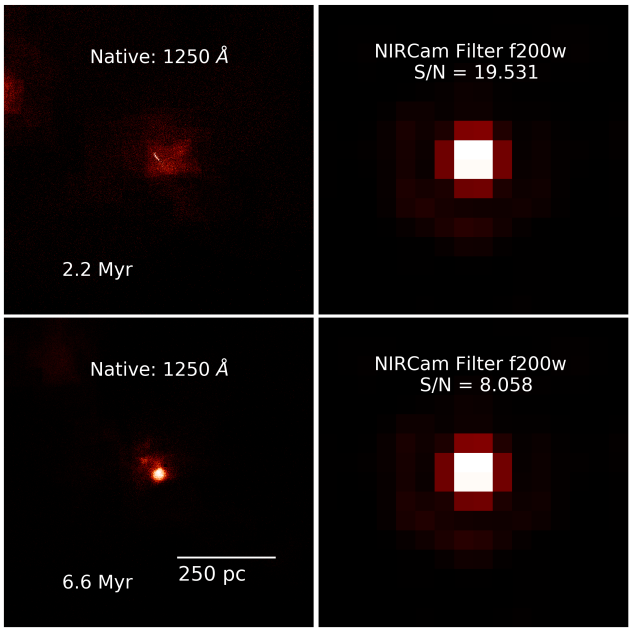

Figure 5.8: Native (left column) and processed monochromatic images (right column) of the halo during the luminous period of the supernovae burst phase in Figure 5.6 (top left). Native images are 800 pc wide with a spatial resolution equal to the simulation and synthetic JWST images are 0.5 arcseconds wide. Synthetic images employ the NIRCam point spread functions.

produces colors commiserate with an extremely young, large cluster of metal-free stars at this timestep. While the simultaneous formation of so many metal free stars is a consequence of and likely unique to this scenario, the abrupt transition from dense gas to a DCBH may need closer consideration before firm conclusions are drawn about the precise nature of the object during and immediately after the ignition phase.

In summary, we show that a scenario in which a DCBH induces a Population III starburst with X-rays would be detectable with *JWST*'s NIRCam instrument at $z = 15$. Chon et al. [186] show that requiring a $J_{21,\mathrm{LW}} = 10^4$ as a precondition for suppressing Population III formation and generating a DCBH implies a scenario number density of approximately one object per 172 (cMpc h^{-1})^{3}Myr^{-1}, peaking at $z \approx 15$. This translates to a sky density of approximately one object per 245 square arcminutes at $z = 15$ assuming a 2 Myr time of visibility for each DCBH. Our study of LW radiative transfer also suggests that the conditions that triggered the formation of a DCBH are further fueled by it. Sources like nearby star-forming galaxies may trigger the formation of an initial DCBH[187], starting a positive feedback cycle that promotes the formation of other DCBHs, boosting their number density in proto-cluster environments.

5.2.1 Comparisons to Literature

Pacucci et al. [188] also simulates DCBH spectra and predict telescope colors, however with a different method. Their black hole SED is drawn from Bruzual and Charlot [57] and they predict emission line strengths from empirical relationships[138]. They simulate $\sim 10^{4-5}$ $\mathrm{M}_\odot$ DCBH seeds that evolve into a $\sim 5 \times 10^6$ $\mathrm{M}_\odot$ black hole under the assumption of fast accretion and a Compton-thick halo neutral hydrogen column density ($N_\mathrm{H} \geq 1.5 \times 10^{24}$). However, our results show a relatively thin, ionized medium (see Figure 5.3) with slow accretion due to supernovae feedback after the initial formation of the DCBH. Where our reprocessing boosts UV due to the hot gas

in our scenario, they predict cooler temperatures and reprocessing of emission to the infrared. However, we generally concur with their claim that a DCBH is observable with colors that can diverge from that of starbursts alone and expand this conclusion to slower-accreting situations and the Cosmic Dawn ($z \approx 15$).

Natarajan et al. [189] model the formation of and accretion onto a 10^5 $M_\odot$ DCBH seed using a 1-D model to produce synthetic spectra. They use CLOUDY to process emission and produce emission lines assuming a single combined source for the black hole and stars and homogeneous medium properties. Their spectra show strong attenuation of ionizing radiation beyond the hydrogen Lyman limit where our models show limited attenuation and even boosting up to the helium Lyman limit. This difference is again due to the heating we see due to the burst of supernovae. Though we agree with their conclusion that a DCBH embedded in star formation would be roughly observable with JWST, differences in our simulation of the medium lead us to predict a bluer spectrum than their predictions.

Our DCBH-hosting galaxy is observed by its impact on star formation and reprocessing of emission in a large H II region rather than directly through high rates of accretion. Indeed, because our accretion rates are substantially less than the near-Eddington and even super-Eddington rates examined by the above works, our analysis leads to a branch of DCBH spectral characteristics that are distinct from those in the literature. Specifically, we focus on observing the few million years right after the formation of a DCBH at high redshift to probe feedback mechanisms unique to a fully 3-D prescription.

CHAPTER 6
CONCLUSIONS AND FUTURE WORK

We describe a pipeline for generating synthetic observatoins of high-redshift ($z \geq 13$) from cosmological simulations. This pipeline includes prescriptions for nebular emssion lines, stellar and black hole radiation, dust and gas reprocessing, and telescope effects. We applied it to a $(4\ \mathrm{cMpc})^3$ ***Renaissance Simulation*** with 1654 galaxies and a direct-collapse black hole simulation of a single galaxy. As of this thesis, our analysis is the most robust synthetic oberservation calculation of its kind and reveals several novel trends and some new physical insights as summarized below.

1. **Chapter 3.** Since star formation and death are disruptive phenomena, feedback processes can delay or extinguish future star formations in small halos. Thus smaller halos will tend to have older, redder stellar populations and shallower UV slopes. This is a known feature of present-day globular clusters, but our calculations predict that this effect dominates the UV slope of objects as early as $z = 15$.

2. **Chapter 3.** The variation between the spectra of galaxies decreases with mass. As the mass of galaxies increase, they are less susceptible to dispersion by supernova feedback and observational characteristics of individual galaxies tend towards the average. Thus, it is possible and useful to describe an average galactic spectra for galaxies with halo mass $M > 10^9\ \mathrm{M}_\odot$.

3. **Chapter 3.** *JWST* should be able to observe galaxies up to $z = 15$. While it is obvious that a new, more powerful telescope should do better than the current record of $z = 11.09$ with *HST*, we can conclusively state that *JWST* is capable of observing a high sky density in early Reionization.

4. **Chapter 4.** Population III galaxies will be difficult to confirm. Population III stars are the first to form in galaxies and thus usually exist in relatively small halos and within relatively small stellar clusters, making them dim. We find that the only scenarios that may lead to an observation are a merger between such a halo with a larger halo or a merger between two Population III galaxies. In either case, a generous exposure time would be needed.

5. **Chapter 4.** Population III galaxies show strong Ly-α and C IV emission lines. Due to the heating on the interstellar medium by massive stars and supernovae, higher ionization states are visible in the spectra than for comparably sized metal-enriched galaxies.

6. **Chapter 5.** Direct Collapse Black holes (DCBH) that induce star formation in primordial gas may also be a source of Lyman-Werner (LW) radiation. X-rays from the black hole are reprocessed into UV radiation in the supernova-heated gas. LW radiation plays a role in suppressing star formation and the formation of massive black holes. The possibility of a DCBH-induced LW flux is unexplored in prior literature.

7. **Chapter 5.** A Direct Collapse Black Hole is relatively easy to observe, but perhaps harder to find. The DCBH scenario examined in Chapter 5 gives excellent S/N ratios for the sort of exposure times that it would take to observe galaxies described in Chapters 3 or 4. However, over a dozen individual pointings with *JWST* are required to capture even a single example of a DCBH.

6.1 Future Work

These measures and results carry the caveat that Caius cannot currently simulate processes in the IGM, track changes in the abundance ratios of chemical species, or tackle the modeling complexities of active galactic nuclei (AGN).

For some studies, an intrinsic IGM modeling method may not be strictly necessary. Investigations of astrophysical questions like the rates of reionization, the impact of X-rays on the interstellar medium, and the dynamics driving the photo-evaporation of satellite galaxies would benefit from advances in radiative transfer techniques alone. Other studies may be better served by the existing body of IGM modeling resources and techniques available to scientists. Both these scenarios offer an opportunity for CAIUS to continue to produce scientifically-relevant results in its current form.

The benefit of adding an intrinsic IGM calculation to CAIUS is therefore two-fold. First, it lessens the modeling burden on scientists who would benefit from a database of more easily cross-referenced and representative synthetic spectra. This will broaden the scope and impact of any findings and facilitate interdisciplinary work. Second, it leverages the existing pipeline to better explore and constrain astrophysical processes such as the impact of high-energy sources like DCBHs, HMXBs, and AGN on clusters of galaxies.

Another important consideration is the chemical composition of the medium during Reionization. For example, observations of enhanced C IV emissions in the IGM at high redshift ($z > 5$) suggested super-solar abundances of carbon[e.g. 190]. This was attributed to both Population III[e.g. 191] and metal-poor Population II stars[e.g. 192] enriching the medium. Additionally, Chapter 4 showed that C IV emissions were a strong component of the CGM spectra in galaxies with young stars despite the assumption of solar abundances. Adding an abundance-tracking technique in conjunction with an IGM method to CAIUS will help investigate both the emission and absorption side of phenomena like these in situations where the assumption of solar abundances is no longer appropriate. Suggested future projects as shown in Figure 6.1 are:

1. **Calibration to Near-Field Objects** Isolated disk-galaxy simulations like those generated in the AGORA project[97] will be used to generate mock Milky

Way-like spectra and images. Depending on the availability of data, high-resolution observations from the *HST*, *JWST*, and synthetic spectra will be directly compared and used to calibrate the generation of representative synthetic observables. The intention is to run the AGORA initial conditions using ENZO for the initial analysis, but AGORA is itself a project to compare various hydrodynamic simulation codes. I will lead a group of representatives from each code to validate or inform their physical assumptions through comparisons with observations by running CAIUS on their galaxy simulations. To accommodate comparisons to observations, the cast of supported instrument measures in CAIUS will be expanded to include the modeling of grisms and integral field units during this phase. The pipeline will also be expanded to generally support smooth particle hydrodynamics (SPH) simulations using YT[128] as a data-collecting intermediary to allow different simulation techniques to be compared.

2. **Chemical Specie Tracking** Simulations such as the publicly available SPH EAGLE project[193] include chemical specie tracking. This will be used to model the evolution of spectra with respect to various phases of enrichment. Where prior work focused on individual snapshots of cosmological simulations, the development of a specie-dependent radiative transfer method will support investigations into redshift and environment-dependent observational measures. The focus in this phase will be on capturing or validating primary and secondary trends in the radiation field as galaxies grow, endure starbursts, and merge. The contributions to Lyman-Werner and ionizing radiation from diffuse sources may have a significant impact on galactic morphology and the rates of star formation, for example, but are customarily excluded from cosmological simulations due to their computational cost. Results will inform a model to reconcile these differences. For observers, results will advise on the relationship between various emission lines, astrophysical events, and the nature of the ISM

and star formation during galaxy assembly.

3. **IGM Modeling** TRIDENT[139] models absorption of spectra in the IGM within the YT ecosystem of simulation analysis tools. This will be used in conjunction with observations and cosmological simulations to further calibrate the generation of representative deep-field synthetic observations. Statistical measures of the half-light radius, luminosity function, and reionization rates will then be investigated using simulations like the $z = 8$ void volume of the ***Renaissance Simulations***[2, 112]. Results will aid the interpretation of low-resolution photometry and spectrometry from *JWST* and ***HST***. A large number of individual synthetic observations will be made publicly available during this phase to aid cross-referencing by observers. Additionally, synthetic observations and physical quantities will be used to train a machine-learning algorithm.

4. **AGN and Compact Objects** Prior studies of High Mass X-ray Binaries (HMXB) using the CAIUS pipeline only modeled their radiation in post-processing using a simple analytic model. The aforementioned EAGLE simulations include an intrinsic AGN feedback and a black hole accretion calculation. This will be combined with a more consistent calculation of the intrinsic spectra of compact objects and binaries to further expand the applicability of the pipeline and study observational markers in AGN-hosting galaxies. As AGN are more readily observed at higher redshift than quiescent galaxies, this study would benefit observers using a wider range of telescopes. Results will also help inform feedback models in future cosmological simulations. By leveraging results from Chapter 5 on the spectroscopic characteristics of a DCBH scenario, better compact object modeling will also be tuned to investigate the impact of high-energy sources on their host galaxies and study electromagnetic analogues to Laser Interferometer Space Antenna (LISA) targets.

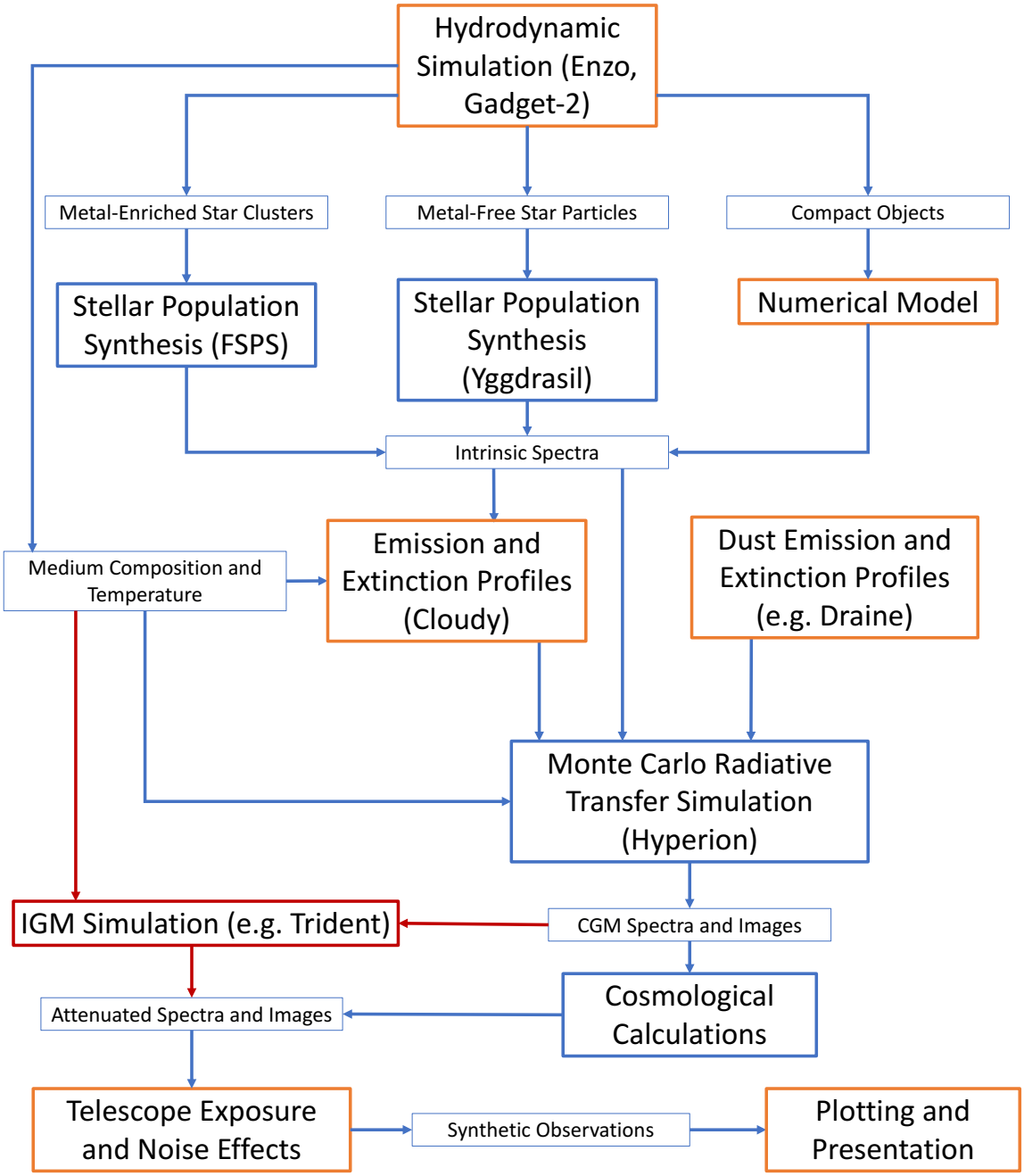

Figure 6.1: Proposed changes to CAIUS pipeline. Large font indicates a calculation and small font indicates an input. Blue pathways and boxes will remain as they exist in the current pipeline. Orange boxes will be overhauled and expanded. Red boxes and pathways are additions to the pipeline.

The radiative transfer techniques employed by CAIUS are more robust than methods currently in the literature. The proposed work will continue to uniquely position CAIUS to answer several novel astrophysical questions and generate predictions for *JWST* and future generations of space telescopes. However, the ultimate goal of this work will be to maximize scientific impact by building collaborations with observers and eventually opening up the use and development of the pipeline to the broader scientific community.

APPENDIX A
THEORY OF WORLD STRUCTURE

To motivate the construction of the continuity equation for radiative transfer in a cosmological context as well as the discussion of cosmological flux attenuation, we briefly derive the Hubble constant, H, from the Friedmann–Robertson–Walker (FRW) metric[18]

$$ds^2 = -c^2dt^2 + a(t)\left[\frac{dr^2}{1-kr^2} + r^2(d\theta^2 + \sin^2(\theta)d\phi^2)\right], \tag{A.1}$$

where $a(t)$ is the cosmological expansion factor and k depends on the curvature, and the Einstein [194] field equations

$$R_{\mu\nu} - \frac{1}{2}Rg_{\mu\nu} + \Lambda g_{\mu\nu} = \frac{8\pi G}{c^4}T_{\nu\mu}, \tag{A.2}$$

where $R_{\mu\nu}$ is the Ricci curvature tensor, $T_{\nu\mu}$ is the stress-energy tensor, $g_{\mu\nu}$ is the metric tensor, Λ is the cosmological constant, and the Ricci scalar curvature, R, is

$$R = \frac{6}{c^2a^2}(\ddot{a}a + \dot{a}^2 + kc^2). \tag{A.3}$$

The subscripted terms are symmetric four by four tensors, which produce ten equations. We see that $g_{00} = -c^2$ and $R_{00} = -3\ddot{a}/a$ from Equation A.1 and we know that $T_{00} = T^{00}(g_{00})^2 = \rho c^4$, where ρ is the matter-energy density of the Universe. Therefore, the time-time component of Equation A.2 is

$$-3\frac{\ddot{a}}{a} + \frac{3}{a^2}(\ddot{a}a + \dot{a}^2 + kc^2) - \Lambda c^2 = 8\pi G\rho, \tag{A.4}$$

which simplifies to the Friedmann [195] equation

$$\left(\frac{\dot{a}}{a}\right)^2 = \frac{8\pi G\rho}{3} + \frac{\Lambda c^2}{3} - \frac{kc^2}{a^2}. \tag{A.5}$$

We define the Hubble constant $H(a) = \dot{a}/a$, where the present-day value of the constant is written as $H_0 = \dot{a}_0/a_0$. We also note that the density has a matter component ρ_{M} and a radiation component ρ_{r} such that $\rho = \rho_{\mathrm{M}} + \rho_{\mathrm{r}}$. We define

$$\Omega_{\mathrm{M}} = \frac{8\pi G}{3H_0^2}\rho_{\mathrm{M}}, \Omega_{\mathrm{r}} = \frac{8\pi G}{3H_0^2}\rho_{\mathrm{r}}, \Omega_{\Lambda} = \frac{\Lambda c^2}{3H_0^2}, \Omega_{\mathrm{k}} = \frac{-kc^2}{a^2H_0^2}, \tag{A.6}$$

where Ω_{M}, Ω_{r}, Ω_{Λ}, and Ω_{k} are the matter, radiation, cosmological constant, and curvature density parameters respectively. The Hubble constant can thus be rewritten from Equation A.5 as

$$H^2 = H_0^2(\Omega_{\mathrm{M}} + \Omega_{\mathrm{r}} + \Omega_{\Lambda} + \Omega_{\mathrm{k}}). \tag{A.7}$$

Upon careful review of Equations A.6, we see that the only terms that change with time are ρ_{M}, ρ_{r}, and the scale factor a. We expect ρ_{M} to be inversely related to a^3 intuitively since each dimension of the volume is scaled. We expect ρ_{r} to be inversely related to a^4 since the number density of photons scales with $1/a^3$ energy of a photon scales with $1/a$. We also note that Ω_{Λ} is completely composed of constants and does not change. If we set the present-day scale factor to be unity ($a_0 = 1$) and employ the relationship $a = 1/(1+z)$, where z is the redshift, we finally obtain

$$H(z) = \frac{\dot{a}}{a} = H_0\sqrt{\Omega_{\mathrm{M},0}(1+z)^3 \ + \Omega_{\mathrm{r},0}(1+z)^4 + \Omega_{\Lambda,0} + \Omega_{\mathrm{k},0}(1+z)^2}, \tag{A.8}$$

in terms of the present day values of the density parameters $\Omega_{\mathrm{M},0}$, $\Omega_{\mathrm{r},0}$, $\Omega_{\Lambda,0}$, and $\Omega_{\mathrm{k},0}$, which necessarily sum to unity.

Cosmologists and astronomers often use redshift as a proxy for time, where a higher redshift refers to a time earlier in the evolution of the Universe. We repose

and integrate Equation A.8 to demonstrate the relationship between the two by first noting that $da/dt = aH(z) = H(z)/(1+z)$. We also see that

$$\frac{dz}{dt} = \frac{dz}{da}\frac{da}{dt} = -(1+z)^2\frac{H(z)}{1+z} = -(1+z)H(z). \tag{A.9}$$

Therefore, the elapsed time, Δt, between an initial redshift, z_1, and a final redshift, z_2, is

$$\Delta t = \int_{z_2}^{z_1} \frac{dz}{(1+z)H(z)}, \tag{A.10}$$

where $z = 0$ corresponds to the present and $z = \infty$ is the beginning of the Universe. Thus, the age of the Universe depends on the values of the present-day density parameters and Hubble constant as calculated in Equation 1.2.

BIBLIOGRAPHY

[1] W. Gliese and H. Jahreiß. Preliminary Version of the Third Catalogue of Nearby Stars. Technical report, 1991.

[2] B. W. O'Shea, J. H. Wise, H. Xu, and M. L. Norman. Probing the Ultraviolet Luminosity Function of the Earliest Galaxies with the Renaissance Simulations. Astrophys. J. Lett., 807:L12, July 2015. doi: 10.1088/2041-8205/807/1/L12.

[3] R. J. McLure, J. S. Dunlop, M. Cirasuolo, A. M. Koekemoer, E. Sabbi, D. P. Stark, T. A. Targett, and R. S. Ellis. Galaxies at z = 6-9 from the WFC3/IR imaging of the Hubble Ultra Deep Field. Mon. Not. R. Astron. Soc., 403:960–983, April 2010. doi: 10.1111/j.1365-2966.2009.16176.x.

[4] R. S. Ellis, R. J. McLure, J. S. Dunlop, B. E. Robertson, Y. Ono, M. A. Schenker, A. Koekemoer, R. A. A. Bowler, M. Ouchi, A. B. Rogers, E. Curtis-Lake, E. Schneider, S. Charlot, D. P. Stark, S. R. Furlanetto, and M. Cirasuolo. The Abundance of Star-forming Galaxies in the Redshift Range 8.5-12: New Results from the 2012 Hubble Ultra Deep Field Campaign. Astrophys. J. Lett., 763:L7, January 2013. doi: 10.1088/2041-8205/763/1/L7.

[5] J. M. Lotz, A. Koekemoer, D. Coe, N. Grogin, P. Capak, J. Mack, J. Anderson, R. Avila, E. A. Barker, D. Borncamp, G. Brammer, M. Durbin, H. Gunning, B. Hilbert, H. Jenkner, H. Khandrika, Z. Levay, R. A. Lucas, J. MacKenty, S. Ogaz, B. Porterfield, N. Reid, M. Robberto, P. Royle, L. J. Smith, L. J. Storrie-Lombardi, B. Sunnquist, J. Surace, D. C. Taylor, R. Williams, J. Bullock, M. Dickinson, S. Finkelstein, P. Natarajan, J. Richard, B. Robertson, J. Tumlinson, A. Zitrin, K. Flanagan, K. Sembach, B. T. Soifer, and M. Mountain. The Frontier Fields: Survey Design and Initial Results. Astrophys. J., 837:97, March 2017. doi: 10.3847/1538-4357/837/1/97.

[6] Y. Feng, T. Di-Matteo, R. A. Croft, S. Bird, N. Battaglia, and S. Wilkins. The BlueTides simulation: first galaxies and reionization. Mon. Not. R. Astron. Soc., 455: 2778–2791, January 2016. doi: 10.1093/mnras/stv2484.

[7] J.-P. Paardekooper, S. Khochfar, and C. Dalla Vecchia. The First Billion Years project: the escape fraction of ionizing photons in the epoch of reionization. Mon. Not. R. Astron. Soc., 451:2544–2563, August 2015. doi: 10.1093/mnras/stv1114.

[8] J. P. Gardner, J. C. Mather, M. Clampin, R. Doyon, M. A. Greenhouse, H. B. Hammel, J. B. Hutchings, P. Jakobsen, S. J. Lilly, K. S. Long, J. I. Lunine, M. J. McCaughrean, M. Mountain, J. Nella, G. H. Rieke, M. J. Rieke, H.-W. Rix, E. P. Smith, G. Sonneborn, M. Stiavelli, H. S. Stockman, R. A. Windhorst, and G. S. Wright. The James Webb Space Telescope. Space Science Reviews, 123:485–606, April 2006. doi: 10.1007/s11214-006-8315-7.

[9] K. S. S. Barrow, J. H. Wise, A. Aykutalp, B. W. O'Shea, M. L. Norman, and H. Xu. First light - II. Emission line extinction, population III stars, and X-ray binaries. Mon. Not. R. Astron. Soc., 474:2617–2634, February 2018. doi: 10.1093/mnras/stx2973.

[10] A. A. Penzias and R. W. Wilson. A Measurement of Excess Antenna Temperature at 4080 Mc/s. Astrophys. J., 142:419–421, July 1965. doi: 10.1086/148307.

[11] R. H. Dicke, P. J. E. Peebles, P. G. Roll, and D. T. Wilkinson. Cosmic Black-Body Radiation. Astrophys. J., 142:414–419, July 1965. doi: 10.1086/148306.

[12] P. J. E. Peebles. Recombination of the Primeval Plasma. Astrophys. J., 153:1, July 1968. doi: 10.1086/149628.

[13] J. M. Lamarre, J. L. Puget, F. Bouchet, P. A. R. Ade, A. Benoit, J. P. Bernard, J. Bock, P. De Bernardis, J. Charra, F. Couchot, J. Delabrouille, G. Efstathiou, M. Giard, G. Guyot, A. Lange, B. Maffei, A. Murphy, F. Pajot, M. Piat, I. Ristorcelli, D. Santos, R. Sudiwala, J. F. Sygnet, J. P. Torre, V. Yurchenko, and D. Yvon. The Planck High Frequency Instrument, a third generation CMB experiment, and a full sky submillimeter survey. New Astro. Rev., 47:1017–1024, December 2003. doi: 10.1016/j.newar.2003.09.006.

[14] Planck Collaboration, P. A. R. Ade, N. Aghanim, M. Arnaud, M. Ashdown, J. Aumont, C. Baccigalupi, A. J. Banday, R. B. Barreiro, J. G. Bartlett, and et al. Planck 2015 results. XIII. Cosmological parameters. Astron. Astrophys., 594:A13, September 2016. doi: 10.1051/0004-6361/201525830.

[15] A. G. Riess, L. M. Macri, S. L. Hoffmann, D. Scolnic, S. Casertano, A. V. Filippenko, B. E. Tucker, M. J. Reid, D. O. Jones, J. M. Silverman, R. Chornock, P. Challis, W. Yuan, P. J. Brown, and R. J. Foley. A 2.4% Determination of the Local Value of the Hubble Constant. Astrophys. J., 826:56, July 2016. doi: 10.3847/0004-637X/826/1/56.

[16] J. L. Bernal, L. Verde, and A. G. Riess. The trouble with H_0. Jour. of Cosmo. and Astropar. Physics, 10:019, October 2016. doi: 10.1088/1475-7516/2016/10/019.

[17] P. A. Oesch, G. Brammer, P. G. van Dokkum, G. D. Illingworth, R. J. Bouwens, I. Labbé, M. Franx, I. Momcheva, M. L. N. Ashby, G. G. Fazio, V. Gonzalez, B. Holden, D. Magee, R. E. Skelton, R. Smit, L. R. Spitler, M. Trenti, and S. P. Willner. A Remarkably Luminous Galaxy at z=11.1 Measured with Hubble Space Telescope Grism Spectroscopy. Astrophys. J., 819:129, March 2016. doi: 10.3847/0004-637X/819/2/129.

[18] Arthur Geoffrey Walker. On milne's theory of world-structure. Proceedings of the London Mathematical Society, 2:90–127, 1937.

[19] IMH Etherington. Lx. on the definition of distance in general relativity. The London, Edinburgh, and Dublin Philosophical Magazine and Journal of Science, 15:761–773, 1933.

[20] D. W. Hogg, I. K. Baldry, M. R. Blanton, and D. J. Eisenstein. The K correction. ArXiv Astrophysics e-prints, October 2002.

[21] George Biddell Airy. On the diffraction of an object-glass with circular aperture. Transactions of the Cambridge Philosophical Society, 5:283, 1835.

[22] J. Anderson. Empirical Models for the WFC3/IR PSF. Technical report, March 2016.

[23] Simon Denis Poisson. Recherches sur la probabilite des jugements en matiere criminelle et en matiere civile, precedees des regles generales du calcul des probabilites. Bachelier, 1837.

[24] J. F. Navarro, C. S. Frenk, and S. D. M. White. The Structure of Cold Dark Matter Halos. Astrophys. J., 462:563, May 1996. doi: 10.1086/177173.

[25] A. Klypin, H. Zhao, and R. S. Somerville. ΛCDM-based Models for the Milky Way and M31. I. Dynamical Models. Astrophys. J., 573:597–613, July 2002. doi: 10.1086/340656.

[26] L. M. Widrow, K. M. Perrett, and S. H. Suyu. Disk-Bulge-Halo Models for the Andromeda Galaxy. Astrophys. J., 588:311–325, May 2003. doi: 10.1086/368410.

[27] S. F. Shandarin and Y. B. Zeldovich. The large-scale structure of the universe: Turbulence, intermittency, structures in a self-gravitating medium. Reviews of Modern Physics, 61:185–220, April 1989. doi: 10.1103/RevModPhys.61.185.

[28] T. Abel, G. L. Bryan, and M. L. Norman. The Formation of the First Star in the Universe. Science, 295:93–98, January 2002. doi: 10.1126/science.295.5552.93.

[29] E. Visbal, R. Barkana, A. Fialkov, D. Tseliakhovich, and C. M. Hirata. The signature of the first stars in atomic hydrogen at redshift 20. Nat., 487:70–73, July 2012. doi: 10.1038/nature11177.

[30] Judd D. Bowman, Alan E. E. Rogers, Raul A. Monsalve, Thomas J. Mozdzen, and Nivedita Mahesh. An absorption profile centred at 78 megahertz in the sky-averaged spectrum. Nature, 555:67 EP –, 02 2018. URL `http://dx.doi.org/10.1038/nature25792`.

[31] N. Kashikawa, K. Shimasaku, M. A. Malkan, M. Doi, Y. Matsuda, M. Ouchi, Y. Taniguchi, C. Ly, T. Nagao, M. Iye, K. Motohara, T. Murayama, K. Murozono, K. Nariai, K. Ohta, S. Okamura, T. Sasaki, Y. Shioya, and M. Umemura. The End of the Reionization Epoch Probed by Lyα Emitters at z = 6.5 in the Subaru Deep Field. Astrophys. J., 648:7–22, September 2006. doi: 10.1086/504966.

[32] D. Koh and J. H. Wise. Extending semi-numeric reionization models to the first stars and galaxies. Mon. Not. R. Astron. Soc., 474:3817–3824, March 2018. doi: 10.1093/mnras/stx3018.

[33] G. L. Bryan, M. L. Norman, B. W. O'Shea, T. Abel, J. H. Wise, M. J. Turk, D. R. Reynolds, D. C. Collins, P. Wang, S. W. Skillman, B. Smith, R. P. Harkness, J. Bordner, J.-h. Kim, M. Kuhlen, H. Xu, N. Goldbaum, C. Hummels, A. G. Kritsuk,

E. Tasker, S. Skory, C. M. Simpson, O. Hahn, J. S. Oishi, G. C. So, F. Zhao, R. Cen, Y. Li, and Enzo Collaboration. ENZO: An Adaptive Mesh Refinement Code for Astrophysics. Astrophys. J. Suppl., 211:19, April 2014. doi: 10.1088/0067-0049/211/2/19.

[34] Eugene Paul Wigner. Group theory and its application to the quantum mechanics of atomic spectra. American Journal of Physics, 1959.

[35] Robert C Hilborn. Einstein coefficients, cross sections, f values, dipole moments, and all that. American Journal of Physics, 50(11):982–986, 1982.

[36] Ludwig Boltzmann. On the relationship between the second fundamental theorem of the mechanical theory of heat and probability calculations regarding the conditions for thermal equilibrium. Sitzungberichte der Kaiserlichen Akademie der Wissenschaften, pages 373–435, 1877.

[37] James Clerk Maxwell. V. illustrations of the dynamical theory of gases.—part i. on the motions and collisions of perfectly elastic spheres. The London, Edinburgh, and Dublin Philosophical Magazine and Journal of Science, 19(124):19–32, 1860.

[38] JC Maxwell. On the process of diffusion of two or more kinds of moving particles among one another. Philosophical Magazine, 20:21–38, 1860.

[39] Werner Heisenberg. Über den anschaulichen inhalt der quantentheoretischen kinematik und mechanik. In Original Scientific Papers Wissenschaftliche Originalarbeiten, pages 478–504. Springer, 1927.

[40] Megh Nad Saha. Liii. ionization in the solar chromosphere. The London, Edinburgh, and Dublin Philosophical Magazine and Journal of Science, 40(238):472–488, 1920.

[41] Megh Nad Saha. On a physical theory of stellar spectra. Proceedings of the Royal Society of London. Series A, Containing Papers of a Mathematical and Physical Character, 99(697):135–153, 1921.

[42] Douglas R Hartree. The wave mechanics of an atom with a non-coulomb central field. part i. theory and methods. In Mathematical Proceedings of the Cambridge Philosophical Society, volume 24, pages 89–110. Cambridge University Press, 1928.

[43] Vladimir Fock. Näherungsmethode zur lösung des quantenmechanischen mehrkörperproblems. Zeitschrift für Physik A Hadrons and Nuclei, 61:126–148, 1930.

[44] Hendrik A Kramers. Xciii. on the theory of x-ray absorption and of the continuous x-ray spectrum. The London, Edinburgh, and Dublin Philosophical Magazine and Journal of Science, 46(275):836–871, 1923.

[45] Oskar Klein and Yoshio Nishina. Über die streuung von strahlung durch freie elektronen nach der neuen relativistischen quantendynamik von dirac. Zeitschrift für Physik, 52:853–868, 1929.

[46] Arthur H Compton. A quantum theory of the scattering of x-rays by light elements. Physical review, 21(5):483, 1923.

[47] G Cillié. The hydrogen emission in gaseous nebulae. Monthly Notices of the Royal Astronomical Society, 92:820, 1932.

[48] JJ Thomson. Xxx. on a theory of the structure of the electric field and its application to röntgen radiation and to light. The London, Edinburgh, and Dublin Philosophical Magazine and Journal of Science, 19:301–313, 1910.

[49] T. Peters, S. N. Longmore, and C. P. Dullemond. Understanding hydrogen recombination line observations with ALMA and EVLA. Mon. Not. R. Astron. Soc., 425: 2352–2368, September 2012. doi: 10.1111/j.1365-2966.2012.21676.x.

[50] Joseph Larmor. Lxiii. on the theory of the magnetic influence on spectra; and on the radiation from moving ions. The London, Edinburgh, and Dublin Philosophical Magazine and Journal of Science, 44(271):503–512, 1897.

[51] Max Planck. The theory of heat radiation. Entropie, 144(190):164, 1900.

[52] Gustav Kirchhoff. I. on the relation between the radiating and absorbing powers of different bodies for light and heat. The London, Edinburgh, and Dublin Philosophical Magazine and Journal of Science, 20(130):1–21, 1860.

[53] W. W. Morgan, P. C. Keenan, and E. Kellman. An atlas of stellar spectra, with an outline of spectral classification. 1943.

[54] Ejnar Hertzsprung. Über die verwendung photographischer effektiver wellenlaengen zur bestimmung von farbenäquivalenten. Publikationen des Astrophysikalischen Observatoriums zu Potsdam, 63, 1911.

[55] Henry Norris Russell. Relations between the spectra and other characteristics of the stars. Proceedings of the American Philosophical Society, 51:569–579, 1912.

[56] C. Leitherer, D. Schaerer, J. D. Goldader, R. M. G. Delgado, C. Robert, D. F. Kune, D. F. de Mello, D. Devost, and T. M. Heckman. Starburst99: Synthesis Models for Galaxies with Active Star Formation. Astrophys. J. Suppl., 123:3–40, July 1999. doi: 10.1086/313233.

[57] G. Bruzual and S. Charlot. Stellar population synthesis at the resolution of 2003. Mon. Not. R. Astron. Soc., 344:1000–1028, October 2003. doi: 10.1046/j.1365-8711.2003.06897.x.

[58] J. J. Eldridge, E. R. Stanway, L. Xiao, L. A. S. McClelland, G. Taylor, M. Ng, S. M. L. Greis, and J. C. Bray. Binary Population and Spectral Synthesis Version 2.1: Construction, Observational Verification, and New Results. Pub. Astro. Soc. Aus., 34:e058, November 2017. doi: 10.1017/pasa.2017.51.

[59] C. Conroy and J. E. Gunn. The Propagation of Uncertainties in Stellar Population Synthesis Modeling. III. Model Calibration, Comparison, and Evaluation. Astrophys. J., 712:833–857, April 2010. doi: 10.1088/0004-637X/712/2/833.

[60] E. Zackrisson, C.-E. Rydberg, D. Schaerer, G. Östlin, and M. Tuli. The Spectral Evolution of the First Galaxies. I. James Webb Space Telescope Detection Limits and Color Criteria for Population III Galaxies. Astrophys. J., 740:13, October 2011. doi: 10.1088/0004-637X/740/1/13.

[61] A. S. Eddington. The Internal Constitution of the Stars. 1926.

[62] N. I. Shakura and R. A. Sunyaev. Black holes in binary systems. Observational appearance. Astron. Astrophys., 24:337–355, 1973.

[63] H. Bondi and F. Hoyle. On the mechanism of accretion by stars. Mon. Not. R. Astron. Soc., 104:273, 1944. doi: 10.1093/mnras/104.5.273.

[64] H. Bondi. On spherically symmetrical accretion. Mon. Not. R. Astron. Soc., 112:195, 1952. doi: 10.1093/mnras/112.2.195.

[65] E. Shima, T. Matsuda, H. Takeda, and K. Sawada. Hydrodynamic calculations of axisymmetric accretion flow. Mon. Not. R. Astron. Soc., 217:367–386, November 1985. doi: 10.1093/mnras/217.2.367.

[66] D. Lynden-Bell. Galactic Nuclei as Collapsed Old Quasars. Nat., 223:690–694, August 1969. doi: 10.1038/223690a0.

[67] Karl Schwarzschild. Über das gravitationsfeld einer kugel aus inkompressibler flüssigkeit nach der einsteinschen theorie. In Sitzungsberichte der Königlich Preussischen Akademie der Wissenschaften zu Berlin, Phys.-Math. Klasse, 424-434 (1916), 1916.

[68] K. Ebisawa, P. Życki, A. Kubota, T. Mizuno, and K.-y. Watarai. Accretion Disk Spectra of Ultraluminous X-Ray Sources in Nearby Spiral Galaxies and Galactic Superluminal Jet Sources. Astrophys. J., 597:780–797, November 2003. doi: 10.1086/378586.

[69] A. A. Zdziarski. Power-law X-ray and gamma-ray emission from relativistic thermal plasmas. Astrophys. J., 289:514–525, February 1985. doi: 10.1086/162912.

[70] L. Titarchuk and T. Zannias. The Extended Power Law as an Intrinsic Signature for a Black Hole. Astrophys. J., 493:863–872, January 1998. doi: 10.1086/305157.

[71] N. Y. Gnedin and J. P. Ostriker. Reionization of the Universe and the Early Production of Metals. Astrophys. J., 486:581–598, September 1997. doi: 10.1086/304548.

[72] D. Mihalas and B. W. Mihalas. Foundations of radiation hydrodynamics. 1984.

[73] Q. Ge and J. H. Wise. On the effect of Lyman α trapping during the initial collapse of massive black hole seeds. Mon. Not. R. Astron. Soc., 472:2773–2786, December 2017. doi: 10.1093/mnras/stx2074.

[74] A. Smith, B. T.-H. Tsang, V. Bromm, and M. Milosavljevic. Discrete diffusion Lyman-alpha radiative transfer. ArXiv e-prints, September 2017.

[75] T. Abel and B. D. Wandelt. Adaptive ray tracing for radiative transfer around point sources. Mon. Not. R. Astron. Soc., 330:L53–L56, March 2002. doi: 10.1046/j.1365-8711.2002.05206.x.

[76] K. M. Górski, E. Hivon, A. J. Banday, B. D. Wandelt, F. K. Hansen, M. Reinecke, and M. Bartelmann. HEALPix: A Framework for High-Resolution Discretization and Fast Analysis of Data Distributed on the Sphere. Astrophys. J., 622:759–771, April 2005. doi: 10.1086/427976.

[77] J. H. Wise and T. Abel. ENZO+MORAY: radiation hydrodynamics adaptive mesh refinement simulations with adaptive ray tracing. Mon. Not. R. Astron. Soc., 414: 3458–3491, July 2011. doi: 10.1111/j.1365-2966.2011.18646.x.

[78] L. B. Lucy. Computing radiative equilibria with Monte Carlo techniques. Astron. Astrophys., 344:282–288, April 1999.

[79] T. P. Robitaille. HYPERION: an open-source parallelized three-dimensional dust continuum radiative transfer code. Astron. Astrophys., 536:A79, December 2011. doi: 10.1051/0004-6361/201117150.

[80] S. V. W. Beckwith, M. Stiavelli, A. M. Koekemoer, J. A. R. Caldwell, H. C. Ferguson, R. Hook, R. A. Lucas, L. E. Bergeron, M. Corbin, S. Jogee, N. Panagia, M. Robberto, P. Royle, R. S. Somerville, and M. Sosey. The Hubble Ultra Deep Field. Astronomical. J., 132:1729–1755, November 2006. doi: 10.1086/507302.

[81] C. C. Steidel, M. Giavalisco, M. Pettini, M. Dickinson, and K. L. Adelberger. Spectroscopic Confirmation of a Population of Normal Star-forming Galaxies at Redshifts Z > 3. Astrophys. J. Lett., 462:L17, May 1996. doi: 10.1086/310029.

[82] S. Malhotra, J. E. Rhoads, N. Pirzkal, Z. Haiman, C. Xu, E. Daddi, H. Yan, L. E. Bergeron, J. Wang, H. C. Ferguson, C. Gronwall, A. Koekemoer, M. Kuemmel, L. A. Moustakas, N. Panagia, A. Pasquali, M. Stiavelli, J. Walsh, R. A. Windhorst, and S. di Serego Alighieri. An Overdensity of Galaxies at z = 5.9 +/- 0.2 in the Hubble Ultra Deep Field Confirmed Using the ACS Grism. Astrophys. J., 626:666–679, June 2005. doi: 10.1086/430047.

[83] R. J. Bouwens, G. D. Illingworth, M. Franx, and H. Ford. UV Luminosity Functions at z˜4, 5, and 6 from the Hubble Ultra Deep Field and Other Deep Hubble Space Telescope ACS Fields: Evolution and Star Formation History. Astrophys. J., 670: 928–958, December 2007. doi: 10.1086/521811.

[84] P. A. Oesch, M. Stiavelli, C. M. Carollo, L. E. Bergeron, A. M. Koekemoer, R. A. Lucas, C. M. Pavlovsky, M. Trenti, S. J. Lilly, S. V. W. Beckwith, T. Dahlen, H. C. Ferguson, J. P. Gardner, C. Lacey, B. Mobasher, N. Panagia, and H.-W. Rix. The UDF05 Follow-up of the Hubble Ultra Deep Field. I. The Faint-End Slope of the Lyman Break Galaxy Population at z ˜ 5. Astrophys. J., 671:1212–1226, December 2007. doi: 10.1086/522423.

[85] A. M. Koekemoer, R. S. Ellis, R. J. McLure, J. S. Dunlop, B. E. Robertson, Y. Ono, M. A. Schenker, M. Ouchi, R. A. A. Bowler, A. B. Rogers, E. Curtis-Lake, E. Schneider, S. Charlot, D. P. Stark, S. R. Furlanetto, M. Cirasuolo, V. Wild, and T. Targett. The 2012 Hubble Ultra Deep Field (UDF12): Observational Overview. Astrophys. J. Suppl., 209:3, November 2013. doi: 10.1088/0067-0049/209/1/3.

[86] R. J. Bouwens, L. Bradley, A. Zitrin, D. Coe, M. Franx, W. Zheng, R. Smit, O. Host, M. Postman, L. Moustakas, I. Labbé, M. Carrasco, A. Molino, M. Donahue, D. D. Kelson, M. Meneghetti, N. Benítez, D. Lemze, K. Umetsu, T. Broadhurst, J. Moustakas, P. Rosati, S. Jouvel, M. Bartelmann, H. Ford, G. Graves, C. Grillo, L. Infante, Y. Jimenez-Teja, O. Lahav, D. Maoz, E. Medezinski, P. Melchior, J. Merten, M. Nonino, S. Ogaz, and S. Seitz. A Census of Star-forming Galaxies in the Z ˜ 9-10 Universe based on HST+Spitzer Observations over 19 Clash Clusters: Three Candidate Z ˜ 9-10 Galaxies and Improved Constraints on the Star Formation Rate Density at Z ˜ 9.2. Astrophys. J., 795:126, November 2014. doi: 10.1088/0004-637X/795/2/126.

[87] S. L. Finkelstein. Observational Searches for Star-Forming Galaxies at z > 6. Pub. Astro. Soc. Aus., 33:e037, August 2016. doi: 10.1017/pasa.2016.26.

[88] R. A. A. Bowler, J. S. Dunlop, R. J. McLure, H. J. McCracken, B. Milvang-Jensen, H. Furusawa, Y. Taniguchi, O. Le Fèvre, J. P. U. Fynbo, M. J. Jarvis, and B. Häußler. The galaxy luminosity function at z 6 and evidence for rapid evolution in the bright end from z 7 to 5. Mon. Not. R. Astron. Soc., 452:1817–1840, September 2015. doi: 10.1093/mnras/stv1403.

[89] G. O. Abell, H. G. Corwin, Jr., and R. P. Olowin. A catalog of rich clusters of galaxies. Astrophys. J. Suppl., 70:1–138, May 1989. doi: 10.1086/191333.

[90] H. Ebeling, A. C. Edge, and J. P. Henry. MACS: A Quest for the Most Massive Galaxy Clusters in the Universe. Astrophys. J., 553:668–676, June 2001. doi: 10.1086/320958.

[91] V. Springel. E pur si muove: Galilean-invariant cosmological hydrodynamical simulations on a moving mesh. Mon. Not. R. Astron. Soc., 401:791–851, January 2010. doi: 10.1111/j.1365-2966.2009.15715.x.

[92] P. F. Hopkins. A new class of accurate, mesh-free hydrodynamic simulation methods. Mon. Not. R. Astron. Soc., 450:53–110, June 2015. doi: 10.1093/mnras/stv195.

[93] V. Springel. The cosmological simulation code GADGET-2. Mon. Not. R. Astron. Soc., 364:1105–1134, December 2005. doi: 10.1111/j.1365-2966.2005.09655.x.

[94] J. W. Wadsley, J. Stadel, and T. Quinn. Gasoline: a flexible, parallel implementation of TreeSPH. New Astron., 9:137–158, February 2004. doi: 10.1016/j.newast.2003.08.004.

[95] R. Teyssier. Cosmological hydrodynamics with adaptive mesh refinement. A new high resolution code called RAMSES. Astron. Astrophys., 385:337–364, April 2002. doi: 10.1051/0004-6361:20011817.

[96] B. W. O'Shea, K. Nagamine, V. Springel, L. Hernquist, and M. L. Norman. Comparing AMR and SPH Cosmological Simulations. I. Dark Matter and Adiabatic Simulations. Astrophys. J. Suppl., 160:1–27, September 2005. doi: 10.1086/432645.

[97] J.-h. Kim, T. Abel, O. Agertz, G. L. Bryan, D. Ceverino, C. Christensen, C. Conroy, A. Dekel, N. Y. Gnedin, N. J. Goldbaum, J. Guedes, O. Hahn, A. Hobbs, P. F. Hopkins, C. B. Hummels, F. Iannuzzi, D. Keres, A. Klypin, A. V. Kravtsov, M. R.

Krumholz, M. Kuhlen, S. N. Leitner, P. Madau, L. Mayer, C. E. Moody, K. Nagamine, M. L. Norman, J. Onorbe, B. W. O'Shea, A. Pillepich, J. R. Primack, T. Quinn, J. I. Read, B. E. Robertson, M. Rocha, D. H. Rudd, S. Shen, B. D. Smith, A. S. Szalay, R. Teyssier, R. Thompson, K. Todoroki, M. J. Turk, J. W. Wadsley, J. H. Wise, A. Zolotov, and t. AGORA Collaboration29. The AGORA High-resolution Galaxy Simulations Comparison Project. Astrophys. J. Suppl., 210:14, January 2014. doi: 10.1088/0067-0049/210/1/14.

[98] J.-h. Kim, O. Agertz, R. Teyssier, M. J. Butler, D. Ceverino, J.-H. Choi, R. Feldmann, B. W. Keller, A. Lupi, T. Quinn, Y. Revaz, S. Wallace, N. Y. Gnedin, S. N. Leitner, S. Shen, B. D. Smith, R. Thompson, M. J. Turk, T. Abel, K. S. Arraki, S. M. Benincasa, S. Chakrabarti, C. DeGraf, A. Dekel, N. J. Goldbaum, P. F. Hopkins, C. B. Hummels, A. Klypin, H. Li, P. Madau, N. Mandelker, L. Mayer, K. Nagamine, S. Nickerson, B. W. O'Shea, J. R. Primack, S. Roca-Fàbrega, V. Semenov, I. Shimizu, C. M. Simpson, K. Todoroki, J. W. Wadsley, J. H. Wise, and AGORA Collaboration. The AGORA High-resolution Galaxy Simulations Comparison Project. II. Isolated Disk Test. Astrophys. J., 833:202, December 2016. doi: 10.3847/1538-4357/833/2/202.

[99] H. Xu, M. L. Norman, B. W. O'Shea, and J. H. Wise. Late Pop III Star Formation During the Epoch of Reionization: Results from the Renaissance Simulations. Astrophys. J., 823:140, June 2016. doi: 10.3847/0004-637X/823/2/140.

[100] A. H. Pawlik, A. Rahmati, J. Schaye, M. Jeon, and C. Dalla Vecchia. The Aurora radiation-hydrodynamical simulations of reionization: calibration and first results. Mon. Not. R. Astron. Soc., 466:960–973, April 2017. doi: 10.1093/mnras/stw2869.

[101] H. Katz, T. Kimm, D. Sijacki, and M. Haehnelt. Interpreting ALMA Observations of the ISM During the Epoch of Reionisation. ArXiv e-prints, December 2016.

[102] S. L. Finkelstein, R. E. Ryan, Jr., C. Papovich, M. Dickinson, M. Song, R. S. Somerville, H. C. Ferguson, B. Salmon, M. Giavalisco, A. M. Koekemoer, M. L. N. Ashby, P. Behroozi, M. Castellano, J. S. Dunlop, S. M. Faber, G. G. Fazio, A. Fontana, N. A. Grogin, N. Hathi, J. Jaacks, D. D. Kocevski, R. Livermore, R. J. McLure, E. Merlin, B. Mobasher, J. A. Newman, M. Rafelski, V. Tilvi, and S. P. Willner. The Evolution of the Galaxy Rest-frame Ultraviolet Luminosity Function over the First Two Billion Years. Astrophys. J., 810:71, September 2015. doi: 10.1088/0004-637X/810/1/71.

[103] H. Atek, J. Richard, M. Jauzac, J.-P. Kneib, P. Natarajan, M. Limousin, D. Schaerer, E. Jullo, H. Ebeling, E. Egami, and B. Clement. Are Ultra-faint Galaxies at z = 6-8 Responsible for Cosmic Reionization? Combined Constraints from the Hubble Frontier Fields Clusters and Parallels. Astrophys. J., 814:69, November 2015. doi: 10.1088/0004-637X/814/1/69.

[104] R. C. Livermore, S. L. Finkelstein, and J. M. Lotz. Directly Observing the Galaxies Likely Responsible for Reionization. Astrophys. J., 835:113, February 2017. doi: 10.3847/1538-4357/835/2/113.

[105] R. J. Bouwens, P. A. Oesch, G. D. Illingworth, R. S. Ellis, and M. Stefanon. The z 6 Luminosity Function Fainter than -15 mag from the Hubble Frontier Fields:

The Impact of Magnification Uncertainties. Astrophys. J., 843:129, July 2017. doi: 10.3847/1538-4357/aa70a4.

[106] D. Sobral, J. Matthee, B. Darvish, D. Schaerer, B. Mobasher, H. J. A. Röttgering, S. Santos, and S. Hemmati. Evidence for PopIII-like Stellar Populations in the Most Luminous Lyman-α Emitters at the Epoch of Reionization: Spectroscopic Confirmation. Astrophys. J., 808:139, August 2015. doi: 10.1088/0004-637X/808/2/139.

[107] A. Pallottini, A. Ferrara, F. Pacucci, S. Gallerani, S. Salvadori, R. Schneider, D. Schaerer, D. Sobral, and J. Matthee. The brightest Ly α emitter: Pop III or black hole? Mon. Not. R. Astron. Soc., 453:2465–2470, November 2015. doi: 10.1093/mnras/stv1795.

[108] A. Smith, V. Bromm, and A. Loeb. Evidence for a direct collapse black hole in the Lyman α source CR7. Mon. Not. R. Astron. Soc., 460:3143–3151, August 2016. doi: 10.1093/mnras/stw1129.

[109] M. Dijkstra, M. Gronke, and D. Sobral. Lyα Signatures from Direct Collapse Black Holes. Astrophys. J., 823:74, June 2016. doi: 10.3847/0004-637X/823/2/74.

[110] B. Agarwal, J. L. Johnson, E. Zackrisson, I. Labbe, F. C. van den Bosch, P. Natarajan, and S. Khochfar. Detecting direct collapse black holes: making the case for CR7. Mon. Not. R. Astron. Soc., 460:4003–4010, August 2016. doi: 10.1093/mnras/stw1173.

[111] R. A. A. Bowler, R. J. McLure, J. S. Dunlop, D. J. McLeod, E. R. Stanway, J. J. Eldridge, and M. J. Jarvis. No evidence for Population III stars or a Direct Collapse Black Hole in the z = 6.6 Lyman-α emitter 'CR7'. Mon. Not. R. Astron. Soc., 469:448–458, July 2017. doi: 10.1093/mnras/stx839.

[112] H. Xu, J. H. Wise, M. L. Norman, K. Ahn, and B. W. O'Shea. Galaxy Properties and UV Escape Fractions during the Epoch of Reionization: Results from the Renaissance Simulations. Astrophys. J., 833:84, December 2016. doi: 10.3847/1538-4357/833/1/84.

[113] C. J. Willott, C. L. Carilli, J. Wagg, and R. Wang. Star Formation and the Interstellar Medium in z > 6 UV-luminous Lyman-break Galaxies. Astrophys. J., 807:180, July 2015. doi: 10.1088/0004-637X/807/2/180.

[114] M. Aravena, R. Decarli, F. Walter, R. Bouwens, P. A. Oesch, C. L. Carilli, F. E. Bauer, E. Da Cunha, E. Daddi, J. Gónzalez-López, R. J. Ivison, D. A. Riechers, I. Smail, A. M. Swinbank, A. Weiss, T. Anguita, R. Bacon, E. Bell, F. Bertoldi, P. Cortes, P. Cox, J. Hodge, E. Ibar, H. Inami, L. Infante, A. Karim, B. Magnelli, K. Ota, G. Popping, P. van der Werf, J. Wagg, and Y. Fudamoto. The ALMA Spectroscopic Survey in the Hubble Ultra Deep Field: Search for [CII] Line and Dust Emission in 6. Astrophys. J., 833:71, December 2016. doi: 10.3847/1538-4357/833/1/71.

[115] D. Larson, J. Dunkley, G. Hinshaw, E. Komatsu, M. R. Nolta, C. L. Bennett, B. Gold, M. Halpern, R. S. Hill, N. Jarosik, A. Kogut, M. Limon, S. S. Meyer, N. Odegard, L. Page, K. M. Smith, D. N. Spergel, G. S. Tucker, J. L. Weiland, E. Wollack, and

E. L. Wright. Seven-year Wilkinson Microwave Anisotropy Probe (WMAP) Observations: Power Spectra and WMAP-derived Parameters. Astrophys. J. Suppl., 192:16, February 2011. doi: 10.1088/0067-0049/192/2/16.

[116] H. Xu, J. H. Wise, and M. L. Norman. Population III Stars and Remnants in High-redshift Galaxies. Astrophys. J., 773:83, August 2013. doi: 10.1088/0004-637X/773/2/83.

[117] T. Abel, J. H. Wise, and G. L. Bryan. The H II Region of a Primordial Star. Astrophys. J. Lett., 659:L87–L90, April 2007. doi: 10.1086/516820.

[118] J. H. Wise and R. Cen. Ionizing Photon Escape Fractions From High-Redshift Dwarf Galaxies. Astrophys. J., 693:984–999, March 2009. doi: 10.1088/0004-637X/693/1/984.

[119] J. H. Wise, T. Abel, M. J. Turk, M. L. Norman, and B. D. Smith. The birth of a galaxy - II. The role of radiation pressure. Mon. Not. R. Astron. Soc., 427:311–326, November 2012. doi: 10.1111/j.1365-2966.2012.21809.x.

[120] D. Schaerer. On the properties of massive Population III stars and metal-free stellar populations. Astron. Astrophys., 382:28–42, January 2002. doi: 10.1051/0004-6361:20011619.

[121] S. E. Woosley and T. A. Weaver. The physics of supernova explosions. Ann. Rev. Astron. Astrophys., 24:205–253, 1986. doi: 10.1146/annurev.aa.24.090186.001225.

[122] J. H. Wise and T. Abel. The Number of Supernovae from Primordial Stars in the Universe. Astrophys. J., 629:615–624, August 2005. doi: 10.1086/430434.

[123] P. Anninos, Y. Zhang, T. Abel, and M. L. Norman. Cosmological hydrodynamics with multi-species chemistry and nonequilibrium ionization and cooling. New Astron., 2:209–224, August 1997. doi: 10.1016/S1384-1076(97)00009-2.

[124] B. Smith, S. Sigurdsson, and T. Abel. Metal cooling in simulations of cosmic structure formation. Mon. Not. R. Astron. Soc., 385:1443–1454, April 2008. doi: 10.1111/j.1365-2966.2008.12922.x.

[125] G. J. Ferland, R. L. Porter, P. A. M. van Hoof, R. J. R. Williams, N. P. Abel, M. L. Lykins, G. Shaw, W. J. Henney, and P. C. Stancil. The 2013 Release of Cloudy. Rev. Mex. de Astrono. y Astrofis., 49:137–163, April 2013.

[126] P. S. Behroozi, R. H. Wechsler, and H.-Y. Wu. The ROCKSTAR Phase-space Temporal Halo Finder and the Velocity Offsets of Cluster Cores. Astrophys. J., 762:109, January 2013. doi: 10.1088/0004-637X/762/2/109.

[127] P. S. Behroozi, R. H. Wechsler, H.-Y. Wu, M. T. Busha, A. A. Klypin, and J. R. Primack. Gravitationally Consistent Halo Catalogs and Merger Trees for Precision Cosmology. Astrophys. J., 763:18, January 2013. doi: 10.1088/0004-637X/763/1/18.

[128] M. J. Turk, B. D. Smith, J. S. Oishi, S. Skory, S. W. Skillman, T. Abel, and M. L. Norman. yt: A Multi-code Analysis Toolkit for Astrophysical Simulation Data. Astrophys. J. Suppl., 192:9, January 2011. doi: 10.1088/0067-0049/192/1/9.

[129] B. T. Draine. Interstellar Dust Grains. Ann. Rev. Astron. Astrophys., 41:241–289, 2003. doi: 10.1146/annurev.astro.41.011802.094840.

[130] M. Asplund, N. Grevesse, A. J. Sauval, and P. Scott. The Chemical Composition of the Sun. Ann. Rev. Astron. Astrophys., 47:481–522, September 2009. doi: 10.1146/annurev.astro.46.060407.145222.

[131] K. Park, T. Di Matteo, S. Ho, R. Croft, S. M. Wilkins, Y. Feng, and N. Khandai. Luminosity function of [O II] emission-line galaxies in the MassiveBlack-II simulation. Mon. Not. R. Astron. Soc., 454:269–279, November 2015. doi: 10.1093/mnras/stv1954.

[132] Chris Wyman, Peter-Pike Sloan, and Peter Shirley. Simple analytic approximations to the CIE XYZ color matching functions. Journal of Computer Graphics Techniques (JCGT), 2(2):1–11, July 2013. ISSN 2331-7418. URL `http://jcgt.org/published/0002/02/01/`.

[133] P. Chen, J. H. Wise, M. L. Norman, H. Xu, and B. W. O'Shea. Scaling Relations for Galaxies Prior to Reionization. Astrophys. J., 795:144, November 2014. doi: 10.1088/0004-637X/795/2/144.

[134] G. Kauffmann, T. M. Heckman, C. Tremonti, J. Brinchmann, S. Charlot, S. D. M. White, S. E. Ridgway, J. Brinkmann, M. Fukugita, P. B. Hall, Ž. Ivezić, G. T. Richards, and D. P. Schneider. The host galaxies of active galactic nuclei. Mon. Not. R. Astron. Soc., 346:1055–1077, December 2003. doi: 10.1111/j.1365-2966.2003.07154.x.

[135] L. J. Kewley, M. A. Dopita, R. S. Sutherland, C. A. Heisler, and J. Trevena. Theoretical Modeling of Starburst Galaxies. Astrophys. J., 556:121–140, July 2001. doi: 10.1086/321545.

[136] J. A. Baldwin, M. M. Phillips, and R. Terlevich. Classification parameters for the emission-line spectra of extragalactic objects. Pub. Astro. Soc. Pacific, 93:5–19, February 1981. doi: 10.1086/130766.

[137] L. J. Kewley, C. Maier, K. Yabe, K. Ohta, M. Akiyama, M. A. Dopita, and T. Yuan. The Cosmic BPT Diagram: Confronting Theory with Observations. Astrophys. J. Lett., 774:L10, September 2013. doi: 10.1088/2041-8205/774/1/L10.

[138] D. Schaerer and S. de Barros. The impact of nebular emission on the ages of z 6 galaxies. Astron. Astrophys., 502:423–426, August 2009. doi: 10.1051/0004-6361/200911781.

[139] C. Hummels, B. Smith, and D. Silvia. Trident: a universal tool for generating synthetic absorption spectra from astrophysical simulations. ArXiv e-prints, December 2016.

[140] E. Zackrisson, A. K. Inoue, and H. Jensen. The Spectral Evolution of the First Galaxies. II. Spectral Signatures of Lyman Continuum Leakage from Galaxies in the Reionization Epoch. Astrophys. J., 777:39, November 2013. doi: 10.1088/0004-637X/777/1/39.

[141] R. Cen and T. Kimm. Infrared Properties of z = 7 Galaxies from Cosmological Simulations. Astrophys. J., 782:32, February 2014. doi: 10.1088/0004-637X/782/1/32.

[142] P. Jonsson. SUNRISE: polychromatic dust radiative transfer in arbitrary geometries. Mon. Not. R. Astron. Soc., 372:2–20, October 2006. doi: 10.1111/j.1365-2966.2006.10884.x.

[143] P. Jonsson, B. A. Groves, and T. J. Cox. High-resolution panchromatic spectral models of galaxies including photoionization and dust. Mon. Not. R. Astron. Soc., 403:17–44, March 2010. doi: 10.1111/j.1365-2966.2009.16087.x.

[144] S. M. Wilkins, Y. Feng, T. Di-Matteo, R. Croft, E. R. Stanway, A. Bunker, D. Waters, and C. Lovell. The photometric properties of galaxies in the early Universe. Mon. Not. R. Astron. Soc., 460:3170–3178, August 2016. doi: 10.1093/mnras/stw1154.

[145] F. Cullen, R. J. McLure, S. Khochfar, J. S. Dunlop, and C. Dalla Vecchia. The First Billion Years project: constraining the dust attenuation law of star-forming galaxies at z 5. Mon. Not. R. Astron. Soc., 470:3006–3026, September 2017. doi: 10.1093/mnras/stx1451.

[146] J. J. Eldridge and E. R. Stanway. BPASS predictions for binary black hole mergers. Mon. Not. R. Astron. Soc., 462:3302–3313, November 2016. doi: 10.1093/mnras/stw1772.

[147] C. F. McKee and E. C. Ostriker. Theory of Star Formation. Ann. Rev. Astron. Astrophys., 45:565–687, September 2007. doi: 10.1146/annurev.astro.45.051806.110602.

[148] T. H. Greif. The numerical frontier of the high-redshift Universe. Computational Astrophysics and Cosmology, 2:3, March 2015. doi: 10.1186/s40668-014-0006-2.

[149] A. Dieball, C. Knigge, D. R. Zurek, M. M. Shara, K. S. Long, P. A. Charles, D. C. Hannikainen, and L. van Zyl. An Ultracompact X-Ray Binary in the Globular Cluster M15 (NGC 7078). Astrophys. J. Lett., 634:L105–L108, November 2005. doi: 10.1086/498712.

[150] R. C. Iping, G. Sonneborn, L. Kaper, and G. Hammerschlag-Hensberge. Far Ultraviolet Observations of the High-Mass X-Ray Binary 4U1700-37/HD153919. In N. St.-Louis and A. F. J. Moffat, editors, Massive Stars in Interactive Binaries, volume 367 of Astronomical Society of the Pacific Conference Series, page 459, 2007.

[151] K. S. S. Barrow, J. H. Wise, M. L. Norman, B. W. O'Shea, and H. Xu. First light: exploring the spectra of high-redshift galaxies in the Renaissance Simulations. Mon. Not. R. Astron. Soc., 469:4863–4878, August 2017. doi: 10.1093/mnras/stx1181.

[152] E. E. Salpeter. The Luminosity Function and Stellar Evolution. Astrophys. J., 121: 161, January 1955. doi: 10.1086/145971.

[153] G. Chabrier. Galactic Stellar and Substellar Initial Mass Function. Pub. Astro. Soc. Pacific, 115:763–795, July 2003. doi: 10.1086/376392.

[154] B. W. O'Shea, C. F. McKee, A. Heger, and T. Abel. First Stars III Conference Summary. In B. W. O'Shea and A. Heger, editors, First Stars III, volume 990 of American Institute of Physics Conference Series, page xiii, March 2008. doi: 10.1063/1.2940787.

[155] P. Kroupa. On the variation of the initial mass function. Mon. Not. R. Astron. Soc., 322:231–246, April 2001. doi: 10.1046/j.1365-8711.2001.04022.x.

[156] A. Heger, C. L. Fryer, S. E. Woosley, N. Langer, and D. H. Hartmann. How Massive Single Stars End Their Life. Astrophys. J., 591:288–300, July 2003. doi: 10.1086/375341.

[157] J. L. Johnson, T. H. Greif, V. Bromm, R. S. Klessen, and J. Ippolito. The first galaxies: signatures of the initial starburst. Mon. Not. R. Astron. Soc., 399:37–47, October 2009. doi: 10.1111/j.1365-2966.2009.15158.x.

[158] E. Zackrisson. Detecting population III galaxies with HST and JWST. In M. Umemura and K. Omukai, editors, American Institute of Physics Conference Series, volume 1480 of American Institute of Physics Conference Series, pages 101–104, September 2012. doi: 10.1063/1.4754337.

[159] M. P. Véron-Cetty and P. Véron. The emission line spectrum of active galactic nuclei and the unifying scheme. Astron. Astro. Rev., 10:81–133, 2000. doi: 10.1007/s001590000006.

[160] D. K. Erb, C. C. Steidel, A. E. Shapley, M. Pettini, N. A. Reddy, and K. L. Adelberger. Hα Observations of a Large Sample of Galaxies at z ˜ 2: Implications for Star Formation in High-Redshift Galaxies. Astrophys. J., 647:128–139, August 2006. doi: 10.1086/505341.

[161] M. Joly. Formation of CA II lines in active galactic nuclei. Astron. Astrophys., 208: 47–51, January 1989.

[162] G. J. Ferland and S. E. Persson. Implications of CA II emission for physical conditions in the broad-line region of active galactic nuclei. Astrophys. J., 347:656–673, December 1989. doi: 10.1086/168156.

[163] M. L. Garcia Vargas, A. I. Diaz, E. Terlevich, and R. Terlevich. The CA II triplet lines in starburst and AGN. Astrop. Space Sci.., 205:85–89, July 1993. doi: 10.1007/BF00657961.

[164] M. Mancini, R. Schneider, L. Graziani, R. Valiante, P. Dayal, U. Maio, B. Ciardi, and L. K. Hunt. The dust mass in z > 6 normal star-forming galaxies. Mon. Not. R. Astron. Soc., 451:L70–L74, July 2015. doi: 10.1093/mnrasl/slv070.

[165] R. Schneider, L. Hunt, and R. Valiante. The dust content of the most metal-poor star-forming galaxies. Mon. Not. R. Astron. Soc., 457:1842–1850, April 2016. doi: 10.1093/mnras/stw114.

[166] H. Xu, K. Ahn, J. H. Wise, M. L. Norman, and B. W. O'Shea. Heating the Intergalactic Medium by X-Rays from Population III Binaries in High-redshift Galaxies. Astrophys. J., 791:110, August 2014. doi: 10.1088/0004-637X/791/2/110.

[167] D. J. Whalen, C. L. Fryer, D. E. Holz, A. Heger, S. E. Woosley, M. Stiavelli, W. Even, and L. H. Frey. Seeing the First Supernovae at the Edge of the Universe with JWST. Astrophys. J. Lett., 762:L6, January 2013. doi: 10.1088/2041-8205/762/1/L6.

[168] X. Fan, M. A. Strauss, R. H. Becker, R. L. White, J. E. Gunn, G. R. Knapp, G. T. Richards, D. P. Schneider, J. Brinkmann, and M. Fukugita. Constraining the Evolution of the Ionizing Background and the Epoch of Reionization with z˜6 Quasars. II. A Sample of 19 Quasars. Astronomical. J., 132:117–136, July 2006. doi: 10.1086/504836.

[169] D. J. Mortlock, S. J. Warren, B. P. Venemans, M. Patel, P. C. Hewett, R. G. McMahon, C. Simpson, T. Theuns, E. A. Gonzáles-Solares, A. Adamson, S. Dye, N. C. Hambly, P. Hirst, M. J. Irwin, E. Kuiper, A. Lawrence, and H. J. A. Röttgering. A luminous quasar at a redshift of z = 7.085. Nat., 474:616–619, June 2011. doi: 10.1038/nature10159.

[170] F. Wang, X.-B. Wu, X. Fan, J. Yang, W. Yi, F. Bian, I. D. McGreer, Q. Yang, Y. Ai, X. Dong, W. Zuo, L. Jiang, R. Green, S. Wang, Z. Cai, R. Wang, and M. Yue. A Survey of Luminous High-redshift Quasars with SDSS and WISE. I. Target Selection and Optical Spectroscopy. Astrophys. J., 819:24, March 2016. doi: 10.3847/0004-637X/819/1/24.

[171] R. Edgar. A review of Bondi-Hoyle-Lyttleton accretion. New Astro. Rev., 48:843–859, September 2004. doi: 10.1016/j.newar.2004.06.001.

[172] F. Yuan and R. Narayan. Hot Accretion Flows Around Black Holes. Ann. Rev. Astron. Astrophys., 52:529–588, August 2014. doi: 10.1146/annurev-astro-082812-141003.

[173] A. Loeb and F. A. Rasio. Collapse of primordial gas clouds and the formation of quasar black holes. Astrophys. J., 432:52–61, September 1994. doi: 10.1086/174548.

[174] V. Bromm and A. Loeb. Formation of the First Supermassive Black Holes. Astrophys. J., 596:34–46, October 2003. doi: 10.1086/377529.

[175] A. Aykutalp, J. H. Wise, M. Spaans, and R. Meijerink. Songlines from Direct Collapse Seed Black Holes: Effects of X-Rays on Black Hole Growth and Stellar Populations. Astrophys. J., 797:139, December 2014. doi: 10.1088/0004-637X/797/2/139.

[176] J. H. Wise and T. Abel. Suppression of H_2 Cooling in the Ultraviolet Background. Astrophys. J., 671:1559–1567, December 2007. doi: 10.1086/522876.

[177] T. P. Stecher and D. A. Williams. Photodestruction of Hydrogen Molecules in H I Regions. Astrophys. J. Lett., 149:L29, July 1967. doi: 10.1086/180047.

[178] A. Aykutalp, J. H. Wise, R. Meijerink, and M. Spaans. The Response of Metal-rich Gas to X-Ray Irradiation from a Massive Black Hole at High Redshift: Proof of Concept. Astrophys. J., 771:50, July 2013. doi: 10.1088/0004-637X/771/1/50.

[179] D. R. G. Schleicher, M. Spaans, and R. S. Klessen. Probing high-redshift quasars with ALMA. I. Expected observables and potential number of sources. Astron. Astrophys., 513:A7, April 2010. doi: 10.1051/0004-6361/200913467.

[180] R. Meijerink and M. Spaans. Diagnostics of irradiated gas in galaxy nuclei. I. A far-ultraviolet and X-ray dominated region code. Astron. Astrophys., 436:397–409, June 2005. doi: 10.1051/0004-6361:20042398.

[181] G. Mellema, I. T. Iliev, M. A. Alvarez, and P. R. Shapiro. C ^{2}-ray: A new method for photon-conserving transport of ionizing radiation. New Astron., 11:374–395, March 2006. doi: 10.1016/j.newast.2005.09.004.

[182] T. Abel, P. Anninos, Y. Zhang, and M. L. Norman. Modeling primordial gas in numerical cosmology. New Astron., 2:181–207, August 1997. doi: 10.1016/S1384-1076(97)00010-9.

[183] B. D. Lehmer, A. R. Basu-Zych, S. Mineo, W. N. Brandt, R. T. Eufrasio, T. Fragos, A. E. Hornschemeier, B. Luo, Y. Q. Xue, F. E. Bauer, M. Gilfanov, P. Ranalli, D. P. Schneider, O. Shemmer, P. Tozzi, J. R. Trump, C. Vignali, J.-X. Wang, M. Yukita, and A. Zezas. The Evolution of Normal Galaxy X-Ray Emission through Cosmic History: Constraints from the 6 MS Chandra Deep Field-South. Astrophys. J., 825:7, July 2016. doi: 10.3847/0004-637X/825/1/7.

[184] P. Madau and T. Fragos. Radiation Backgrounds at Cosmic Dawn: X-Rays from Compact Binaries. Astrophys. J., 840:39, May 2017. doi: 10.3847/1538-4357/aa6af9.

[185] M. D. Perrin, R. Soummer, E. M. Elliott, M. D. Lallo, and A. Sivaramakrishnan. Simulating point spread functions for the James Webb Space Telescope with WebbPSF. In Space Telescopes and Instrumentation 2012: Optical, Infrared, and Millimeter Wave, volume 8442 of Proc. of SPIE, page 84423D, September 2012. doi: 10.1117/12.925230.

[186] S. Chon, S. Hirano, T. Hosokawa, and N. Yoshida. Cosmological Simulations of Early Black Hole Formation: Halo Mergers, Tidal Disruption, and the Conditions for Direct Collapse. Astrophys. J., 832:134, December 2016. doi: 10.3847/0004-637X/832/2/134.

[187] J. A. Regan, E. Visbal, J. H. Wise, Z. Haiman, P. H. Johansson, and G. L. Bryan. Rapid formation of massive black holes in close proximity to embryonic protogalaxies. Nature Astronomy, 1:0075, March 2017. doi: 10.1038/s41550-017-0075.

[188] F. Pacucci, A. Ferrara, A. Grazian, F. Fiore, E. Giallongo, and S. Puccetti. First identification of direct collapse black hole candidates in the early Universe in CANDELS/GOODS-S. Mon. Not. R. Astron. Soc., 459:1432–1439, June 2016. doi: 10.1093/mnras/stw725.

[189] P. Natarajan, F. Pacucci, A. Ferrara, B. Agarwal, A. Ricarte, E. Zackrisson, and N. Cappelluti. Unveiling the First Black Holes With JWST:Multi-wavelength Spectral Predictions. Astrophys. J., 838:117, April 2017. doi: 10.3847/1538-4357/aa6330.

[190] R. A. Simcoe. High-Redshift Intergalactic C IV Abundance Measurements from the Near-Infrared Spectra of Two z ˜ 6 QSOs. Astrophys. J., 653:977–987, December 2006. doi: 10.1086/508983.

[191] J. Schaye, A. Aguirre, T.-S. Kim, T. Theuns, M. Rauch, and W. L. W. Sargent. Metallicity of the Intergalactic Medium Using Pixel Statistics. II. The Distribution of Metals as Traced by C IV. Astrophys. J., 596:768–796, October 2003. doi: 10.1086/378044.

[192] F. Matteucci and F. Calura. Early chemical enrichment of the universe and the role of very massive population III stars. Mon. Not. R. Astron. Soc., 360:447–452, June 2005. doi: 10.1111/j.1365-2966.2005.08908.x.

[193] J. Schaye, R. A. Crain, R. G. Bower, M. Furlong, M. Schaller, T. Theuns, C. Dalla Vecchia, C. S. Frenk, I. G. McCarthy, J. C. Helly, A. Jenkins, Y. M. Rosas-Guevara, S. D. M. White, M. Baes, C. M. Booth, P. Camps, J. F. Navarro, Y. Qu, A. Rahmati, T. Sawala, P. A. Thomas, and J. Trayford. The EAGLE project: simulating the evolution and assembly of galaxies and their environments. Mon. Not. R. Astron. Soc., 446:521–554, January 2015. doi: 10.1093/mnras/stu2058.

[194] Albert Einstein. Die grundlage der allgemeinen relativitätstheorie. Annalen der Physik, 354:769–822, 1916.

[195] A. Friedmann. Über die Möglichkeit einer Welt mit konstanter negativer Krümmung des Raumes. Zeitschrift fur Physik, 21:326–332, December 1924. doi: 10.1007/BF01328280.